# EXPERIMENTAL INVESTIGATION OF 3D FLOW FIELD AROUND A FLAPPING WING MAKING FIGURE OF EIGHT MOTION IN HOVER USING PIV TECHNIQUE

A THESIS SUBMITTED TO

THE GRADUATE SCHOOL OF NATURAL AND APPLIED SCIENCES

OF

MIDDLE EAST TECHNICAL UNIVERSITY

BY

İREM ERSÖZ

IN PARTIAL FULFILLMENT OF THE REQUIREMENTS

FOR

THE DEGREE OF MASTER OF SCIENCE

IN

AEROSPACE ENGINEERING

SEPTEMBER 2014

Approval of the thesis:

**EXPERIMENTAL INVESTIGATION OF 3D FLOW FIELD AROUND A FLAPPING WING MAKING FIGURE OF EIGHT MOTION IN HOVER USING PIV TECHNIQUE**

Submitted by **İREM ERSÖZ** in partial fulfillment of the requirements for the degree of **Master of Science in Aerospace Engineering Department, Middle East Technical University** by,

Prof. Dr. Canan Özgen
Dean, Graduate School of Natural and Applied Sciences           _____


Prof. Dr. Ozan Tekinalp
Head of Department, **Aerospace Engineering**                          _____


Prof. Dr. Nafiz Alemdaroğlu
Supervisor, **Aerospace Engineering Dept., METU**               _____


**Examining Committee Members:**
Prof. Dr. Serkan Özgen                                          _____
Aerospace Engineering Dept., METU


Prof. Dr. Nafiz Alemdaroğlu                                     _____
Aerospace Engineering Dept., METU


Prof. Dr. Altan Kayran                                          _____
Aerospace Engineering Dept., METU


Doç. Dr. Sinan Eyi                                             _____
Aerospace Engineering Dept., METU


Dr. Ebru (Sarıgöl) Ortakaya                                     _____
Rocket Industrial And Trading Inc. (ROKETSAN)        **Date**:\_ 03 / 09 / 2014\_

I hereby declare that all information in this document has been obtained and presented in accordance with academic rules and ethical conduct. I also declare that, as required by these rules and conduct, I have fully cited and referenced all material and results that are not original to this work.

Name, Last name: İREM ERSÖZ

Signature　　　　:

**ABSTRACT**

**EXPERIMENTAL INVESTIGATION OF 3D FLOW FIELD AROUND A FLAPPING WING MAKING FIGURE-OF-EIGHT MOTION IN HOVER USING PIV TECHNIQUE**

ERSÖZ, İrem

M.S., Department of Aerospace Engineering
Supervisor: Prof. Dr. Nafiz Alemdaroğlu

September 2014, 101 pages

This thesis presents the results of experimental investigation of vortex formation around a three dimensional flapping wing making figure-of-eight motion in hovering flight at low Reynolds numbers. These results are compared with those obtained from previous computational and experimental studies of the same flapping motions. Analysis of vortex formations around the three dimensional flapping wing and the investigations of the effect of different parameters such as the amplitude of motion in y direction and the angle of attack throughout the spanwise direction are performed using the Particle Image Velocimetry (PIV) technique. The experimental setup that was previously used in the study of Baskan was improved, in such way that the vortical structures during the figure-of-eight motion could be visualized and measured much better. From series of measurements, the three-dimensional experimental results indicate a very good agreement with the two-dimensional numerical results which were performed by Cekinmez.

Keywords: Flapping Motion, Figure-of-Eight Motion, Leading Edge Vorticity, Trailing Edge Vorticity, PIV.

# ÖZ

## PIV TEKNİĞİ KULLANARAK HAVADA ASILI KONUMDA SEKİZ ŞEKLİ ÇİZEREK ÇIRPAN BİR KANAT ETRAFINDAKİ 3 BOYUTLU AKIŞ ALANININ DENEYSEL İNCELENMESİ

ERSÖZ, İrem

Yüksek Lisans, Havacılık ve Uzay Mühendisliği Bölümü

Tez Yöneticisi: Prof. Dr. Nafiz Alemdaroğlu

Eylül 2014, 101 sayfa

Bu çalışma, düşük Reynolds sayısındaki havada asılı durumda sekiz hareketi çizen üç boyutlu bir çırpan kanat etrafındaki girdap oluşumlarını araştıran ve bu sonuçları önceki çalışmalarda analiz edilmiş olan çırpma hareketleri ile karşılaştıran deneysel bir çalışmadır. Üç boyutlu çırpan kanat etrafındaki vorteks oluşumlarına, kanat uzunluğu boyunca hücum açısı, y yönündeki hareket genliği gibi farklı parametrelerin etkisini araştırılmış ve ölçümler Parçacık Görüntülemeli Hız Ölçme (PIV) tekniği ile gerçekleştirilmiştir. Başkan'ın çalışmasında kullanılan deneysel düzenek biraz daha geliştirilerek, sekiz hareketi yapan üç boyutlu kanat etrafındaki girdap yapıları daha net olarak görüntülenmiş ve ölçülebilmiştir. Bu ölçümlerin sonucunda elde edilen üç boyutlu deneysel sonuçlar, Çekinmez tarafından elde edilen iki boyutlu ölçümler ve numerik sonuçlar ile karşılaştırılmış ve iki boyutlu ölçmelerin birbirlerine benzer olduğunu gösterilmiştir.

Anahtar Kelimeler: Çırpma Hareketi, Sekiz Şekli Hareketi, Hücum kenarı girdapları, Firar kenarı girdapları, PIV.

To My Family…

# ACKNOWLEDGEMENTS

# TABLE OF CONTENTS

# LIST OF TABLES

# LIST OF FIGURES

xiv

# NOMENCLATURE

DARPA        :Defense Advanced Research Project Agency

MAV          :Micro Air Vehicle

DNS          :Direct Numerical Simulation

CFD          :Computational Fluid Dynamics

PIV          :Particle Image Velocimetry

SPIV         :Stereoscopic Particle Image Velocimetry

LEV          :Leading Edge Vortex

TEV          : Trailing Edge Vortex

CW           : Clock-Wise

CCW          : Counter-Clock-Wise

3-D          : Three-dimensional

2-D          : Two-dimensional

Re           : Reynolds number

AoA          :Angle of attack

$\alpha$          :Initial of angle of attack

B            :A distance of vertical amplitude during  figure-of-eight motion

c            :Chord length of the NACA 6412 airfoil

# CHAPTER 1

# INTRODUCTION

Up to now, numerous attempts in hovering flight have been performed using numerical and/or experimental methods to understand the vortex formation around flapping wings in linear flapping motion. Especially, in the last five years hummingbirds as a special species of hoverers are widely investigated to catch its aerodynamic mechanism during hovering flight.

This chapter introduces general information about the importance of the flapping flight with the brief information about hovering flight. After the definition of motion studied in this thesis is explained, this chapter concludes with the objective and the outline of the present study.

## 1.1. Background:

Over last decades, biological systems of insects or birds have shed light to inspiring engineers for their use of unsteady aerodynamics with flapping wings, since there are many requirements like surveillance, maneuverability and etc. of small vehicles at low speeds. And, challenges in less energy consumption of the vehicles have opened a new opportunities in civilian and military applications. Especially in military applications, the primary advantage is the ability of reconnaissance vehicles and the other one is their ease of transport to the battlefield, even in a soldier's backpack. Given safety and accessibility considerations, the Micro Air Vehicles (MAVs) become inevitable tools to use in such contaminated and toxic areas, where entrance of humans is strictly banned. As a result of derivation from both physical and technological considerations for the limit size of MAVs, the vehicles consist of the dimensions less than 15 cm in size, which is comparable to the size of small birds or bats, and a flight speed of 10–20 m/s (a definition employed by Defense Advanced

Research Project Agency, DARPA) Ref. [1]. Because of this small size and low velocities, MAVs operate a very sensitive Reynolds number (Re) regime $10^3$-$10^5$, where the flow separation around an airfoil can result in sudden increases in drag and loss of efficiency. In order to see flight regime of MAVs, the comparison of the flight regime of Micro Air Vehicles to existing flight regime is given as below.
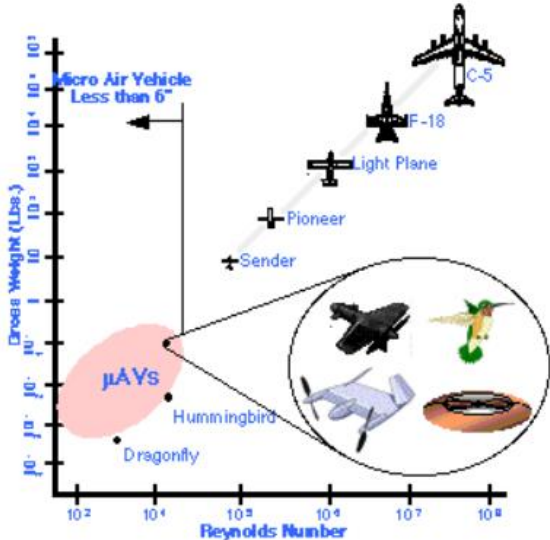


Figure 1. Comparison of flight regimes from Ref. [2]

Even though the flight regime cause loss of efficiency, MAVs have some advantages, these are:

- more reasonable to achieve faster, better and cheaper
- practically undetectable,
- exploring new fields, etc.

MAVs have performed wide range of tasks in many applications since the late 1990s. MAVs equipped with a video camera or a sensor which enables these vehicles

to perform surveillance and reconnaissance, targeting, and biochemical sensing at remote or otherwise hazardous locations. For this, various numbers of proposed designs have been built and tested, including flying wings, conventional platforms, rotary wing platforms and flapping wing platforms. Among all MAV concepts, the flapping wing MAVs (see in Figure 2) exhibits a better aerodynamic performance in the low Reynolds number regime than fixed-wing and rotary-wing in hovering mode, since the relatively large forces that are generated during flapping flight cannot be explained with conventional fixed-wing aerodynamic theory. This means by advance of flapping wings not only very high unsteady lift is achieved but also the combination of lift and thrust mechanisms and the ability of their hovering flight can be obtained.
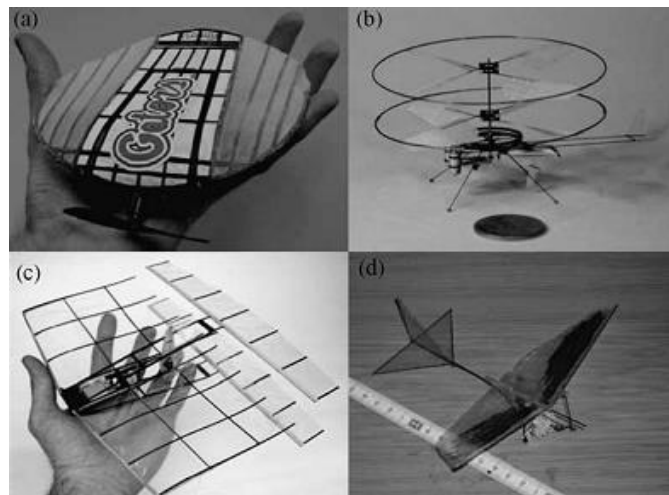


Figure 2. Representative MAVs: (a) flexible fixed wing; (b) rotary wing; (c) hybrid flapping–fixed wing, with the fixed wing used for lift and the flapping wing for thrust; and (d) flapping wing for both lift and thrust (Adapted from Ref [3])

When looking at the bird species hanging in the air, different types of the motion stand out in terms of high maneuverability and hovering capabilities. As the kinematics of flapping wing motions for many different families of birds and insects are analyzed, this serves us to correlate a relation between in nature and new MAVs design. Of all MAVs designs in flapping flight, it is important to note that designed MAVs can be powered by either with muscles or with engines.

As a special kind of ornihopters (see in Figure 3), entomopter which was developed by the Georgia Tech Research Institute (GTRI), University of Cambridge (England), and ETS Labs Ref [4] using Reciprocating Chemical Muscle (RCM) is able to fly on the planet Mars achieving high lift during forward flight.



Figure 3. The left side of figure is the entomopter From Ref [4], the right side of figure is a kind of ornihopters From Ref [5]

Inspired from dragonflies, lack of hovering flight of ornihopters could be resolved by a new design of the TechJect's Dragonfly which was created by a multi-disciplinary team from the Georgia Institute of Technology in 2013. Seen in Figure 4, the robot dragonfly has four wings as a combination of forewings and hindwings with a weight of nearly 25 g and a length of 15 cm (Ref. [6]). In terms of the actuator system, the wings are divided into 4 categories as alpha, delta, gamma and omega models. The former is based on magnetic solenoidal actuators, while the others

depends on a Continuously Variable Transmission (CVT). By aid of a single-cell Li-Po battery rated at 250mAh, a flight capability of robot dragonfly can be between 8 and 10 minutes in hovering flight, which is extended by a hybrid flight (a combination of hovering and gliding motion) of nearly 25–30 minutes with maximum speeds of 35 mph Ref [6].



| DRAGONFLY MODELS → | ALPHA | DELTA | GAMMA | OMEGA |
|---|---|---|---|---|
| Flight Computer | MARC-Basic | MARC-Basic | MARC-2 | MARC-3 |
| Re-configurable Processor. | | | ✔ | ✔ |
| Hovering | | ✔ | ✔ | ✔ |
| Gliding | ✔ | ✔ | ✔ | ✔ |
| Accelerometers | ✔ | ✔ | ✔ | ✔ |
| Gyroscopes | ✔ | ✔ | ✔ | ✔ |
| Remote Control | ✔ | ✔ | ✔ | ✔ |
| GPS | | | | ✔ |
| Advanced Sensor Pack – 18 Environmental Sensors | | | | ✔ |
| Camera(s) | Add-on* | Add-on* | ✔ | ✔ ✔ |
| Wi-Fi | Add-on* | Add-on* | ✔ | ✔ |
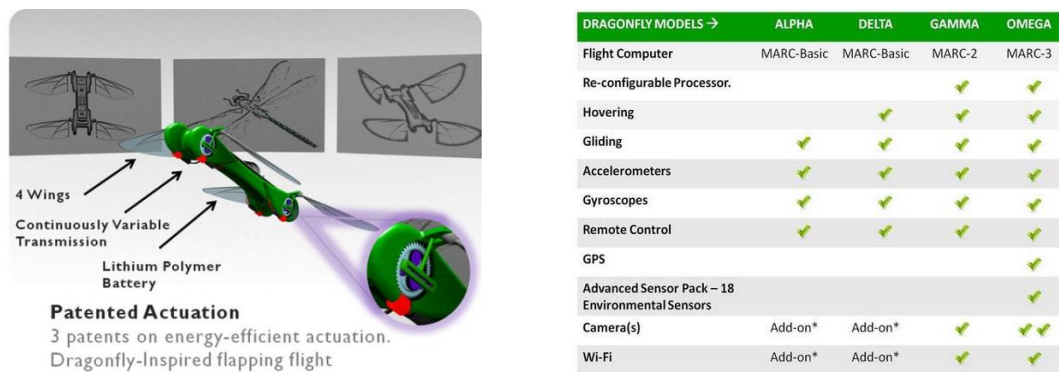
Figure 4. The representation of robot dragonfly was created by Georgia Institute of Technology with its features. (Ref. [6])

### 1.1.1. Flapping Flight and Hovering Flight:

Differences between flapping flight, also known as powered flight, and hovering flight should be distinguished. The most significant difference is a generation of thrust in flapping flight. The flapping motion in the literature is done with a nonzero free stream velocity. Conversely, the purpose of hovering flight is production of a vertical force to balance the weight. So, it is assumed to be the body fixed in space and the free stream velocity is zero. This means the fluid motions only come from the wing motions.

As the flapping patterns of birds, bats, and insects are investigated, relative to species a wide variety of different flapping patterns emerge in hovering and forward

flight. Generally, larger birds have simple wingtip paths like an oval tip path, whereas smaller flyers relatively exhibit more complicated flapping patterns. Figure 5 illustrates several different flight patterns (Ref [3]).
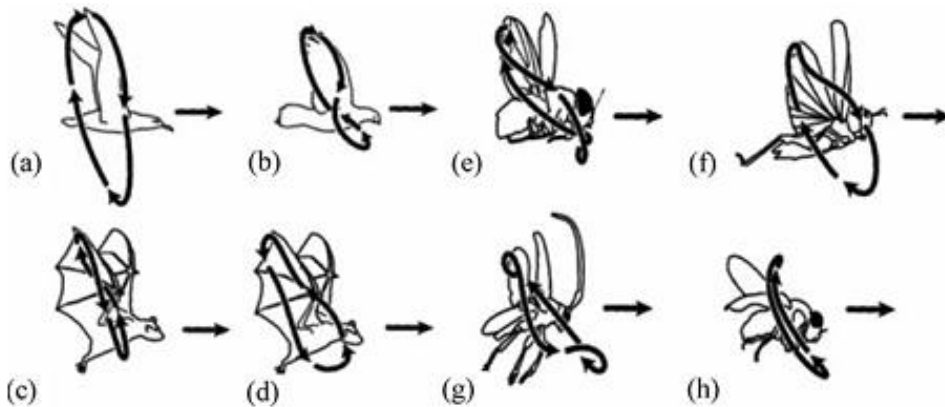


Figure 5. Wingtip paths relative to the body for a variety of flyers, as indicated by the arrows: (a) albatross, fast gait; (b) pigeon, slow gait; (c) horseshoe bat, fast flight; (d)horseshoe bat, slow gait; (e) blowfly; (f) locust; (g) June beetle; (h) fruit fly. (Adapted from Ref. [3])

In the detailed literature survey been accomplished two kinds of hovering motion have been appeared as symmetric hovering (called as insect stroke) and asymmetric hovering (called as avian stroke), which are described by Norberg (Ref. [7]).

**1.1.1.1. Asymmetric Hovering Flight:**

Asymmetric hovering flight, also called "avian stroke", is performed by large birds which cannot rotate their wings between forward and backward stroke whose wings are extended to provide more lift during downstroke. For this, the stroke plane is more tilted (see in Figure 6). Thus, during the upstroke the wings are flexed backward to reduce drag.
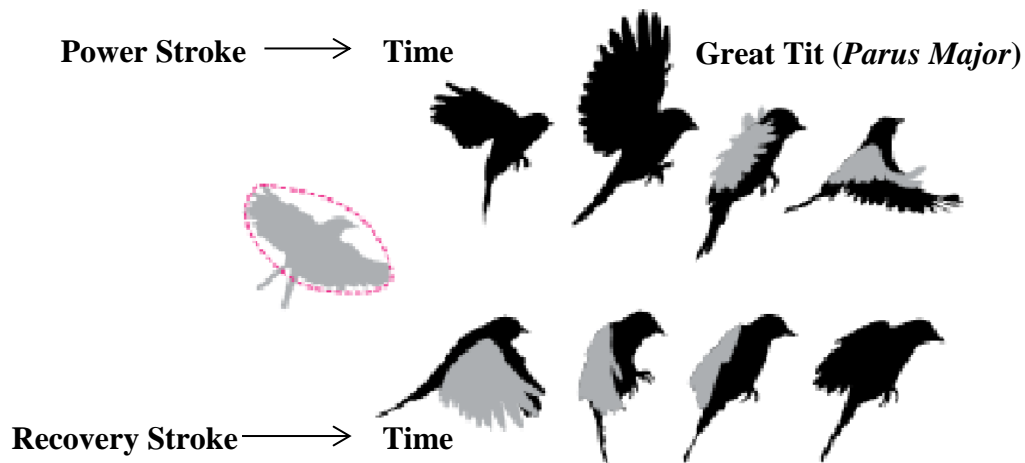
Figure 6. Illustration of Asymmetric Hovering Flight or "Avian Stroke" (Ref. [8])

### 1.1.1.2 Symmetric Hovering Flight:

Symmetric hovering, also called normal or true hovering, or "insect stroke" (Ref. [3]), is performed by hummingbirds or insects that hover with fully extended wings during the entire wing-beat cycle as seen in Figure 7a. Except at the reversal points, positive lift is produced during the entire wing stroke, since the wings flip at positive angle of attack around the edges of the eight. The wings are rotated and twisted during the backstroke so that the leading edge of the wing remains the same throughout the cycle. But the upper surface of the wing during the forward stroke becomes the lower surface during the backward stroke. The wing movements during downstroke and upstroke can be seen in Figure 7b. Regardless of the wings' exact shapes, the plugging-down motion indicates that insects may use aerodynamic drag in addition to lift to support its weight. Note that, during hovering flight, the body axis is inclined at a desirable angle and the wings describe a figure-of-eight in the vertical plane (Ref. [3]). The figure-of-eight motion was firstly described by the French scientist Marey in 1869 (Ref [9]). In that motions, the wing-tip trajectories of many insects resembles the figure "eight", and this motion is particularly used for hovering flight as a superposition of heaving and pitching motion.

7

Figure 7a. Illustration of Symmetric Hovering Flight or "Insect Stroke" (Ref. [8])
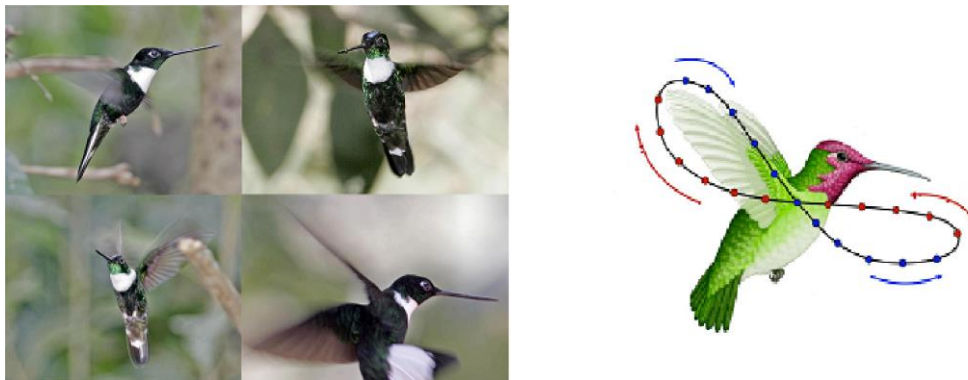


Figure 7b. Illustrations of hummingbird in hovering flight making figure-of-eight motion. The wing path is seen right side. The red arrows are upstroke, the blue arrows are downstroke of hovering motion. (Ref. [8])

## 1.1.2. Hovering Flight Kinematics:
### 1.1.2.1. Linear Motion:

As stated in symmetric hovering flight, insect flight is the similar the flight mechanism to normal hovering flight. Fundamentally, insects use a reciprocating movement of the wings as seen schematic approach of one flap cycle in Figure 8.

In literature, this movement is divided by two half-stroke as downstroke and upstroke. At the end of these strokes translational movements predominantly occur

and pitch angle then rather changes. Because of this, three phases can be distinguished in insects' flight: the translational phase (moving the wing fore and aft), the rotational phase (when the pitch angle of the wing is changing substantially) and the heaving and plunging phase (upwards and downwards movement of the leading edges). During rotational phases or at the end of each half-stroke, the wing stroke inverses and the wing pitch rapidly changes. At the end of upstroke the pronation motion occurs, at the end of downstroke the supination motion occurs as seen in Figure 8.
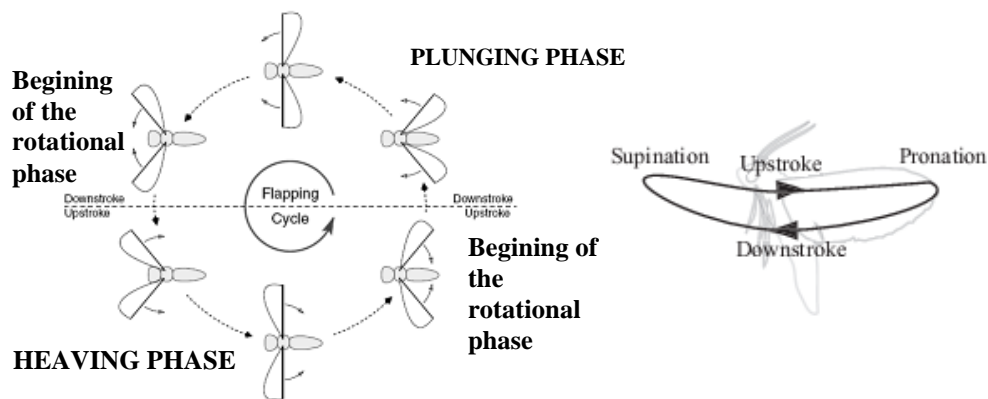


Figure 8. Schematic representation of half strokes during insect hovering flight.
(Adapted from Ref [10])

From previous study of Kurtulus (Ref. [11]), the linear flapping motion was analyzed in four main phases. The motion contains two translational phases as upstroke and downstroke in that the translational phases end at the high angles of attack and two rotational phases as pronation and supination appears at the end of stroke reversal. As seen in Figure 9, the first region corresponds to the half of the downstroke in that the leading edge is pointing in positive direction by following the half-upstroke. The last two regions are the mirror regions of the first two ones

respectively. That is, the first region as a half of downstroke corresponds to the third region as a half of the upstroke.
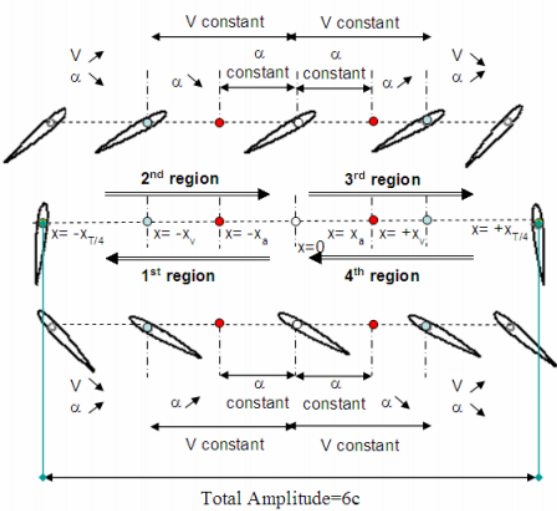


Figure 9. The schematic illustration of flapping motion defined by Kurtulus (Ref. [11])

From the definition of Kurtulus, the flapping motion starts with a first half of downstroke as a translational phase, the wing profile translates with a constant velocity until the time $t_v$ and position $x_v$ at that point where the velocity begins to decrease. At the end of downstroke, the airfoil rotates around a point on the chord line (1/4c, 1/2c, 3/4c for 3 different cases studied by Kurtulus Ref. [11]) from leading edge. The rotational motion is superimposed on the translational motion at a predefined time $t_a$ and position $x_a$.

T is the period of the flapping motion. The motion of airfoil start from rest with a constant velocity from the origin (x=0) until the position of $x_v$ at time $t_v$. After passing the position of $x_v$, the airfoil begins to decelerate until zero velocity at the quarter period of motion. Then, the airfoil rotates around the center of rotation around a point on the chord line, where it reaches an angle of attack of 90° at t=T/4.

10

From the definition of Kurtulus (Ref. [11]), the velocity (V) and the angular velocity variation ($\omega$) are represented in Equation 1.1. and Equation 1.2.

$$V = V_0 \cos(\frac{\pi}{2}\frac{(t - t_v)}{(\frac{T}{4} - t_v)})$$ (Eqn. 1.1.)

$$\omega = -\frac{\omega_{max}}{2}(1 - \cos(\frac{\pi}{2}\frac{(t-t_a)}{(\frac{T}{4}-t_a)}))$$ (Eqn. 1.2.)

$$\omega_{max} = \frac{2 \propto_0}{\frac{T}{4}-t_a}$$ (Eqn. 1.3.)

Where

$$T = \frac{4\pi}{2|V_0|}(x_{\frac{T}{4}} - x_{v)} + t_v$$ (Eqn. 1.4.)

Insects' flight is accomplished by either of two mechanisms, the Weis-Fogh mechanism (the clap-and-fling mechanism) or the delayed-stall/rotational-lift-wake-capture mechanism (the same term as dynamic stall or LEVs.).

To give general information about the species using Weis-Fogh's flight mechanism and delayed stall mechanism, Table 1 is given as follows:

Table 1. Insect flight mechanisms (Ref. [12])

| Weis-Fogh: | Delayed-Stall: |
|---|---|
| Hover flies, Syrphinae | Birds, Hummingbirds |
| Dragonflies, Odonta | Bats |
| Butterflies, Lepidoptera Rhopalocera | Most flying beetles |
| Wasp, Encarsia Formasa | Sphinx moths |

### 1.1.2.2. Definition of motion studied in the thesis:

In this study, the hovering flight making the figure-of-eight motion is analyzed at $x_v = x_c = 2c$ and $t_v = t_c$ by rotating the airfoil at quarter chord line (1/4 c) from the leading edge.

11

The wing motion in symmetric hovering flight or normal hovering resembles a figure-of-eight as seen in Figure 10, examining in 4 regions. The first region corresponds to the half of the downstroke in that the leading edge is pointing in positive direction by following the half-upstroke. During the first region-also named as a translational phase, since the wing profile translates with a constant velocity until the time $t_v$ and position $x_v$, Sarigol (Ref. [13]) explained that the vortices near TEVs are translated to the flow. The third and fourth regions are the mirror regions of the first and second regions respectively. Figure 11 shows the description of the hovering motion for one period.
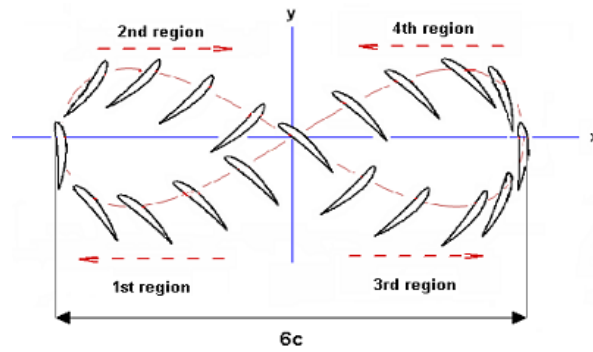


Figure 10. Schematic illustration of the wing path at each region on Lissajous curve (Ref [14])

In order to analyze this type of motion, as a continuous trajectory from the wing tip, the Lissajous curves are used, which is the graph of a system of parametric equations describing a complex harmonic motion. The parametric equations are given as below:

$$x = A\sin(at + \delta) \qquad \text{(Eqn. 1.5.)}$$

$$y = B\sin(bt) \qquad \text{(Eqn. 1.6.)}$$

12

Where, t $t \in [0, 2\pi]$, phase difference $\delta$ $(\delta = \frac{\pi}{2})$ , as angular frequencies a, (a=1), and b, (b=2) , yielding $|a - b| = 1$. As given in Figure 11, a total displacement of the airfoil is 6 chord lengths (6c) in horizontal direction during the figure-of-eight motion. So, value of A in Eqn 1.5 is 3c as a half of this displacement for all cases studied. Also, two different values of B (amplitude in y direction) are studied throughout the present study as B=c and B=2c. B=c and B=2c values correspond to a half of total displacement in vertical direction. The presentation of these values is indicated in Figure 11.
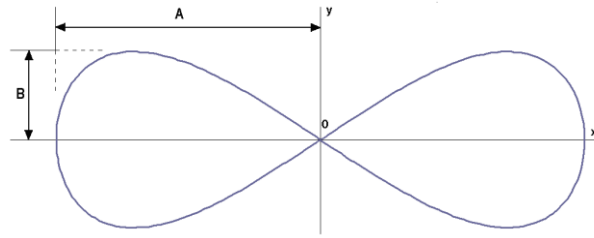


Figure 11. Lissajous curve used for figure-of-eight motion (Ref.[14])

The non-dimensional time (t*) is obtained by dividing the time of captured image to total period; i.e. t/T=1 corresponds that one cycle ends at the starting point of the previous motion.

$$t^* = \frac{t}{T_{periyot}}$$
(Eqn. 1.7.)

As seen in Figure 12, the motion starts plunging from Point 1 to Point 2 (t=0,163 T) with the first half downstroke as a translational phase, the airfoil translates with a constant velocity until the time $t_v$ and position $x_v = \frac{1}{4}$ c at that Point 2 where the velocity begins to decrease. At Point 2, the wing model rotates around its chord line from leading edge. Between Point 2 and 3 (t= 0.211T), the wing is in the middle of

13

the rotation and reaches an angle of attack of 0° at Point 3 (t=0.25T). After Point 3, the wing continues its motion as seen in the image in Figure 12 at t=0.298T. Until the wing reaches it starting angle of attack at t=0.349T, it continues its motion. Then, the wing completes one cycle after passing the mirror regions of first and second regions.
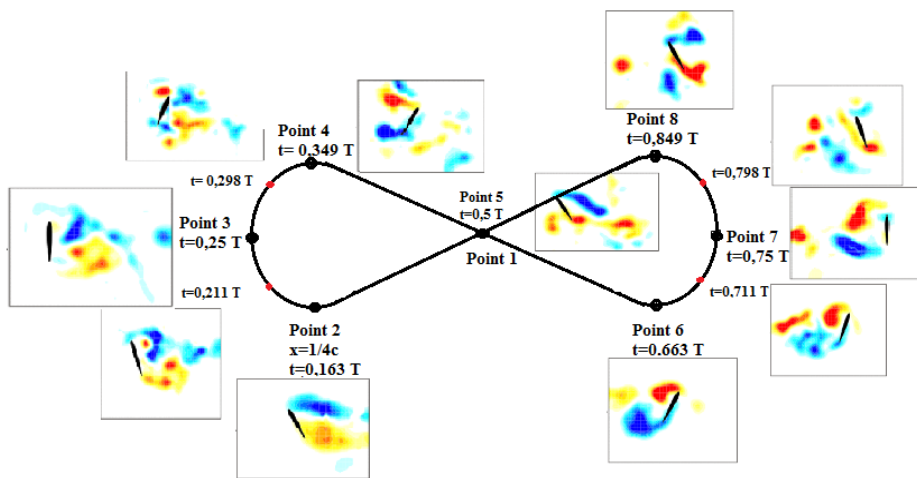


Figure 12. The images captured in different 8 points along one cycle for the wing having NACA 0012 airfoil at α= 60 ° are taken from the study of Baskan (Ref. [14]).

## 1.2. Objective and Outline of the Present Study:

The purpose of this study is to investigate a vortex formation around a 3-D flapping wing making a figure-of-eight motion in hovering flight at a low Reynolds number, 1000, experimentally. To analyze vortex formations around the 3-D flapping wing using PIV technique, FlowManager software was used to visualize seeding particles inside a water tank having 1 x 1 x 1,5 m$^3$ dimensions. By improving the experimental setup which was used in the study of Baskan (Ref. [14]), measurements of wing having NACA 6412 airfoil are taken in each direction of hovering motion.

14

The experimental results will be compared with the experimental and numerical study of Cekinmez (Ref. [15]) consisting 2-D flapping wing (NACA 6412) making figure-of-eight motion. This study is conducted at Reynolds number of 1000, unsteady, incompressible and inviscid flow and the effect of figure-of-eight motion conducting the studies on NACA 6412, which were used previous studies, will be quantified.

This thesis contains five chapters. The first section in Chapter 1 introduces the importance of the flapping flight with different wing motion where its subsection explains the differences between flapping flight and hovering flight, which was widely confused especially for hovering flights due to numerous flight patterns. Following the explanation of insects or bird flight mechanisms with the definition of motion studied in this thesis, a detailed literature survey related to hovering flights at low Reynolds number regime MAVs or insects/birds is given in the Chapter 2. Then, the experimental procedure, measurement details and experimental setup are extensively explained in Chapter 3. Chapter 4 presents the results obtained from measurements and compares the obtained results with the previous studies. Lastly, Chapter 5 serves the conclusion, general remarks with future recommendations on the study.

# CHAPTER 2

# LITERATURE SURVEY

In civilian and military applications requirements of surveillance, maneuverability and other one for small vehicles at low speeds cause aerodynamicists to investigate aerodynamic mechanisms of flapping wings by inspiring from biological systems of insects or birds. Up to now, a several number of studies have been carried out by biologists and aerodynamicists to understand the flapping motion phenomena using a model of real insect/bird wing geometries or different airfoil profiles which are often called as simplified model.

It should be taken into consideration that the investigation of flapping motion should be carried out as a combination of analytical, numerical and experimental studies of flapping motion to understand the flight mechanisms of MAVs. Therefore, in order to understand evidently the aerodynamic behavior and the flight mechanisms of flapping motion of birds or insects, detailed information of experimental studies for the investigations flapping motion is given in this chapter.

At the beginning of 1930s, an analytical approach for estimating the unsteady lift and moment on harmonically oscillating airfoils was published by Theodorsen (Ref. [16]) on the assumption of an inviscid and incompressible flow. Theodorsen also assumed that all oscillations were of very small amplitude so that the flow would be fully attached to the airfoil during flapping cycle. So, the Kutta condition was applied at the trailing edge of the airfoil, and the wake of the airfoil would take the form of a continuous vortex sheet of sinusoidally varying strength, stretching from the trailing edge to infinity in the downstream direction. In order to analyze airfoil flutter, rotorcraft aerodynamics and flapping flight kinematics, Theodorsen's theory became as a standard tool.

In the mid-1930s, the first theoretical explanation of drag and thrust generation to observe area of interest and the orientation of the wake vortices was undertaken by Von Karman and Burgers (Ref. [17]). Observing experimentally the orientation of the wake vortices, they concluded that a wake consisting of two rows of counter-rotating vortices (See in Figure 13) could generate a thrust force on an airfoil in an incompressible flow.
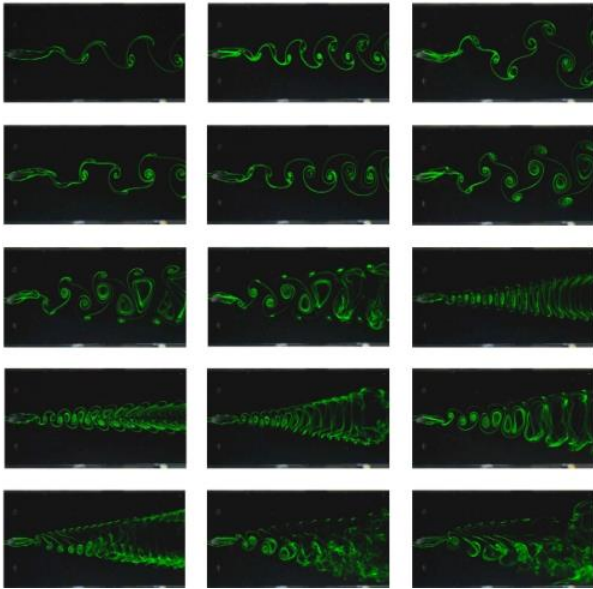


Figure 13. Dye visualizations of different wakes behind an oscillating airfoil (from Von Karman vortex, street, to neutral wake, to reverse von Karman vortex street, to deflected wake). (Ref. [17])

It should be noted that the linearized potential flow consist of a number of assumptions about **the flow**, which is inviscid and incompressible, **thin airfoil geometry** to treat as a flat plate and **the airfoil motion**. The last one is assumed to be of small amplitude and the wake does not evolve in response to its own induced velocity field.

In 1973, a biologist named Torkel Weis-Fogh conducted a landmark experimental study (Ref. [18]) of insect flight which was published to explain the high lift generation in the *chalcid wasp Encarsia formosa*. In that paper, a new mechanism for insect flight was identified by Torkel Weis-Fogh and then termed the Weis-Fogh mechanism, also referred to as the Clap-Fling. As this mechanism (see Fig 14.a-b) is commonly used in small insects at low Reynolds numbers and larger hovering animals usually use this mechanism an essentially normal hovering flight which is steady flow process. A detailed theoretical analysis of the clap-and-fling can be found in Lighthill (1973) and Sunada et al. (1993), and experimental treatments in Bennett (1977), Maxworthy (1979) and Spedding and Maxworthy (1986) (Ref. [10]).
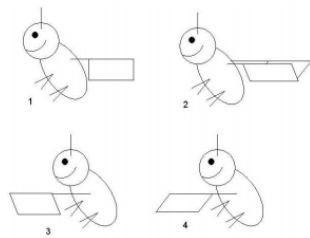


Figure 14.a. Schematic illustration of 2-D clap-fling mechanism (Ref [19])
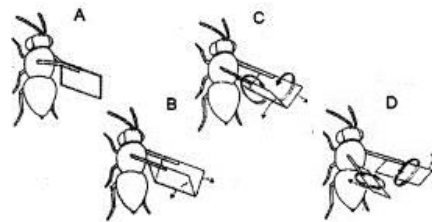
Figure 14.b. Schematic illustration of 3-D clap-fling mechanism (Ref [20])

Discrepancy between the Weis-Fogh's mechanism and normal hovering mechanism was pointed by Maxworthy in 1981 (Ref. [21-22]) that Weis-Fogh's steady state conclusion about normal hovering comes from the fortuitous cancellation of unsteady effects when averaged over a complete cycle. The investigation of hovering motion was divided into four categories: normal hovering (as a horizontal stroke plane), the clap-fling mechanism (as a horizontal stroke plane) named by Weis-Fogh, inclined wing stroke plane and vertical wing stroke plane.

19

From a numerous experimental investigation of hovering fliers such as rufous hummingbirds, motion begins with the downstroke and continues the end of the downstroke to the beginning of the upstroke. Up to now, the theoretical investigations of hovering flight on the animals to have being studied can be divided into three kinematic groups with respect to stroke plane, which are horizontal stroke plane, inclined stroke plane and lastly vertical stroke plane. Thus, kinematics of hovering flight is explained in three categories. Since normal hovering flight is an area where the wing stroke is approximately horizontal, hummingbirds and the majority of insects are generally examined in this group.

In nature, the most commonly observed type of hovering is defined by an approximately horizontal stroke plane as Figure 15.a. Up to now, this group has been extensively discussed by Weis-Fogh (1972,1973), who called the pattern normal hovering unlike Maxworthy and includes the hummingbirds (Stolpe&Zimmer 1939; Greenewalt 1960) and most of the insects (Weis-Fogh 1973) (Ref. [10]).
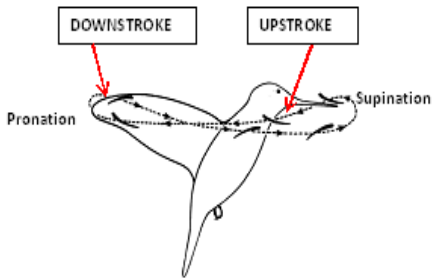


Figure 15.a. The wing tip path of hummingbird *Chlorostilbon aureoventris*. Black airfoil shapes represent the wing shape on the each location (Ref. [23])
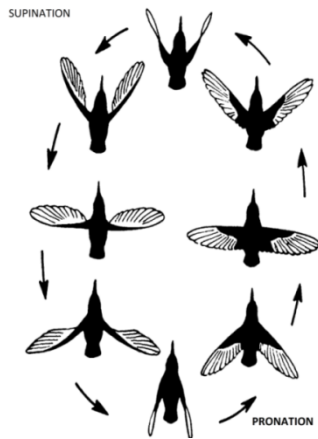
Figure 15.b. Schematic representation of wingbeat pattern for *Melanotrochilus fuscus* (Ref. [23])
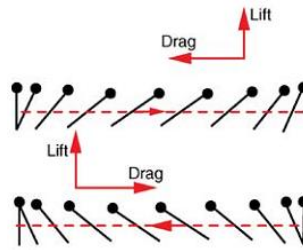
Figure 15.c. The schematic lift-drag diagram of normal hovering flight (Ref [24])

In 1997, a further study of Ellington et al. (Ref. [25]) was performed by Van den Berg and Ellington (Ref.[26]) to investigate the 3-D LEV of a "hovering" model *hawkmoth Manduca sexta* and the vortex wake of this model using smoke visualization mechanism. As seen in Figure 21, the smoke was distributed over the leading edge and the camera was mounted parallel to the wing surface. It was confirmed that the existence of a small, strong and stable LEV resulted in size increment from wing-base to wingtip due to the continuous roll-up of air into the vortex as a shape of the conical leading-edge vortex by separating from the wing at approximately 75 % of the wing length. However, the LEV became unstable at approximately 0.75R, where R is wing length, and then detached from wing surface. Especially, the tip vortex became very large during the downstroke, covering the outer 0.25R. Then, as seen in Figure 16 c, the strong axial flow of leading-edge vortex fed vorticity into the tip vortex during the transient air over wing, resulting in gradually building up a vortex ring in its wake.
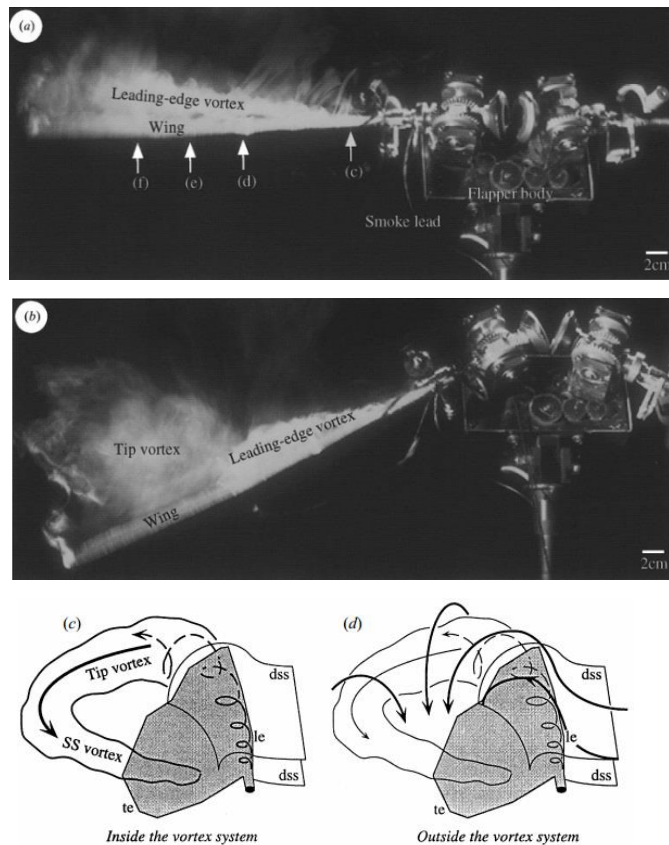
Figure 16. Flow visualization of the LEV over a wing of the "flapper" during the downstroke: a) The LEV at $\phi = 0°$. b) The LEV at $\phi \approx -25°$. c) The flow "dss" is inside the vortex system. (d) The flow outside the "dss (Adapted from Ref. [26])

It was not until the experimental study for the 3-D LEV of a "hovering" model *hawkmoth* of the species *Manduca sexta* performed by Van den Berg and Ellington (Ref [26]) that this served detailed information about the formation and roll-up of starting (sta) and stopping (sto) vortices during a complete wing-beat cycle as seen in Figure 17. The results revealed that at the end of the upstroke a stopping vortex was shed and during late pronation the hidden vortex then appeared from behind the wing and rolled over the trailing edge. This leads to a generation of starting vortex and then sheds from the trailing edge rolling up on the anatomical topside of the wing. However, during the downstroke, the combination of sta and sto (SS) vortex

22

decreased the strength vortex core, resulting in the connection with the SS vortex and tip vortex (see in Figure 16-c). The results indicated that the downstroke starting vortex was much stronger than the upstroke starting vortex which spiraled towards the stopping vortex and merging with the downstroke stopping vortex and then creating another combined SS vortex. Although the connection of the strong vortex rings of the downstroke with weak upstroke vortex rings validated with flow visualization results for the hawkmoth during near-hovering (Willmott et al. 1997), the upstroke wake was not sufficiently detailed by Van den Berg and Ellington.
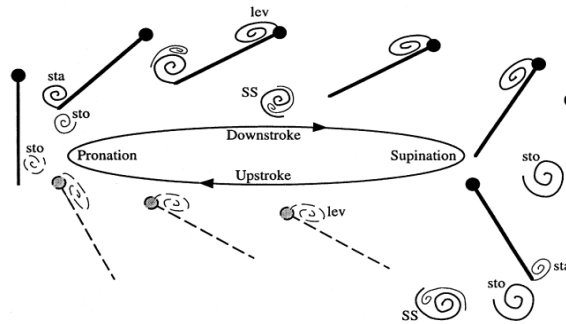
Figure 17. The representation for the formation and roll-up of starting (sta) and stopping (sto) vortices during a complete wingbeat cycle. Abbv : sta (starting vortex), sto (stopping vortex), lev (leading-edge vortex), SS (combination of sta and sto) (Ref. [26])

In 2005, characterization of vortex dynamics produced by the flapping wing in linear motion was analyzed by Kurtulus (Ref. [11]) using both DNS and PIV methods by means of a 2-D simplified analytical model which was symmetrical (NACA 0012). Throughout this study, the incompressible and laminar flow was assumed by changing with the Reynolds numbers between 500 and 2000 and with angles of attack varying between 5° and 60° with 15° increments . So, the predicted

forces could be optimized by the parameters of the motion leading to maximum force. During experimental measurements, the Reynolds number was 1000 and the angle of attack was 45°. The results indicated that in average on a period the total force coefficient was on the order of 2.5. On the other hand, especially for high angles of attack, this model could not give better results at the second part of the rotation, so that the used model could not analyze the interactions between produced vortices and the near field of airfoil. Thus, the requirements for 3-D model were emphasized, since 3-D effects in the vortex generation mechanism played a crucial role in realistic behavior of flapping wing.

In 2007 (July), a further study of Kurtulus (Ref. [11]) was performed by Sarigol (Ref. [13]) in order to analyze the flow which was incompressible, laminar flow at low Reynolds Number regime using DNS and PIV methods. Each measurements in hovering motion were taken in both 2-D and 3-D flapping wing. So, results of the numerical and experimental measurements could be compared for the same parameters such as angle of attack, airfoil profile and Reynolds number. From plenty of measurements, the effect of the profile thickness in symmetrical airfoils (NACA 0010 and NACA 0015) revealed that as the angle of attack increased, the absolute peak values of drag coefficients decreased for any given profile, but the absolute peak values of lift coefficients were increased especially for thinner profiles. In a meanwhile, as the thickness of profile was increasing, the attachment of LEVs and TEVs was decreasing with bigger rotational stopping vortex. Besides that, symmetrical airfoil for NACA 0012 at angle of attack of 60° had higher lift and drag coefficients than the cambered one for NACA 6412, whereas the cambered one at angle of attack of 45° was better. Moreover, the attachment of LEV was better in the symmetrical airfoil, while the shedding of LEV was rapidly detached in the cambered one. Notably, during pronation or supination, the cambered airfoil had higher values in the variation of lift coefficient with time. However, these variations for symmetrical airfoils were observed throughout the translational phase of motion. Nevertheless, in the 3-D experimental investigation of Sarigol (Ref.[13]) the wing was for single airfoil profile, aspect ratio and angle of attack. So, the

24

comprehensively investigation for the effect of wing profile or aspect ratio could not be performed.

The unsteady aerodynamics of insect wing motion has been a considerably issue in insect flight studies such that just for a specific wing motion and flight condition has been studied because of costly computations and sophisticated numerical techniques in the unsteady simulation of flapping wing motion. For this, an unsteady force production mechanism of insect by numerically simulating a realistic wing motion of blowfly was investigated in detail by Kim et. al. (Ref. [27]) in 2009 using e-Science infrastructure which was a special program. Experimental measurements were carried out in a wind tunnel using the blowfly, as kind of a tethered locust, in the front of tunnel under the free stream condition of 2.75m/s. As seen in Figure 18, during the experiments the wing motions were filmed by using a high-speed camera.
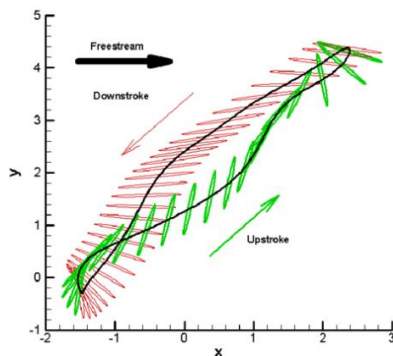


Figure 18 a. The figure-of-eight motion from wing-tip trajectories of the blowfly (Ref. [27])
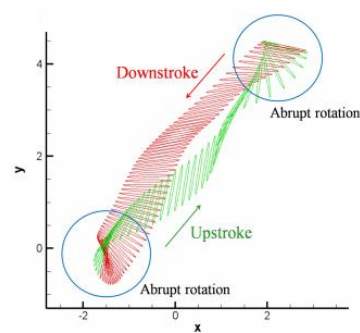
Figure 18 b. Non-sinusoidal pitch angle motion at the end of strokes in the figure-of-eight motion (Ref. [27])

During the numerical measurements, the instantaneous maximum lift coefficient, the instantaneous maximum thrust coefficient, the mean lift and thrust coefficients

were respectively found 3.355, 4.79, 0.689 and 0.146. On the other hand, the experimental measurements indicated that a ratio of lift to drag was 4.719 providing that the time-averaged thrust could be considered as the negative time-averaged drag because of the zero average horizontal force during the measurements of figure-of-eight motion. Taking into consideration both results of measurements, Kim et. al. (Ref. [27]) suggested that lift was significantly produced during the downstroke motion due to a high effective angle of attack, whereas thrust was unexpectedly generated at the end of the upstroke. The reason why the thrust was abruptly generated was that toward trailing edge a new CCW rotating vortex was developed from the shear layer, causing a transverse momentum induced by a strong jet between counter-rotating vortices which were moving downstream as a pair. Moreover, from extremely detailed numerical results and comparisons, the study showed that a production of thrust during the upstroke was obtained by the figure-of-eight motion, while a generation of lift during the downstroke was helpful in an inclined stroke motion due to the high effective angle of attack. Also, as for analysis of a wing sectional shape, they proposed that the camber effect could be beneficial only for hovering flight, because the cambered airfoil improves the lift production.

In 2009, the flow field of unsteady 2-D flapping wings making figure-of-eight motion in hovering flight was analyzed by Baskan (Ref. [14]) in incompressible, laminar flow at low Reynolds numbers using both the numerical (CFD) and the experimental (PIV) tools. The effects of parameters on the aerodynamic force coefficients and vortex formation mechanisms were investigated numerically using both wings having NACA 0012 and NACA 6412 airfoil sections at three different angles of attack (30˚, 45˚ and 60˚) at Reynolds numbers of 200, 1000 and 5000. In the experimental method two wings were examined for a Reynolds number of 1000 and for three different angles of attack. In the numerical methods, 2-D Navier-Stokes equations were solved by using the moving grid technique. In the study of Baskan (Ref. [14]), figure-of-eight motion of airfoils performed by using Lissajous curves which is the graph of a system of parametric equations describing a complex harmonic motion. From comparison between numerical and experimental data, the results showed that bulky LEVs and TEVs are produced in figure-of-eight motion

compared to linear flapping motion, especially in larger amplitude of motion in y direction. Besides that, interactions between both produced vortices in successive stroke do not occur, resulting in more strength vortices compared to linear flapping motion. On the other hand, the results indicated that the effect of Reynolds number and of camber do not substantially effect on aerodynamic forces and vortical structures. However, examination of the effects of vertical distance in the figure-of-eight motion was absent, since the experimental apparatus could not be able to move in y-direction.

In order to analyze the insects' hovering flight, many studies have generally examined on the aerodynamic performance of tethered locust such as bumblebee, hawkmoth, fruitflies. However, comparing to hovering insects, flight patterns of hummingbirds is similar to those of insects, though the hummingbirds are large-scale birds. In 2010 (January), 3-D vortex topologies related to aerodynamic performance were investigated by Liang et al. (Ref. [28]) using numerical (DNS) and experimental method (PIV). As an advantage of wing kinematics of hummingbird due to asymmetric motions throughout downstroke and upstroke, the hovering flight is performed at the Reynolds number regimes between $10^3$ and $10^4$ and at nearly 41 Hz flapping frequency. Thus, from investigations, it was found that during downstroke 75% of total lift is produced, while the remaining part of total lift is generated during upstroke. The wing configuration of which wing aspect ratio is 9.1 and kinematics used during the measurements are given in Figure 19. The results of measurements, this study revealed that the ratio of amount of lift generated during downstroke to that produced during upstroke is 2.95.
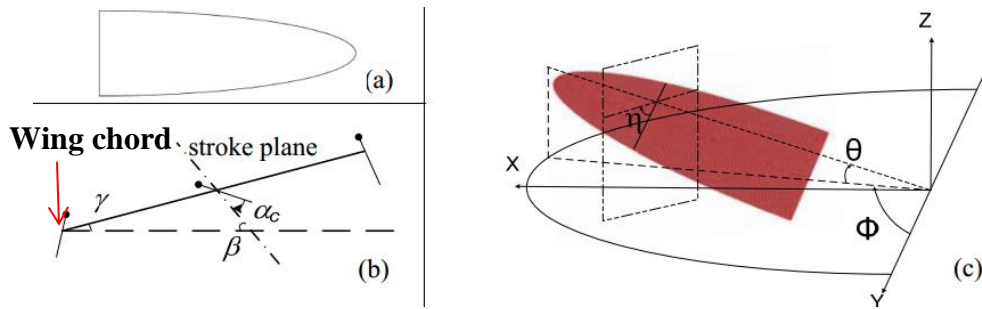
Figure 19.a. The profile of half elliptic wing; b- $\alpha_c$ is the chord angle, $\beta$ is the body angle relative to horizontal plane, $\gamma$ is the stroke plane angle relative to horizontal plane; c- $\phi$ is stroke angle, the coordinate system for hovering motions. (Ref [28])

Until 2013, numerical, experimental and theoretical studies of bats, insects etc. have been extensively examined their aerodynamic performance with related to hovering flight kinematics changing with their special flight patterns. Hummingbirds are not comprehensively investigated as much as these species. As mentioned before, hummingbirds are specialized hoverers to make a series of vortex rings the onset of downstroke. A further study of Warrick et. al. in 2005 (Ref.[29]), Wolf et al. in 2013 (October) (Ref.[30]) identified the structure of vortex wake in hovering Anna's hummingbirds by using PIV methods in both parasagittal and transverse planes. In the parasagittal plane, the starting and stopping vortices were measured to identify wing-stroke and the circulation of secondary vortices which is consistent with the shedding of LEVs created throughout downstroke. As seen in Figure 20, experiments carried out in a plexiglass flight cube having 0.9 x 0.9 x 0.9 m³. In order to prevent boundary effects the distance from hummingbirds to walls was chosen minimum 5 wing lengths.
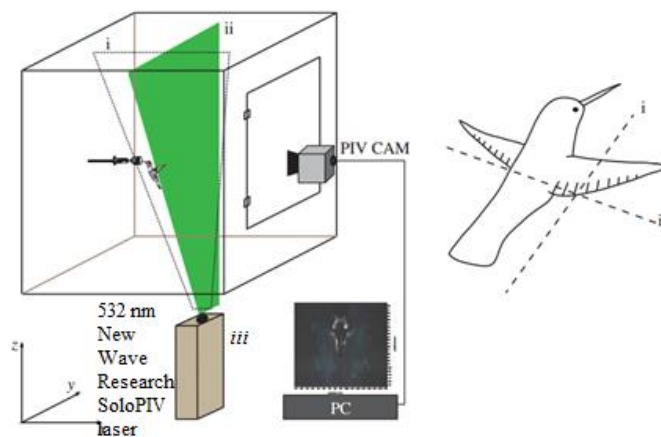
(i)   parasagittal plane
(ii)  transverse plane
(iii) a double-pulsed 50 mJ Nd:Yag laser running at a 15 Hz repetition rate with a 2 mm-thick laser plane. (but, wingbeat frequency is nearly 45 Hz)

Figure 20. The experimental setup (Ref.[30])

In the study of Wolf et. al. in 2013 (Ref.[30]) the examination of the wake vortex was divided into two ways as the development of the wake from wing root to wingtip and force production to support the weight. Contrary to a single vortex loop wake, individual ring structures with each stroke Anna's hummingbirds produced a bilaterally paired vortex loop by contributing force production through a wing beat and by supporting weight. As a result of the examination of wake vortex, the ratio of circulation of wing root to wing tip was approximately estimated 85%, whereas this ratio was only 42% for the slow-flying bats. Taking into account the uncertainty in prediction of velocity was nearly $\pm$ 1% and in vorticity $\pm$ 10%, the experimental studies of Anna's hummingbirds (Calypte anna) indicated that as vortices separate from root to tip, the circulation strongly increases up to 15 % throughout downstrokes. In fact, during downstroke the contribution of required weight support was estimated 66 $\pm$8 %, while this contribution was predicted 35$\pm$ 7 % throughout upstroke. Moreover, the structure of secondary vortex could supply to weight at the range of 8-26%. Generally, compared to downstroke, the behavior of vortex shedding was more continuous at the wing root during upstroke. However, Wolf et. al. in 2013 (October) (Ref.[30]) suggested that a 3-D PIV study should be studied to

resolve accurately wake structure, especially for the visualization of the vortex shedding throughout upstroke with the interactions between each stroke wakes such as up- to downstroke.

The lack of 3-D experimental investigation of vortex wake structure of flapping wings in hovering flight was resolved in the study of Cheng et. al. in 2013(November) (Ref.[31]) by using a single wing, resembling a wing of *Drosophila*. By using Volumetric three-component Velocimetry (V3V) process, vortex rings existing around a dynamically scaled flapping wing at the stroke reversal and significantly large drag due to revolving wings at large AoA were illuminated. For the experiments, the length and thickness of single wing was respectively 185 mm and 1.52 mm, leading to an aspect ratio of 6. As the wing was moving a sinusoidal function (See in Figure 21) with both strokes amplitude of 130° and the maximum wing rotation of 60°, the measurements were taken in the V3V measurement volumes (140 X 140 X100 mm$^3$), which covered a total volume of 420 X 276 X 354 mm$^3$ in the fixed Cartesian frame (X, Y, Z) at the Reynolds number of 2200 and at the wing beat frequency of 1/3 Hz. The test chamber, which was filled with mineral oil, made from an acrylic tank with transparent walls and transparent wing so as to capture vortex formation both the near and the far field of a flapping wing having the dimensions of 610 X 610 X 3050 mm$^3$ in terms of width X height X length.
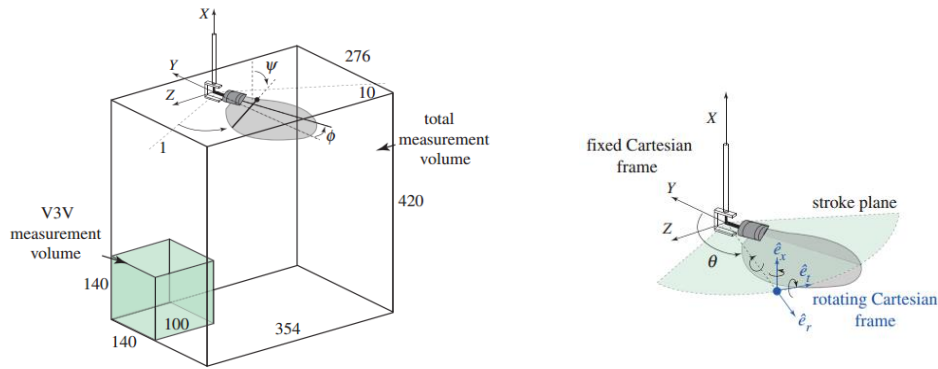
Figure 21. The experimental apparatus in the rotating Cartesian frame. The vertical axes ($\hat{e}_x$), the radial one ($\hat{e}_r$), the tangential one ($\hat{e}_t$ ). The last two components changing with the azimuth angles ($\theta$) of the particles of interest. (Ref.[31])

From this study of Cheng et. al. (Ref.[31]), a notably result from Q-criterion method is that between successive strokes produced trailing edge shear layer and root vortex do not connect with the starting or tip vortices to make the a closed vortex ring. In other words, the tip vortices and root vortices are not interact with the shedding radial vorticities in starting and stopping vortices, resulting in the absent of the formation of a closed-loop structure. Even, the wing-attached LEV smoothly interacts with tip vortex at the wing tip, while the shedding vortex from the wing trailing edge (trailing edge shear layer) quickly rolls up into root vortex. Then, the rolling up trailing edge shear layer into root vortex cause the formation of vortex system which contracts radially but expands tangentially in the wake. Also, the study of Cheng et. al. (Ref. [31]) put into evidence the stabilization of LEV or the magnitude variations of vortex that is substantially affected by both the induced downwash and the vortex compression, unlike spanwise flow. However, in this study, it was unclear whether wake patterns are affected by Reynolds number, wing profile or wing kinematics.

# CHAPTER 3

# EXPERIMENTAL METHOD AND SETUP

A number of different measurement techniques are developed to measure the flow around the body in entire volume, sufficiently. To calculate the velocity vectors as well as scalar quantities in the flow, the flow measurement techniques can be divided into two groups; as intrusive techniques and non-intrusive techniques. The reason why the former called as the intrusive techniques is that the instruments are located in the flow disturbing the flow. Similarly, locating the instruments outside the flow, this technique is named as the non-intrusive method.

Among all measurement techniques, Particle Image Velocimetry (PIV) is used to measure the flow both qualitatively and quantitatively instantaneously. The major advantages of the PIV technique are given as follows:

- Since the appropriately selected seed particles do not disturb the flow, the seed particles play role on flow measurement as probes in PIV measurements.

- Multiple instantaneous whole flow field velocity images enable visual validation of flow patterns to understand flow phenomena whole flow field.

- Large quantities of image pairs in a relatively short period of time are generated and can be analyzed just in time or later.

- High degree of accuracy is obtained providing that each vector is the statistical average for many particles within a particular tile**.**

Taking the advantages of PIV measurements into account, this technique is plausible in order to investigate the vortex shedding mechanism from the leading and trailing edges of the airfoil.

This chapter gives information about principles of PIV measurement, 3-D PIV Measurements and experimental setup.

### 3.1. Principles of PIV Measurement:

PIV is able to capture the instantaneous flow field. One of the most important advantages is that it allows to record images of whole velocity flow field, instead of the measurement a single point like Laser Doppler Anemometry (LDA) or Laser Doppler Velocimetry (LDV).

Its principle is based on the quantification of the displacement of small tracer particles which are carried by the fluid during a short time interval. The instantaneous whole field velocities are based on the well-known equation:

$$speed = \frac{distance}{time}$$ (Eqn. 3.1)
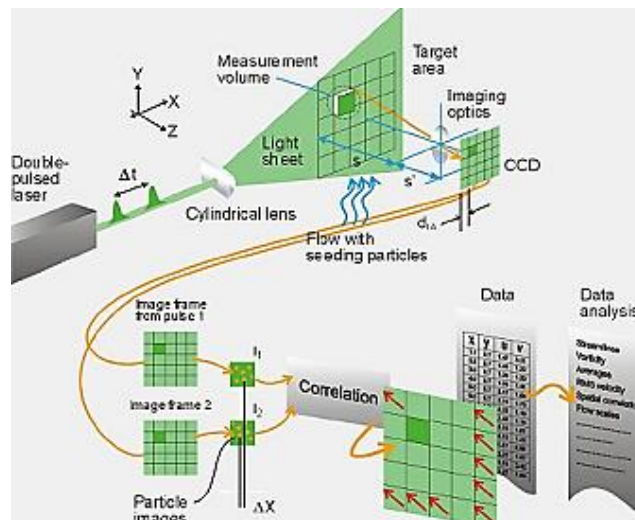

Figure 22. Basic principles of PIV (Ref. [32])

As given in Figure 22, the PIV technique can be divided into seven main sections; **seeding, illumination, cameras, synchronization, resolution, correlation and validation**. In order to visualize the vortex structures of the flow, the particles, which are often called as "seeds", are inserted into the flow. The seeding particles must be

34

able to match the concentration of the fluid particle so that the tracers can follow into the local flow velocity between the two illuminations. Thus, the particle size should be accurately balanced to scatter enough light to visualize all particles within the laser sheet plane, but small enough to follow the flow. Also, the tracer particles should be visible, so that the images of illuminated particle can be recorded. In this study, Silver Coated Hollow Glass Spheres (S-HGS) which is appropriate for liquid flow applications is used. The reflectivity is increased thanks to a thin silver coating further. The specification of this seeding particle (S -HGS) is shown in Table 2.

Table 2. Specification of seeding particle (Ref. [33])

| Mean particle size (µm) | Size distribution (µm) | Particle shape | Density (g/cm3) | Melting point (°C) | Material |
|---|---|---|---|---|---|
| 10 | 2-20 | Spherical | 1.4 | 740 | Borosilicate glass |

The illumination system, which is a combination of laser and optics, illuminates the flow field in the interest region with a narrow light sheet. By means of optics including a set of cylindrical lenses and mirrors, a beam shape of light source is transformed into a planar sheet to illuminate the flow field. The light sheet is permanent, but pulsed to produce a stroboscopic effect. During its exposure to the light-pulse, the pulse duration has to be able to catch the particles as dots rather than streaks. Also, not to see the flow fields as moving, the time between successive light pulses should be correctly selected. A difference between the successive light pulses determines the displacement between the initial and final positions of the seeding particles.

During the experiments, as a double-cavity Q-switched Nd:YAG laser "New Wave Solo PIV 120 XT"(see in Figure 23-a) is used to obtain pulsing light-sheets.

35

The laser is used as light source in PIV systems which can easily be collected into thin light sheet for illuminating and recording the tracer particles. The maximum output energy of the laser is 120 mJ per pulse at 532 nm wavelength and pulse duration of it is 3-5 ns. To increase the optical transmission of pulsed laser radiation, a high power laser guide (see in Figure 23.b) is used. The features of laser are given below.



Figure 23-a. New Wave Solo PIV 120 XT-532 nm



Figure 23-b. Flexible high powered light guide

Table 3. Specification of New Wave Solo PIV 120 XT (Ref. [34])

| Repetition Rate [Hz] | 532 nm | | Beam Diameter (mm) | Pulse Width (ns) | Divergence (mrad) | Beam Pointing Stabilitiy (urad) | Jitter (±ns) |
|---|---|---|---|---|---|---|---|
| | Energy (mJ) | Energy Stability (±%) | | | | | |
| 15 | 120 | 4 | 4,5 | 3-5 | <3 | <100 | 1 |

The typical optical configuration of PIV setup includes a light source (usually a double-pulse laser), light sheet optics (converting the beam shape of light source into a light planar sheet by optics), the tracer particles and cameras (imaging lens and recording media). Up to now, the first four have been mentioned. A CCD camera (Charged Coupled Device), which is the last part of the configuration of PIV setup detects the position of the illuminated seeding particles. The particle positions appear as light specks on a dark background on each camera frame. The image optics (see in the Figure 24) and the time interval are presented in the denominator of the equations as below.
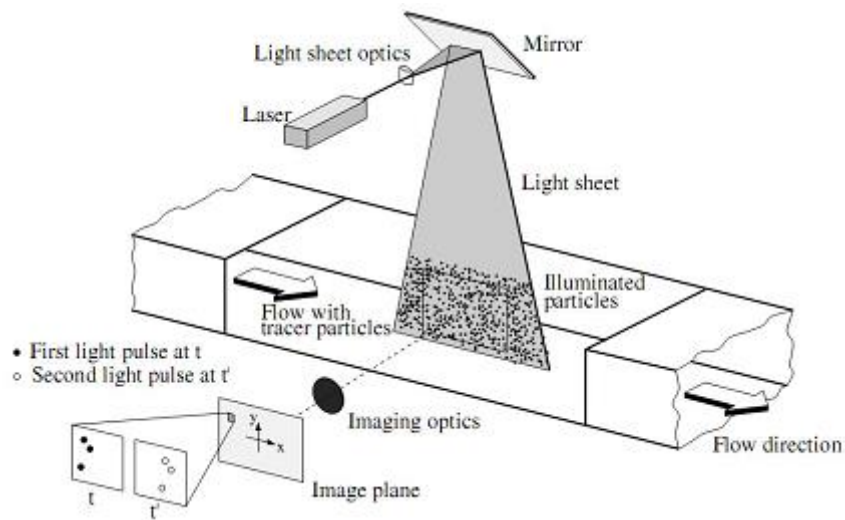


Figure 24. Experimental arrangement for PIV investigation of the area of interest

(Adapted from Ref. [35])

$$u(x,y) = \frac{\Delta x}{\Delta t}$$ (Eqn. 3.2.)

$$v(x,y) = \frac{\Delta y}{\Delta t}$$ (Eqn. 3.3.)

37

Each camera has its own personality module, which provides an interface between the camera and the rest of the system. Also another main part of the system is the input buffer whose property is as follows: simultaneously reading image maps from a CCD camera, storing images in memory, and either sending the entire image directly to the PC, or dividing the entire image into smaller sections and sending these to the correlator unit. Briefly, the input buffer by means of this personality module receives image maps from the camera, and gives these to the correlator for vector processing. Throughout the experimental research the HiSense MkII camera is used. The specifications of cameras having approximately 640 gr weight of camera head are given below.

Table 4. The specifications of HiSense MkII Camera (Ref. [36])

| Imaging Device | Effective No. Of Pixels | Cell Size | Effective Area | Frame Rate | A/D Converter |
|---|---|---|---|---|---|
| Progressive scan interline CCD with micro-lens | 1344 X 1024 ( H X V) | 6.45 µm x 6.45 µm | 8,67 mm x 6.60 mm (2/3 inch size) | 12.2 Hz | 12 bit |

Synchronization between the CCD-cameras and the laser is performed by the synchronization board to synchronize all activities in the PIV-system. So, this provide connections and communication links to the users own devices as well as the illumination system and the camera. The synchronization procedure is indicated in Figure 25.
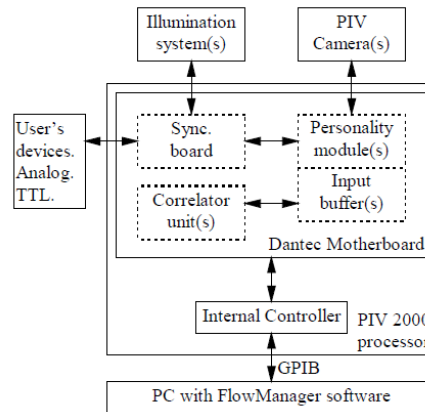
Figure 25. The schematic presentation of synchronization procedure (Ref. [32])

Synchronization between the CCD-camera and the laser provides that the first image acquired at the first light pulse of the laser is saved on frame 1 of the camera, and that the second pulse is saved on frame 2 of the camera. This procedure is called as double frame or double exposure. The difference of both photos, which was captured at each time as the initial and final positions of particles in the flow, gives the displacement vector of the particle. In this study, the experiments are performed by double frame procedure.

After gathering the images on two frames, the velocity of the particles is calculated by determining interrogation areas or region. To achieve this, each camera images are divided into rectangular subdomains so as to find out displacement vectors of each particle. The displacement of both images is determined by correlation technique-FFT (Fast Fourier Transform). Capturing the first image at the first pulse of the laser and the second image at the second pulse of the laser, the average displacement of each particle can be calculated within a specific short time interval. Performing this for all interrogation areas, a vector map of average particle displacements is obtained. Dividing with the known time interval, the displacement vectors are converted into a map of so-called "raw-velocity vectors". The cameras role in the PIV measurement process is given in Figure 26.

It should be noted that pre-processing method consists of an optimal image processing, implying a homogeneous seeding, uniform illumination and uniform image background during data acquisition process.
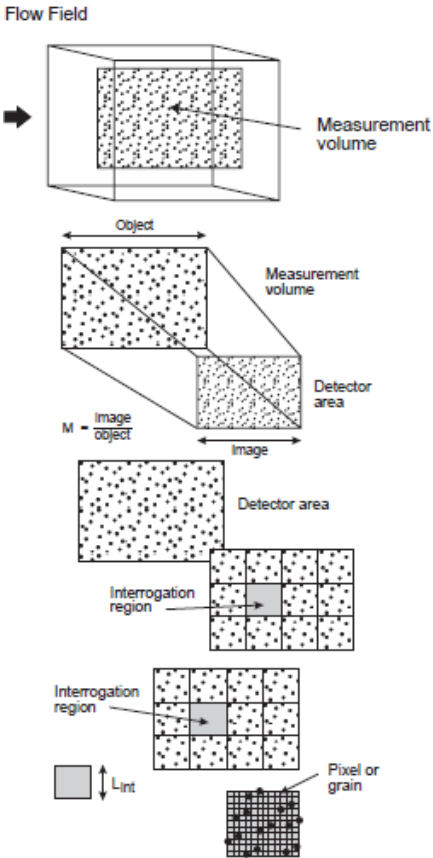


Figure 26. Cameras' role in the PIV measurement process (Ref. [32])

During the correlation process, the correlation plane is scanned and the possible highest/signal peaks are then detected. In here, if the smaller interrogation area is selected, the position of the signal peaks is determined by using an interpolation routine. Obviously, the selection of analysis options, particularly the size and overlap of the interrogation region as well as the pixel array size of the selected PIV camera

affect analysis time of a given vector map. For this, all of them should be properly optimize not to evaluate again the given vector map. A schematic illustration of correlator unit is given in Figure 27.
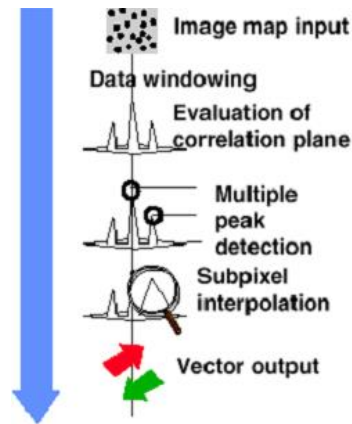


Figure 27. The schematic illustration of Correlator unit Ref. [32]

Different correlation techniques can be used such as auto-correlation, cross-correlation and adaptive correlation. Adaptive correlation technique is superior to cross-correlation, even though the computational cost of cross-correlation is much lower. Adaptive correlation is much more suited for this study, since adaptive correlation technique enables to acquire more successful vectors in a larger area by using "iteration and overlapping interrogation areas". Thus, this results in suitable interpolations, which are of great help when calculating derived quantities such as streamlines and vortices from the vector map. The overlapping interrogation areas process retrieve the information destroyed by windows, as illustrated in Figure 28.

41
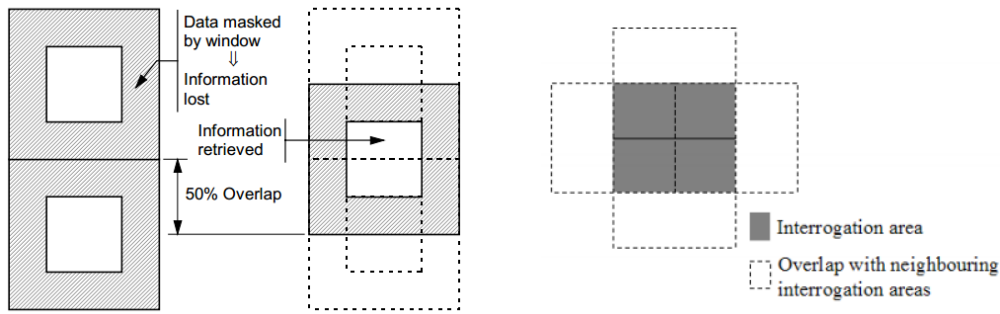
Figure 28. The left one explains the principle of the overlapping interrogation areas, while the right one describes that the overlapping areas can be either horizontal or vertical neighbouring interrogation areas. (Ref. [32])

The fundamental principle of adaptive correlation is an iterative procedure. For this, as seen in Figure 29, interrogation area from in the image frame I1 capturing at time t is shifted to interrogation area from in the image frame I2 capturing at time t + Δt by using an initial guessed offset value and selected interrogation area size. So, acquired velocity vector is validated to make estimation for the new correlation area offset. Then, a new correlation process is performed for a smaller interrogation area until the final interrogation area size is reached. If the iterative procedure is carried out twice, taking the interrogation area size of 128x128 pixels, the final interrogation area size will be 32x32 pixels. In addition to iterative procedure, a relative overlap among neighboring interrogation areas is termed as "Overlap–Horizontal/Vertical" parameter, as illustrated in Figure 28 for (H-50%, V-50%). The horizontal and vertical overlaps can be independently set, offering total freedom to increase vector map resolution in any direction. In this study, the overlap is taken as 50 % which is the usual recommended value, since double exposure is used.
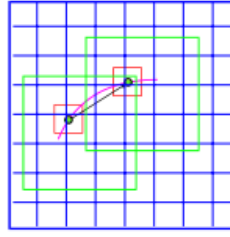
Figure 29. The representation of window offset Ref. [32]

Because of PIV as an instantaneous measurement technique, it should be noted that there will be an output data whether the input data are meaningful or not. As a result of this, the acquired vector maps which are attained after the correlation are corroborated. This explains why the acquired vector maps are named raw vector maps. In order to improve the vector maps, the latest part of PIV technique, the validation method is applied. During validations, the incorrect velocity vectors as inputs are recognized, rejected, removed and then the more correct velocity vectors are replaced.

Throughout the validation methods, the sufficient part is substitution which performs removes the rejected vectors and substitutes more correct vectors which is estimated from the surrounding measured vectors. The validation methods depending on logical mathematical algorithms include peak height ratios, velocity range validation, moving average, manual validation of vector maps and masking.

### 3.1.1. 3-D PIV Measurements:

In traditional 2-D PIV methods, the flow measurements are performed locating the optical axis of the recording lens to perpendicular to the area of interest, which is defined by the laser light sheet. In 2-D PIV the third component of the velocity field can not be accounted, since the velocity vector which is projected into the plane of the light sheet is lost. For 2-D measurements one camera can give reliable results, while a second camera adding to 3-D PIV methods allows the recording images to view the flow which was defined by the laser sheet from a specific angle.

43

The fundamental principle of 3-D PIV system, called as Stereo PIV, is based on the Scheimpflug principle. As seen in Figure 30 the Scheimpflug arrangement is a kind of perspective distortion. Each camera obtains different 2-D information about the same object, by recording captured by two cameras pointed at the same object from a different point of view (see in Figure 31). Then 3-D information about recorded object is obtained by combining or overlapping the information of two cameras (see in Figure 32). Briefly, intersection at a common point or focus at the image plane is realized by three planes-which are the object plane, the image plane (CCD-plane) and the plane of the imaging lens. Therefore, the velocity vectors are converted from images to non-distorted fluid space, as long as the camera is correctly focused by using Scheimpflug condition.
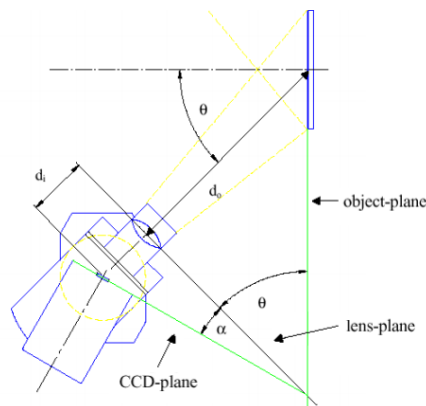


Figure 30. The Scheimpflug principle (Ref. [37])

In 3-D measurements the cameras are positioned at the specific angles to the light sheet to acquire three dimensionalities, while in 2-D measurements the camera is placed at right angles to the light sheet. In order to be sure how much points in the object plane are clearly imaged onto the CCD-plane, calibration procedure is carried out for each camera in Stereo PIV methods. For this, by means of calibration target

including a grid of dots (see in Figure 34), a well-defined grid of dots is obtained, as long as the each dots is clearly seen. The calibration images simultaneously taken from both cameras are served in Figure 32.
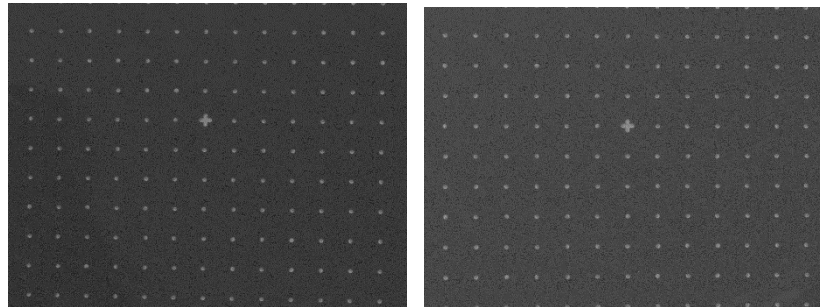


Figure 31. During experiments, the left side is the Calibration Image 1 captured from Camera 1 , the right one is the Calibration Image 2.
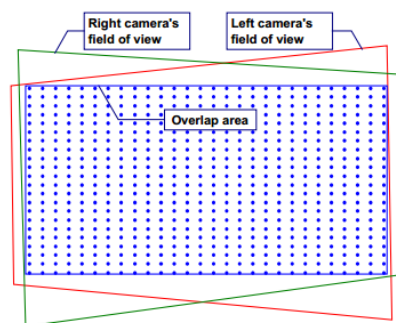


Figure 32. Overlap area from two images Ref. [37]

In this study, the design of HiSense MkII camera mount (see in Figure 33) enables us to tilt the CCD plane relative to lens plane around CCD axis. Otherwise, it is not possible with ordinary cameras.
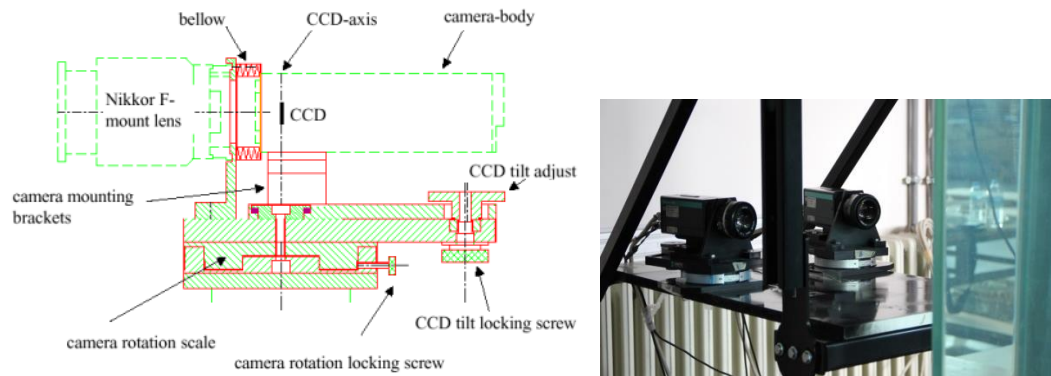
Figure 33. The HiSense MkII CCD cameras mount (Ref. [37])

In Figure 34, the calibration target, which is used in the experiments, is the multi-level target containing a two-level grid of white dots on a black background. Each grid in the calibration targets defines the coordinate system. As seen below the center of plane, which is the origin of the coordinate system at (0,0,Z), has larger dot surrounded by four smaller dots which identifies the x- and the y-axis. In order to perform successful calibrations, both cameras must be able to see the large dot surrounded by the four smaller points.
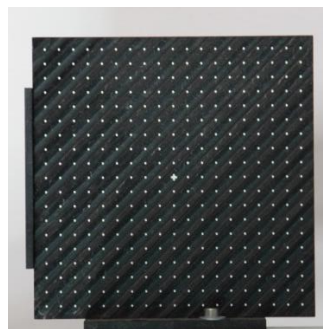


Figure 34. Double-sided multi-level target

Before starting with measurements, the plane calibration target must be aligned with the light sheet. Assuming that both cameras are on the same side of the light sheet, the position in which the calibration-plane is centered in the light sheet equals Z=0, while positions closer to the cameras are normally considered positive (Z>0) and positions further away from the cameras are considered negative (Z<0) (see in Figure 35).
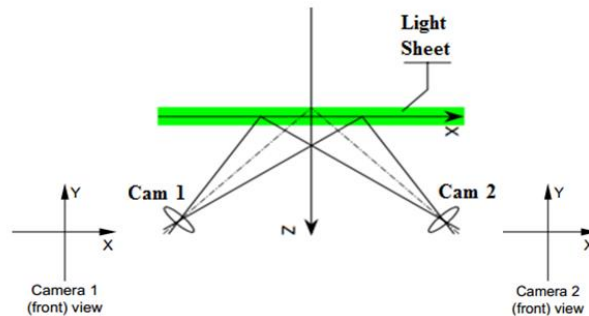


Figure 35. The orientation of each camera as top view. Direction of Z-axis is positive towards cameras (Ref. [37])

It should be noted that the accuracy of the calibration depends on the quality of the calibration images. Therefore, the calibration target illumination should be uniform and bright giving a good contrast. Also, the calibration target should be as large as the field of view. A number of experimental studies have shown that around 100 visible dots give reasonable results for each calibration image in order to obtain the best possible calibration. To maximize the overlap between the two camera images, the steps should be performed:

- centering the larger dot in both the left and the right image
- keeping the same object- camera distance for both cameras
- keeping the same camera height in the non-Scheimpflug-plane

- tilting the cameras until the same number of dots should be seen from left and right sides of the large dot in both camera images. (Generally, the results of 3D-PIV measurement are reasonable in case of camera viewing angles of $\pm 30°$ or even at of $\pm 15°$.)

Since the more accurate alignment of the light sheet and the calibration target enable us to obtain the more accurate the stereoscopic re-combination of the two 2-D vector fields. If the Scheimpflug condition is not achieved by the criteria that mentioned above, either right cameras field of view or left one likes in Figure 36:
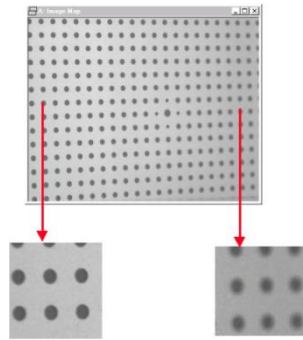


Figure 36. The illustration of badly obtained Scheimpflug condition (Ref. [37])

During the experiments, the Scheimpflug condition can be satisfied by two methods:

- Both cameras are adjusted the CCD tilt angle at the back of the camera mount to the calculated value. This calculation is :

$$\alpha = ArcTan[\frac{f_{lens}.tan\theta}{d_0 - f_{lens}}]$$ (Eqn.3.4.)

$f_{lens}$: Focal number of lens

$\theta$    : Rotational scale of the camera mounts

$d_0$ : Approximately the distance between the centre of the lens and of the calibration target

- Another way is that the best possible focus over the entire image is achieved by focusing at the center of object image and tilting the CCD-plane for both cameras. Thus, a significant peak at histogram values for the black dots indicates the best focusing.

During Stereo PIV measurements, three displacements ($\Delta X, \Delta Y, \Delta Z$) are extracted from a pair of 2-D displacements ($\Delta x, \Delta y$) and 4 equations with 3 unknowns is therefore solved by FlowManager 3-D PIV, which provides polynomial imaging models. Nevertheless, this model is linear with respect to Z. The n'th order XY-Polynomial allows the user to define polynomial order in the range 2-9.

It should be taken into consideration that the polynomial imaging models are strictly empirical, resulting in no physical arguments to justify their use. However, the experiments provide better results than the Direct Linear Transform (DLT).

### 3.2. Experimental Setup:

The experimental set-up was built in Aerospace Engineering Department of Middle East Technical University. Experiments were performed in a 1m x 1m x1.5m water tank made of altuglass in order to use PIV method as a nonintrusive experimental technique.

A cambered NACA 6412 airfoil section (see in Figure 37) having an aspect ratio of 5 (a span of 30 cm and the chord length of 6 cm) was chosen for this study, so that the aspect ratio for hoverers is altering from 3 to 11 in the literature. For instance, a typical dragonfly's wings have an aspect ratio of 11. The reason why we used this airfoil is that the cambered airfoil profile has plenty of advantages than the symmetrical one in hovering flight making figure-of-eight motion. The notable one is in the study of Sarigol (Ref. [13]) the cambered airfoils overcame higher absolute peak values of both lift and drag coefficients at high angles of attack compared to the symmetrical airfoil. The other one is that the cambered airfoils had higher values in terms of the variation of the lift coefficient with time during the reversal rotational phases of the motion. Depending upon the nature of living creatures, the hoverers generally has the cambered airfoil profile, when they make the figure-of-eight motion in hovering flight.
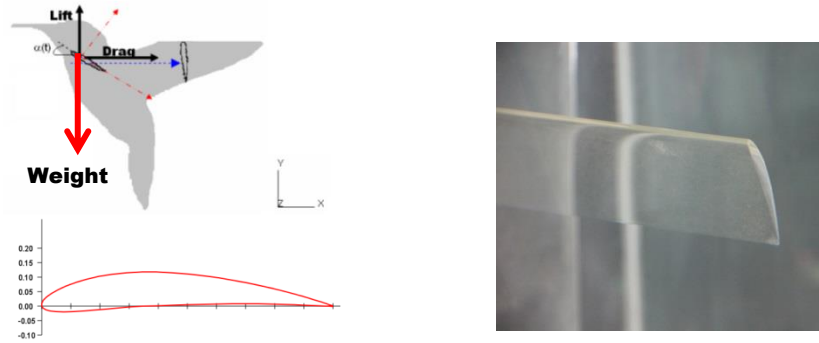
Figure 37. The left side is the illustration of 2-D cut of a wing section of NACA 6412 (Ref [38]). The right side indicates the cambered airfoil which was used during the experiments.

As one end of the wing model is attached to an end plate which has 90 cm long and 50 cm wide, the other one was set free in the flow field to create the 3-D behavior around the wing model (see in Figure 38). The experimental wing model and the end plate are made of plexiglass. Transparent materials reflecting the laser sheet in the measurement volume allow the seeding particles in the laser sheet to be captured by cameras in both suction and the pressure sides around the airfoil.



Figure 38. The end plate with model wing

During the experiments, the wing and the endplates assembly were translated together by an accurate translational mechanism placed above the tank. The model was set to rotate about its center of rotation point which is placed at 1/4c. The whole experimental setup is shown in Figure 39.
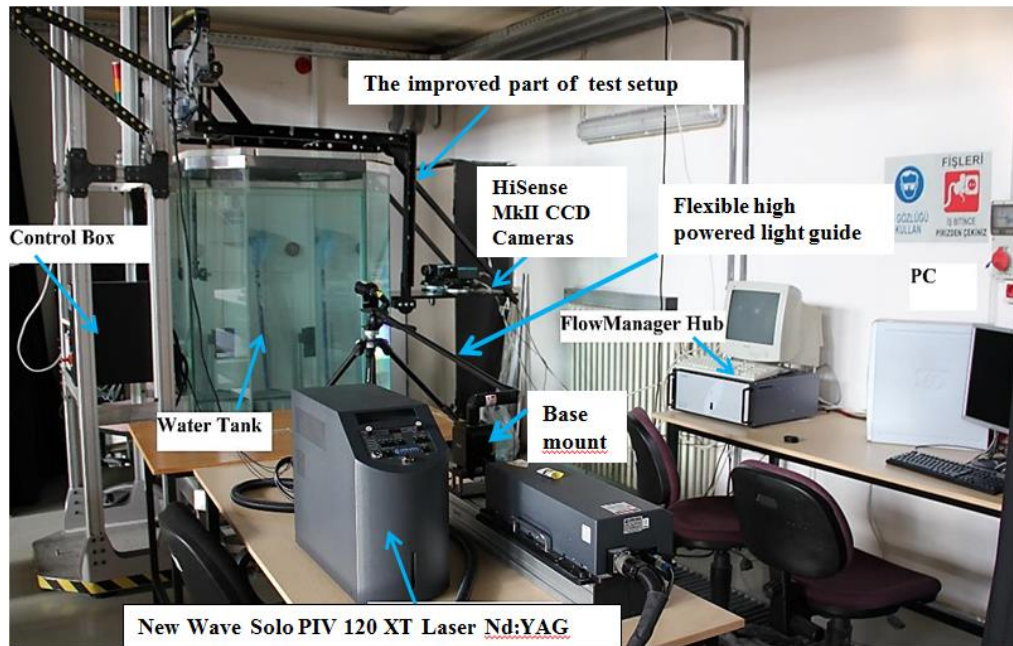


Figure 39. The modified experimental setup used during 3-D experiments

The PIV measurements were performed at three different spanwise planes, as given in Figure 40. A distance between locations is equal to a chord length of wing. Since the 3-D measurements entail the cameras to see the illuminated plane at different angles, the viewing angles of each camera are changed with each spanwise location. Therefore, each calibration procedure should be carefully fulfilled to get accurate measurements. The cameras are approximately 70 cm away from the water tank with the focal number (F) of 1.4.
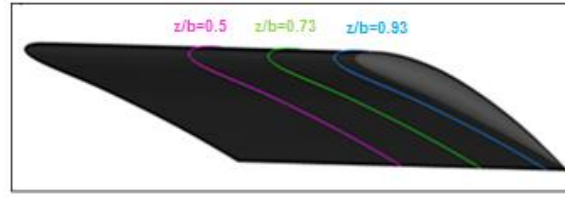
Figure 40. A representation of the spanwise locations which were performed during 3D measurements. (Ref. [13])

In this experiment the Nd:YAG laser is used, since the illumination energy density in the water flows is not dependent upon the time between pulses. The time between successive flashes is 80 000 μs yielding the particle can move nearly 3 mm. With the help of the HiSense MkII CCD cameras, operating at double frame, two images are taken at each time. This makes an extended control range of exposure time, which is 500 ms in this experiment.

The speed and the actual displacement are controlled by the control program by measuring at the center of rotation point at every 50 milliseconds.

In the experimental setup, cameras were mounted on a bar carrying the wing. As the wing is moving, the cameras are moving with the same velocity by the advent of a special configuration (see in Figure 41). Different from the experimental setup which was performed by Sarigöl (Ref. [13]), the experimental setup was improved by means of linear bearings taken from SKF and a special design of Sait Özbiçer. Utilization of moving cameras simultaneously with the moving wing facilitate the 3-D measurement, since the measurements only for one wing at angle of attacks of α=30°,α=45°, α=60° and Re=1000 entail sensitive calibration and measurement technique at each spanwise location throughout the figure-of-eight motion.

Figure 41. The improved part of experimental setup

### 3.2.1. Experimental Conditions:

As stated in calibration procedure, the accuracy of the calibration is based on the quality of the calibration images. Thus, for every experimental measurement, a calibration of whole experimental system is required. For this, the following sequences shall be carried out in the sequence given as below:

- Provide the seeding particles spread homogeneously in water tank. Especially, the water should be mixed, if the seeding particles subside in the water tank.

- For all experiments (at the each different case of experiments), adjust the alignment between the camera position and the wing section which is the interest region.

- Align the light sheet of laser to the wing section where the measurements are taken from the spanwise location.

After completing the above steps, the wing model moves from point 8 at α=90° with 14,167 m/s at the beginning of the motions. The experimental conditions of present study for the figure-of-eight motion (see in Figure 42) are summarized in Table 5.
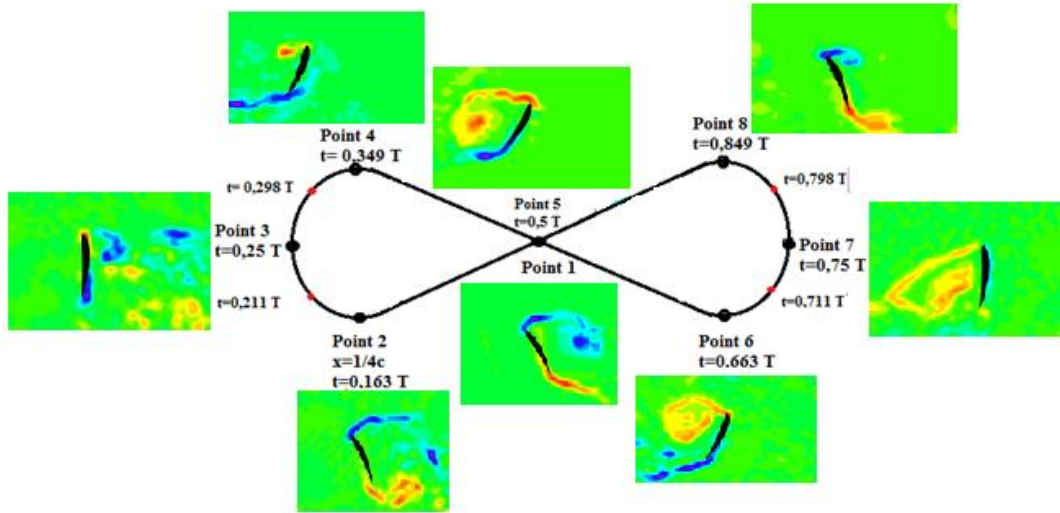
Figure 42. For one full period, the images taken from the 2-D flapping wing having a cambered airfoil (NACA 6412) at α=60° and B=c, Re=1052 (Ref. [14])

Throughout the experiments, the quantitative flow images are captured with both 12 bit Hi-Sense cameras with 1344×1024 pixel resolution and 12.2 Hz frame rate. Both cameras are mounted on a plate moving simultaneously with the wing by the same moving mechanism. With help of the configuration, whole field of view around the flapping airfoil is captured, resulting 246.2mm x 187.5mm the physical measurement plane for each camera.

In contrast to 2-D measurement principles, in the 3-D measurements the laser sheet should be thicker to illuminate a volume from rear to fore of the wing as a half of volume of width. During the experiments, nearly 11 mm volume thickness is illuminated by starting from rear of the wing at z= -Z/2 (-5.5 mm) to fore of the wing at z=+z/2 (+5.5 mm). Hence, calibration images are taken from three different positions which are a center the light sheet equals Z=0, the positions closer to the cameras (Z>0) and positions further away from the cameras (Z<0).

Table 5. The experimental conditions of current study

| Wing model | Airfoil Type | NACA6412 |
|---|---|---|
| | Chord [m] | 0,06 |
| | Span [m] | 0,30 |
| Flow | Fluid | Water |
| | Temperature [°C] | 21 |
| Motion | Period [s] | 55(the amplitude of B=c) 64 (the amplitude of B=2c) |
| Seeding particle | Type | S-HGS |
| | Diameter[μm] | 10 |
| | Concentration [g/cm3] | 1,4 |
| Laser | Type | Nd:YAG |
| | Pulse Energy [mj/pulse] | 30 |
| | Laser Sheet Thickness [mm] | 11 |
| Recording | Camera Type | HiSense MkII |
| | Number of Camera | 2 |
| | Lens Focal Length [mm] | 50 |
| | F number | 1.4 |
| | Frame Rate [fps] | 12.2 |
| | Δt/T (non-dimensional time step) | 0.01 |
| | Resolution [pixels] | 1344x1024 |
| | Dynamic Range [bit] | 12 |
| | Exposure Delay Time[μs] | 80000 |
| | Exposure Time [ms] (time between two successive images) | 500 |
| Interrogation | Method | Double Exposure Adaptive Correlation |
| | Resolution | Initial :IA =128 x 128 pixels with N=2 Final: 32x32 pixels each with 50% overlap for both horizontal and vertical |
| | Validation | Local Neighbourhood Validation: MxM area is set 3 with both n= 3 iterations |

# CHAPTER 4

# EXPERIMENTAL RESULTS

This chapter presents the experimental results of the figure-of-eight motion in hover by analyzing the effect of the counter-rotating vortices in 3-D flow field on the vortex shedding mechanism and by examining the evolution of these vortices along the spanwise direction. The results are also compared with the previous studies performed Cekinmez (Ref. [15]) for 2-D flapping wing making the figure-of-eight motion.

Different from 2-D measurements which was performed previously (Ref. [15]), 3-D vortex regions around the cambered cross-section of NACA 6412 airfoil are observed from wing root to the wing tip at three different spanwise locations, by using Stereoscopic Particle Image Velocimetry (SPIV) technique. As stated before, the distance between locations (see in Figure 40) is determined a chord length of wing to investigate the velocity along spanwise direction. To overcome the periodicity of the flow field around the wing model, the experiments are performed and analyzed after the 7th period of flapping motion at three different angles of attack of $\alpha=30°$, $\alpha=45°$, $\alpha=60°$ and at a Reynolds number of Re=1000.

During the figure-of-eight motion, the airfoil moves both in the horizontal (x) and inthe vertical (y) directions. The schematic representation of the flow pattern during the figure-of-eight motion is given below. For the detailed definition of the motion, the kinematics of the figure-of-eight motion is introduced in Section 1.1.2.2 in terms of a non-dimensional period of the motion.
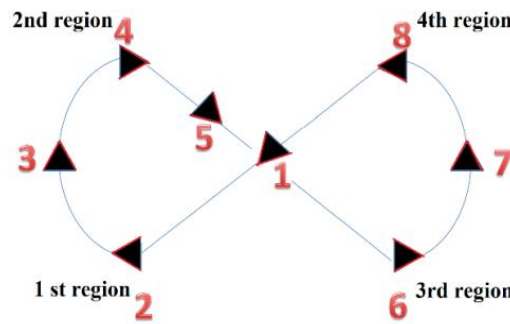
Figure 43. The schematic representation of Lissajous curve during figure-of-eight motion

The vortex shedding mechanism during the figure-of-eight motion can be explained as follows:

- The 1$^{st}$ region of the motion (between points 1 and 3) is only the half of the downstroke as the translational phase. Leading edge is pointing in positive direction by following the half-upstroke such that the LEVs (see in Figure 44)-which are formed at the leading edge- are rotating in CW direction, whereas the TEVs (see in Figure 44) or translational vortices- which are formed at trailing edge- are generated rotating in CCW direction.

- In the 2$^{nd}$ region (between points 3 and 5) after reaching the minimum angle of attack ($\alpha = 0°$), the LEVs begin to change their location with TEVs. The LEVs are now rotating in CCW direction and extending over the airfoil upper surface, whereas the TEVs are now rotating in the CW direction. During this phase of the motion, it is also observed that the strength of the TEVs is also increased. Also, a rotational stopping vortex (see in Figure 44) at the trailing edge of the airfoil is identified only at the end of the rotational phase. After the stroke reversal, the rotational stopping vortex detaches from the airfoil and sheds to the flow.

- Regions 3 and 4 are merely the mirror regions of the 1<sup>st</sup> and 2<sup>nd</sup> regions. Hence similar vortex formation and interaction mechanisms are observed in these regions.
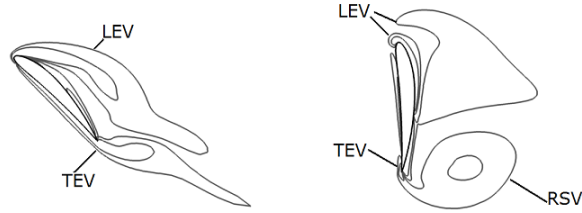


Figure 44. Schematic representations of vortex regions shown with the airfoil

(Ref. [13])

Before the evolution of experimental results, it should be necessary to explain the vorticity. The vorticity of the flow is based on the circulation of the flow along a closed path by the Stokes equation (Ref. [39]). In 2-D flow the vorticity is always perpendicular to the plane of flow. The vorticity ($\omega, [1/s]$) can be expressed as:

$$\vec{\omega} = \nabla \times \vec{v} = \left(\frac{\partial}{\partial x}, \frac{\partial}{\partial y}, \frac{\partial}{\partial z}\right) \times \left(v_x, v_y, 0\right) = \left(\frac{\partial v_y}{\partial x} - \frac{\partial v_x}{\partial y}\right) \vec{z} \qquad \text{(Eqn. 4.1.)}$$

Where $\nabla$ is the del operator, $\vec{v}$ is the velocity field of the flow.

In 3-D flow, the vorticity of the flow is defined in Cartesian coordinates as:

$$\vec{\omega} = \nabla \times \vec{v} = \left(\frac{\partial}{\partial x}, \frac{\partial}{\partial y}, \frac{\partial}{\partial z}\right) \times \left(v_x, v_y, v_z\right) \qquad \text{(Eqn. 4.2.)}$$

$$= \left(\frac{\partial v_z}{\partial y} - \frac{\partial v_y}{\partial z}, \frac{\partial v_x}{\partial z} - \frac{\partial v_z}{\partial x}, \frac{\partial v_y}{\partial x} - \frac{\partial v_x}{\partial y}\right)$$

It has to be noticed in the following sections, that the experimental results presented in the figures are given in perspective views such that a much better and clear picture of the vortex formations around the wing could evidently be observed.

## 4.1. Effects of Vertical Amplitude of Motion

In order to observe the effect of the vertical amplitude of the motion, the experiments were conducted with two different amplitude values (B=c and B=2c, where B is given in Eqn 1.6 and c is the chord of the airfoil) for different initial angle of attacks of α=30°, α=45°and α=60° and Re=1000. However, only the case for the initial angle attack of 45° with two different amplitude values are presented in the current study for brevity.

In order to evaluate the effect of amplitude on the results evidently, only the images captured from the mid-span location are compared. The instantaneous vortex formation along spanwise direction for both vertical amplitudes is given in Appendix.

To evaluate the effect of the vertical amplitude, the aerodynamic mechanisms for the generation of lift should be investigated. Two main aerodynamic mechanisms play an important role on the generation of lift; "Delayed stall" and "Kramer effect". The name of delayed stall stems from the separation of the LEV from the wing surface. The phenomenon "delayed stall" is also called as the separation of the LEVs from the wing surface or the "dynamic stall" of vortices. The second one is the circulation, known as the "Kramer effect". The latter phenomenon is observed on the condition that both the rotational and the translational motions appear at the same time. The Kramer effect is first described by Kramer (Ref. [11]) on the condition that the lift coefficients are obtained above the steady-stall value during stroke reversal. Both aerodynamic mechanisms are explained as follows.

When the wing model passes at point 1 with an initial angle of attack of 45°, a LEV and a TEV pair is generated. As the wing continues its motion, LEVs grows near leading edge. After a certain distance, a new vortex near the trailing edge is generated to keep the total fluid momentum constant. Since the new produced TEVs rotates in the opposite direction compared to LEVs, the TEVs decreases the aerodynamic normal force generation. However, the generated LEVs keep the enhancement of force production until a certain distance where the LEVs detach from leading edge and shed to the flow. In such cases, a reduction of lift occurs, which can lead to "stall". However, prior to the stall, a new LEV is observed around

leading edge. Within this point, this is termed as "delayed stall". Up to now, the explained process periodically repeats with the vortex evolution around wing and shedding into the flow.

As for Kramer effect, this is observed at the end of every stroke (at supination and pronation). From the explanation of Sane (Ref. [10]), the Kramer effect is observed as follows. When the wing rotates along a spanwise axis with translational motion, Kutta condition is deviated. This leads to the stagnation region to move away from the trailing edge. To re-establish the Kutta condition, a new circulation must be generated around the wing to counteract the effects of rotation (see in Figure 45 c). However, the re-establishment of Kutta condition is required a specified time interval due to rapid rotation. In this time interval, the flow tends to resist the shear stresses due to viscosity effects in the flow. In order to re-establish the Kutta condition at the trailing edge, a new additional circulation in the flow is generated to counteract the effect of the rotational motion. Thus, the generation of the ratio of extra circulation to the angular velocity of rotation continues until smooth, tangential flow is obtained. Depending on the direction of rotation, this extra circulation causes rotational forces that either add to or subtract from the net force.
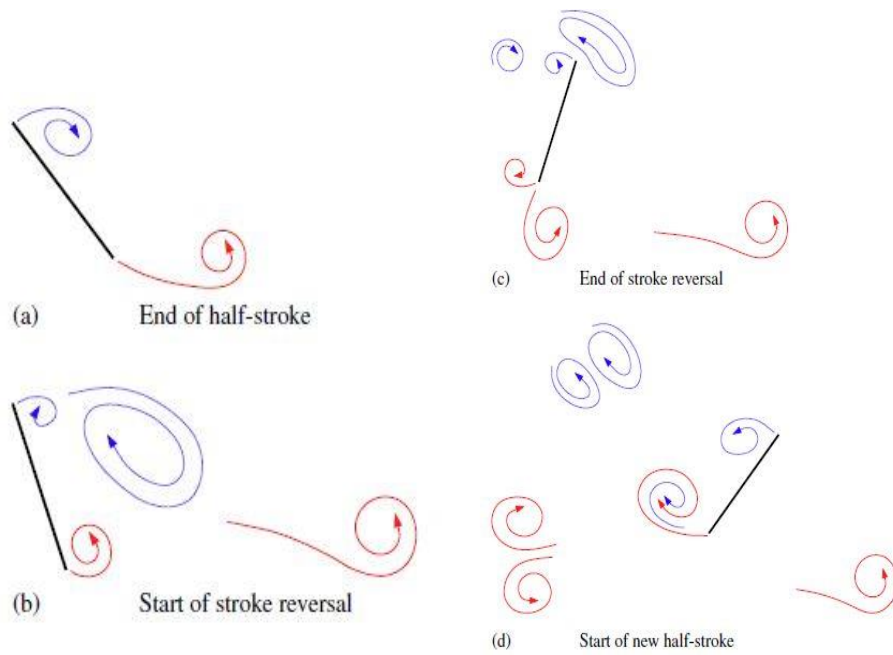
Figure 45. Schematic illustration of Kramer Effect (Ref. [40])

During the experiments obtained examples for Kramer effect are indicated in Figure 46 as instantaneous vorticity contours of wing during the 7th period for all initial angle of attacks at B=2c,and Re=1000.

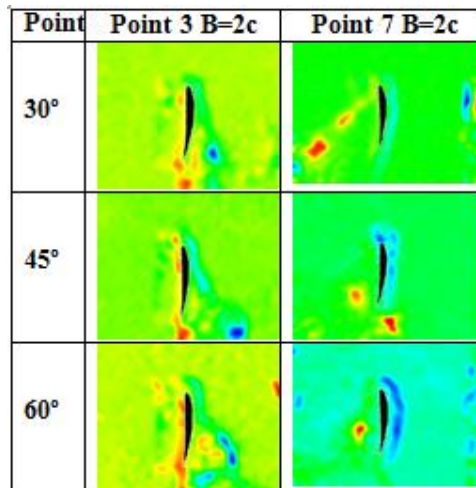| Point | Point 3 B=2c | Point 7 B=2c |
|-------|--------------|--------------|
| 30° | | |
| 45° | | |
| 60° | | |

Figure 46. Instantaneous vorticity contours (1/s) of wing during the 7th period for all initial angle of attacks at B=2c and Re=1000.

As shown in Figure 46 for point 1, the graphs of vorticity contours show that the generated LEVs and TEVs at initial angle of attack of 45° for B=c are substantially larger than the case for α=45° and B=2c. However, as the motion progresses down to point 2, the magnitude of produced counter-rotating vortices are more for the case of B=2c in spite of less attachment of the LEVs and TEVs in the same case.

As continuing the motion at point 2, it is seen that the growth rate of magnitude of LEVs are higher for the case of B=2c rather than B=c. On the other hand, the magnitude of TEVs significantly increases for the case of B=2c from 2.982 (1/s) to 4.420 (1/s), whereas the magnitude of TEVs decrease with the same rate to 3.998 (1/s).

It should be noted that the larger vertical amplitude of the motion is a chord length longer than the smaller one. Because of this, the vortex formations during the figure-of-eight motion show the differences between two different vertical amplitudes. Hence, the main difference between B=c and B=2c comes from the path of figure-of-eight motion such that the translation the vorticities to the flow is more in the case for B=2c due to higher angle of attack.

When the wing reaches to points 3 and 7 along its trajectory during the figure-of-eight motion, the delayed stall and Kramer effect play a significant role on the vortex formations. The new additional circulation at trailing edge are more apparently observed for larger amplitude (i.e. B=2c), rather than for small amplitude case (ie. B= c). Also, the stopping vorticity from the separated LEVs is distinctly identified in the case of B=2c at point 3. Thus, due to less attachment of the LEVs at point 3, the produced additional circulation for the case of B=2c can not counteract the effect of the rotational motion as much as for the case of B=c. This results in the reduction of the magnitude of counter-rotating vortices for the case of B=2c. For instance, the magnitude of TEVs for B=2c at point 7 is 6.671 (1/s), while the magnitude of TEVs for B=c is 3.728 (1/s) for the same point.
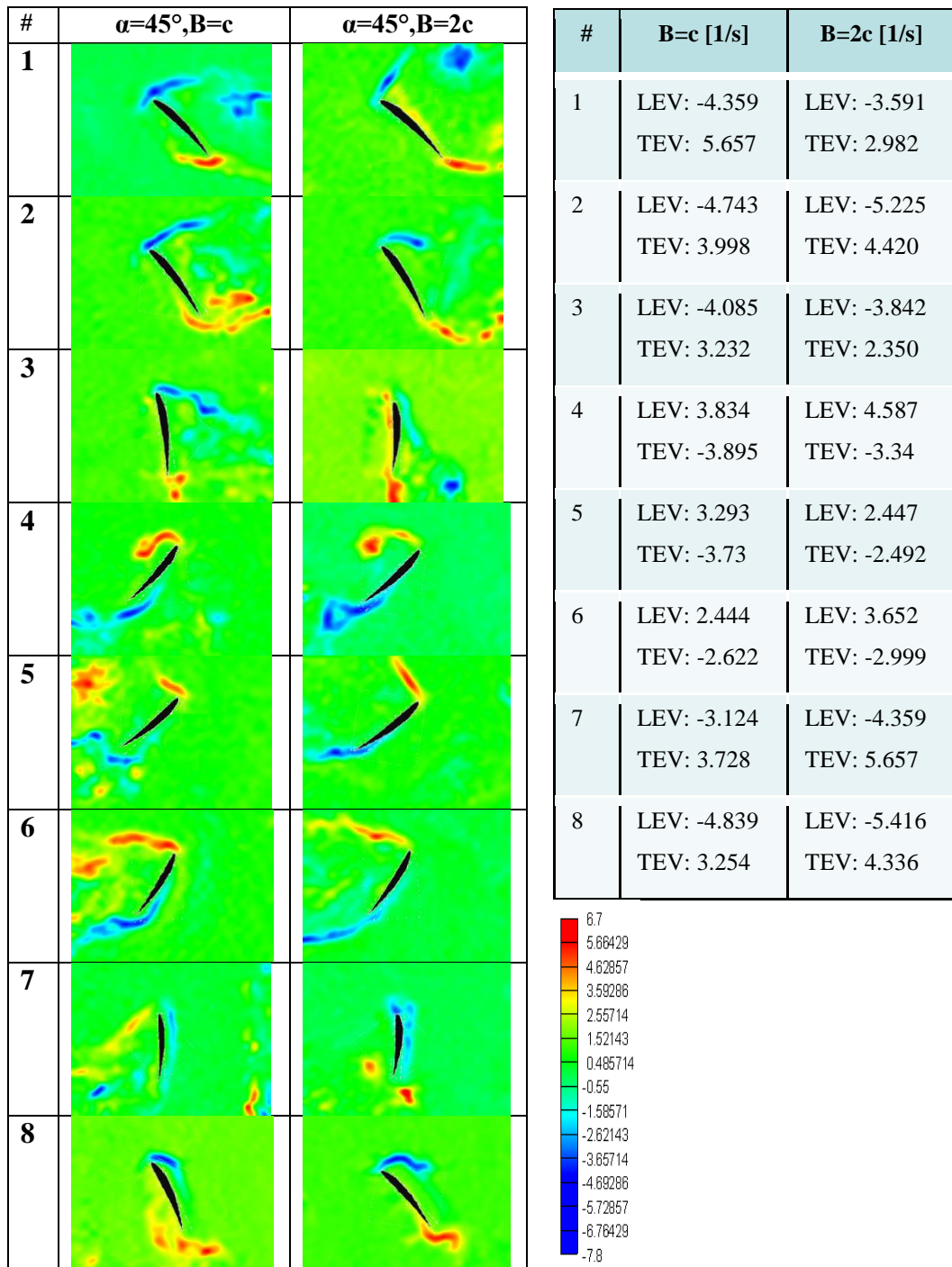
| # | α=45°,B=c | α=45°,B=2c |
|---|-----------|------------|
| 1 | | |
| 2 | | |
| 3 | | |
| 4 | | |
| 5 | | |
| 6 | | |
| 7 | | |
| 8 | | |

| # | B=c [1/s] | B=2c [1/s] |
|---|-----------|------------|
| 1 | LEV: -4.359<br>TEV: 5.657 | LEV: -3.591<br>TEV: 2.982 |
| 2 | LEV: -4.743<br>TEV: 3.998 | LEV: -5.225<br>TEV: 4.420 |
| 3 | LEV: -4.085<br>TEV: 3.232 | LEV: -3.842<br>TEV: 2.350 |
| 4 | LEV: 3.834<br>TEV: -3.895 | LEV: 4.587<br>TEV: -3.34 |
| 5 | LEV: 3.293<br>TEV: -3.73 | LEV: 2.447<br>TEV: -2.492 |
| 6 | LEV: 2.444<br>TEV: -2.622 | LEV: 3.652<br>TEV: -2.999 |
| 7 | LEV: -3.124<br>TEV: 3.728 | LEV: -4.359<br>TEV: 5.657 |
| 8 | LEV: -4.839<br>TEV: 3.254 | LEV: -5.416<br>TEV: 4.336 |

6.7
5.66429
4.62857
3.59286
2.55714
1.52143
0.485714
-0.55
-1.58571
-2.62143
-3.65714
-4.69286
-5.72857
-6.76429
-7.8



Figure 47. Instantaneous vorticity contours (1/s) of wing with its magnitudes during the 7th period for α=45, B=c, B=2c and Re=1000

The main difference between the points 3 and 7 is that the magnitude of LEVs at point 3 for the case of B=c decreases from 4.085 (1/s) to 3.842 (1/s) with increasing vertical amplitude. Nevertheless, the magnitude of LEVs at point 7 for the case of B=2c increases from 3.124 (1/s) to 3.689 (1/s). The reason comes from that the strength of vortices is increased by the attachment of LEVs to the wing.

Although the size of produced new TEVs increases quite rapidly at higher vertical amplitude (i.e B=2c), the generated TEVs are less affected by the remaining vortices from the previous stroke. This is especially observed at point 7.

After passing the point 3, the LEVs and the TEVs start to change their location around the wing. At this point, the LEVs and TEVs substitute their location from the upper surface to the lower surface of the wing and also change their rotational direction. The direction of LEVs is in the CCW direction, whereas the direction of TEVs is in the CW direction. For two amplitudes, the produced LEVs at point 3 tend to separate from leading edge of wing, as the new LEVs are generated.

As seen from point 4 in Figure 47, as the angle of attack increases throughout the motion trajectory, the strength of the LEVs continues to increase and is followed by an eventual detachment of these vortices from the leading edge of the wing. Thus, the magnitude of LEVs for the case of B=c changes from 3.834 (1/s) to 4.587 (1/s) for the case of B=2c.

On the other hand, while the successive TEVs are more visible and persistent near the trailing edge for low amplitude case (i.e. B=c case), they tend to move towards leading edge of the wing from its lower surface for the larger amplitude case (i.e. B=2c).

As the wing is passing through point 5, the generated TEVs are more detached due to increased vertical amplitude of the motion, which cause to decrease the strength of TEVs. Similarly, the separated LEVs dissipate to the flow at the higher vertical amplitudes, which causes to lower magnitudes of LEVs. The effect of the vertical amplitude on the counter-rotating vortices is such that magnitude of counter-rotating vortices for B=2c is lower.

As the wing continues its motion at point 6, it is possible to say that a larger interaction between LEVs and TEVs is seen at lower vertical amplitude of motion.

66

As a result of this, the interaction decreases the magnitude of LEVs and TEVs. For instances, the magnitude of LEVs decreases from 2.999 (1/s) to 2.622 (1/s) during the lower vertical amplitude of the motion (i.e. B=c).

The last point to complete the trajectory of the figure-of-eight motion is point 8. In this point, newly generated LEVs turn in the CW direction, while the TEVs rotate in the CCW direction. Although this location is a mirror position of point 4, the strength and the magnitude of the counter-rotating vortex couples at point 8 is higher than at point 4 due to non-symmetrical airfoil shape of wing. The magnitude of generated counter-rotating vortices increases with higher vertical amplitude of motion at point 8.

Generally, it could be infirm from the results for the case of B=2c and for α= 45° that the generated LEVs and TEVs for higher vertical amplitude of motion are substantially larger. There are two reasons as follows. The former is that the interaction between the counter-rotating vortices is less for the case of B=2c, which leads to less combination of the LEVs and TEVs. The latter is that the wing moves with a higher angle of attack. So, more massive vortices are obtained for the case of B=2c.

It should be stated that the maximum magnitudes of LEVs and TEVs are observed at point 8 (respectively 5.416 (1/s), 4.336 (1/s)) for B=2c, whereas the maximum magnitudes of counter-rotating vortices for B=c is seen at point 1 (respectively 4.359 (1/s), 5.657(1/s)). As general remarks, the magnitude of counter-rotating vortices for both amplitudes is higher during the downstroke of figure-of-eight motion.

## 4.2. Effects of Initial Angle of Attack

This section includes effects of the initial angle of attack with three different angles for both amplitudes during figure-of-eight motion. In order to evaluate the results for all angle of attacks, the images captured from mid-span location are compared. The instantaneous vortex formation along spanwise direction for all initial angle of attacks is given in Appendix.

As seen in Figure 48, at the beginning of the motion CW rotating LEVs and CCW rotating TEVs detaches with increasing angle of attacks. However, higher angle of attack causes production of massive coupling vortices. For instance, the magnitude of

LEVs changes from 4.750 (1/s) to 5.258 (1/s) (see in Table 6), as the initial angle of attack increases. So, low pressure area over the suction side of airfoil leads to the generation of lift.

During translational motion from point 1 to point 2, the size of LEVs decreases with increasing initial angle of attack, since the LEVs can not reattach around leading edge due to separation. So, the magnitude of LEVs decreases from 5.220 (1/s) to 4.389 (1/s). On the other hand, the size of TEVs grows up to initial angle of attack of 60°, then the detached TEVs at α= 60 ° are extensively observed around the trailing edge. As seen below, the magnitude of TEVs decline from 5.182 (1/s) to 3.998 (1/s) until initial angle of attack of 60°. After that, the magnitude of TEVs rises to 4.197 (1/s).

At the stroke reversal, the rotational phase is effective on the formation of vortex structure. Since the detachment of LEVs near the airfoil is more with increasing angle of attack, the magnitude of LEVs rises from 4.019 (1/s) to 4.58 (1/s). However, for all angle of attacks, a magnitude of TEVs (approx. 3.4 (1/s)) is generally same, since generated additional circulations around trailing edge counteract the effects of the rotation. Besides that, the diffusion of TEVs towards LEVs occurs at higher angle of attacks. After the wing model completes its rotation, magnitude of TEVs is higher than the magnitude of LEVs on the condition that the initial angle of attack increases up to 60°. For instances, at α=30° the magnitudes of TEVs and LEVs are respectively 3.149 (1/s), 2.929 (1/s). At higher angle of attack, the produced TEVs move up to leading edge, which causes to more massive LEVs than TEVs ( i.e. the magnitudes are respectively 4.935 (1/s), 3.536(1/s)). Also, at α=45°, the generated successive TEV pairs are apparently seen around the trailing edges of the wing.

When the wing model returns to the initial position at point 5, the generated LEVs are extended at higher initial angle of attacks. However, the separated LEVs try to reattach to lower surface of the wing. The higher magnitude of LEVs (3.293(1/s)) are observed at α=45°. Besides that, the shedding TEVs at higher angle of attack moves towards to LEVs, which makes the LEVs be more massive around leading edge of wing. As a result of this, the magnitude of TEVs increases from 2.471 (1/s) to 4.238 (1/s).
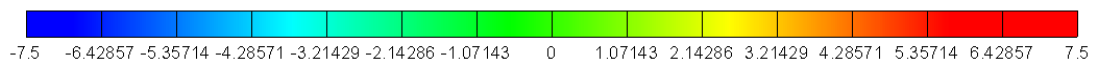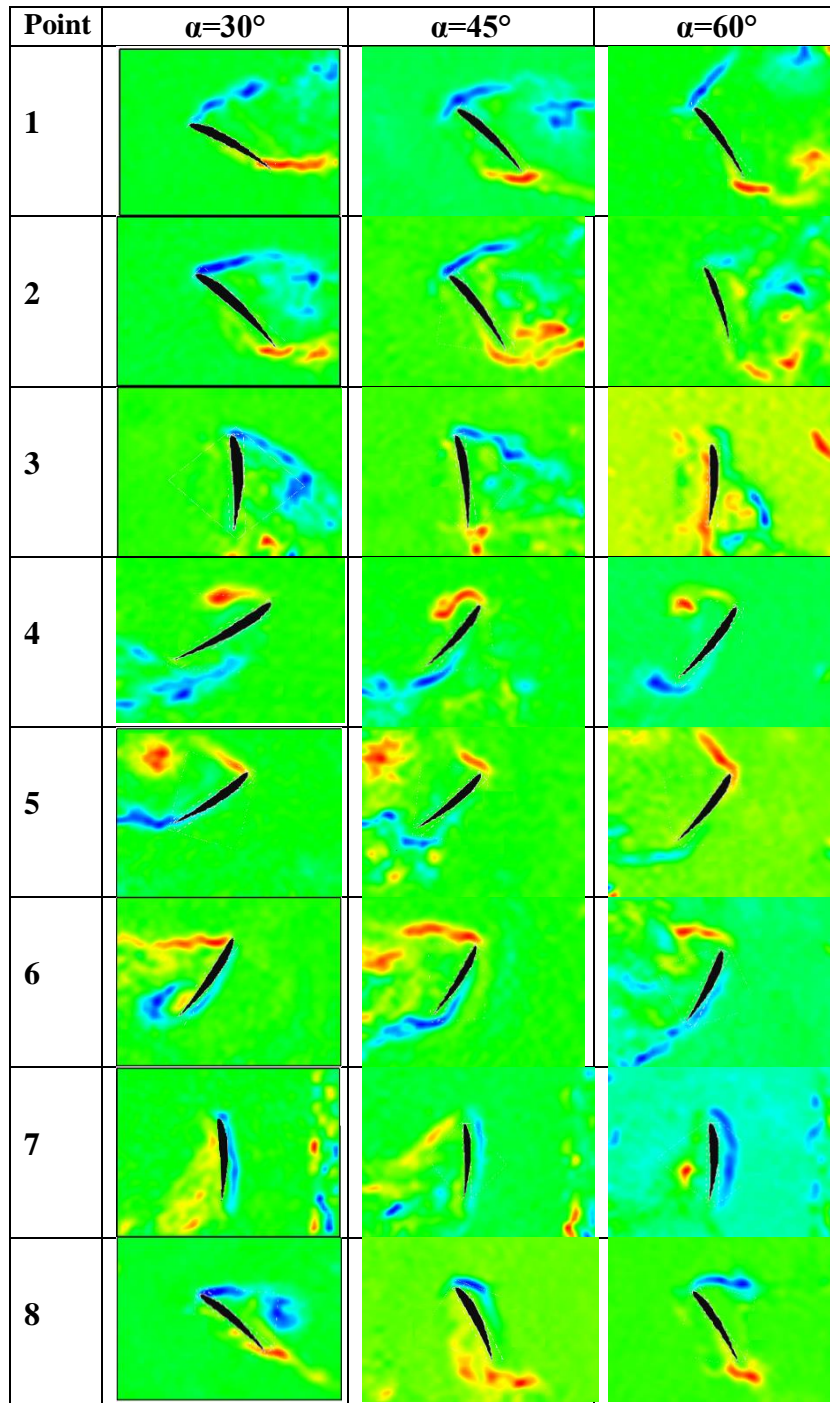
Figure 48. Instantaneous vorticity contours (1/s) of wing during the 7th period for all initial angle of attacks with B=c and Re=1000

Table 6. Magnitudes of instantaneous vorticity contours (1/s) of wing during the 7th period for all initial angle of attacks with B=c and Re=1000

| Point | α= 30° | α= 45° | α= 60° |
|---|---|---|---|
| 1 | LEV: -4.756<br>TEV: 5.362 | LEV: -4.359<br>TEV: 5.657 | LEV: -5.258<br>TEV: 5.542 |
| 2 | LEV: -5.220<br>TEV: 5.182 | LEV: -4.743<br>TEV: 3.998 | LEV: -4.389<br>TEV: 4.197 |
| 3 | LEV: -4.019<br>TEV: 3.449 | LEV: -4.085<br>TEV: 3.232 | LEV: -4.580<br>TEV: 3.440 |
| 4 | LEV: 2.929<br>TEV: -3.149 | LEV: 3.834<br>TEV: -3.895 | LEV: 4.935<br>TEV: -3.536 |
| 5 | LEV: 2.566<br>TEV: -2.471 | LEV: 3.293<br>TEV: -3.739 | LEV: 2.847<br>TEV: -4.238 |
| 6 | LEV: 2.165<br>TEV: -2.441 | LEV: 2.444<br>TEV: -2.622 | LEV: 3.433<br>TEV: -4.139 |
| 7 | LEV: -2.755<br>TEV: 2.856 | LEV: -3.125<br>TEV: 3.728 | LEV: -4.498<br>TEV: 6.213 |
| 8 | LEV: -5.548<br>TEV: 5.116 | LEV: -4.839<br>TEV: 3.254 | LEV: -6.233<br>TEV: 5.356 |

As the wing model continues the motion to point 6 (see in Figure 48), the produced LEVs attach to the pressure surface of wing and tend to interact the TEVs at α=30°. This situation causes the separation of TEVs near the trailing edge due to shedding LEVs. Although at α=60° the counter-rotating vortices detaches more than α=45°, the higher angle of attacks lead to extension of the LEVs by diffusing towards

trailing edge. Especially for α=60°, this case could be distinctly observed. Thus, among all initial angle of attacks, the maximum magnitudes of LEVs and TEVs are seen at α=60°. As the angle of attack increases, the magnitudes of LEVs and TEVs are respectively as follows: 2.165 (1/s), 2.441(1/s); 2.444(1/s), 2.622(1/s); 3.433 (1/s), 4.139(1/s) ( see in Table 6).

During stroke reversal at point 7, the circulation of vortices plays an important role in generation of lift. As indicated in Figure 48, the generated counter-rotating vortices dissipate to the flow during the sudden changes in the wing location. At lower angle of attack a couple counter-rotating vortices are closer to each other due to the attachment of them to the wing. Especially at this point, the remaining vertical counter-rotating vortices from previous stroke are observed. For instance, these remaining vortices are less seen in higher initial angle of attacks due to the lack of interaction of these vortices. However, regardless of the increment of angle of attack, the TEVs are more attached to the wing model on the upper surface, whereas at higher initial angle of attack the detachment of LEVs is more than the TEVs. This condition is extensively seen at α=60°. As a result of this, higher magnitudes of LEVs and TEVs are respectively observed 6.123 (1/s), 4.498(1/s) at α=60°.

After the end of rotation at point 8, the attached TEVs at point 7 shed to the flow, resulting in a new production of TEVs. At higher initial of angle of attack, the LEVs separate from the leading edge of the wing and then dissipate to the flow. On the other hand, since the separated LEVs increase their magnitudes, the magnitudes of LEVs for α=30° and α=60° are respectively 5.548 (1/s), 6.233 (1/s). At α=45° the magnitude of LEV is lower than the other two angles. Similarly, since the size of new generated TEVs are larger and they are more extended to the flow, the magnitudes of TEVs for α=30° and α=60° are respectively 5.116 (1/s), 5.356 (1/s). At α=45° the magnitude of TEVs is lower than the other two angles.

It should be noted that the higher magnitudes of LEVs and TEVs are generally observed at the initial angle of attack of 60°. During the figure-of-eight motion, the maximum magnitudes of LEVs and TEVs are respectively identified 6.233 (1/s) and 5.356 (1/s) at point 8. As general remarks, the magnitude of counter-rotating vortices for all angle of attacks is higher during the downstroke of figure-of-eight motion.

71

## 4.3. Investigation of Velocity Magnitude along Spanwise Direction ($\overrightarrow{W}$)

In this section, the behavior of the span-wise component of velocity around LEVs and TEVs is investigated using SPIV technique at three different spanwise locations. As previous sections, data is presented for three initial angle of attacks and two distinct vertical amplitudes. Figure 49 presents the distribution of instantaneous velocity component along the spanwise direction of the wing at three different spanwise locations for points 1 and 2 of figure-of-eight motion during the 7th period for three initial angle of attacks of α=30°, α=45° and α=60° with amplitude of B=c. The corresponding Reynolds number is 1000. Figure 50 shows the instantaneous velocity component along the spanwise direction for points 3 and 4 for the same conditions.

As it is obvious from the Figure 49, the motion in spanwise direction is decreased by increasing the initial angle of attack for points 1 and 2. And also more motion in spanwise direction is depicted in the wing tip area. In Figure 50 while the wing model approaches the 3$^{rd}$ point of the figure-of-eight motion, it seems that there are quite similar spanwise motion distributions for all three initial angle of attacks cases as the corresponding angle of attack for the wing at point 3 is zero for all three cases. Figure 50 indicates that the motion in spanwise direction is increased towards wing tip area by increasing the initial angle of attack for points 4.

72

| # | 1 (B=c) | 2(B=c) |
|---|---------|--------|
| 30° | | |
| 45° | | |
| 60° | | |

W: -0.1760 -0.1451 -0.1141 -0.0832 -0.0523 -0.0214 0.0096 0.0405 0.0714 0.1024 0.1333 0.1642 0.1951 0.2261 0.2570
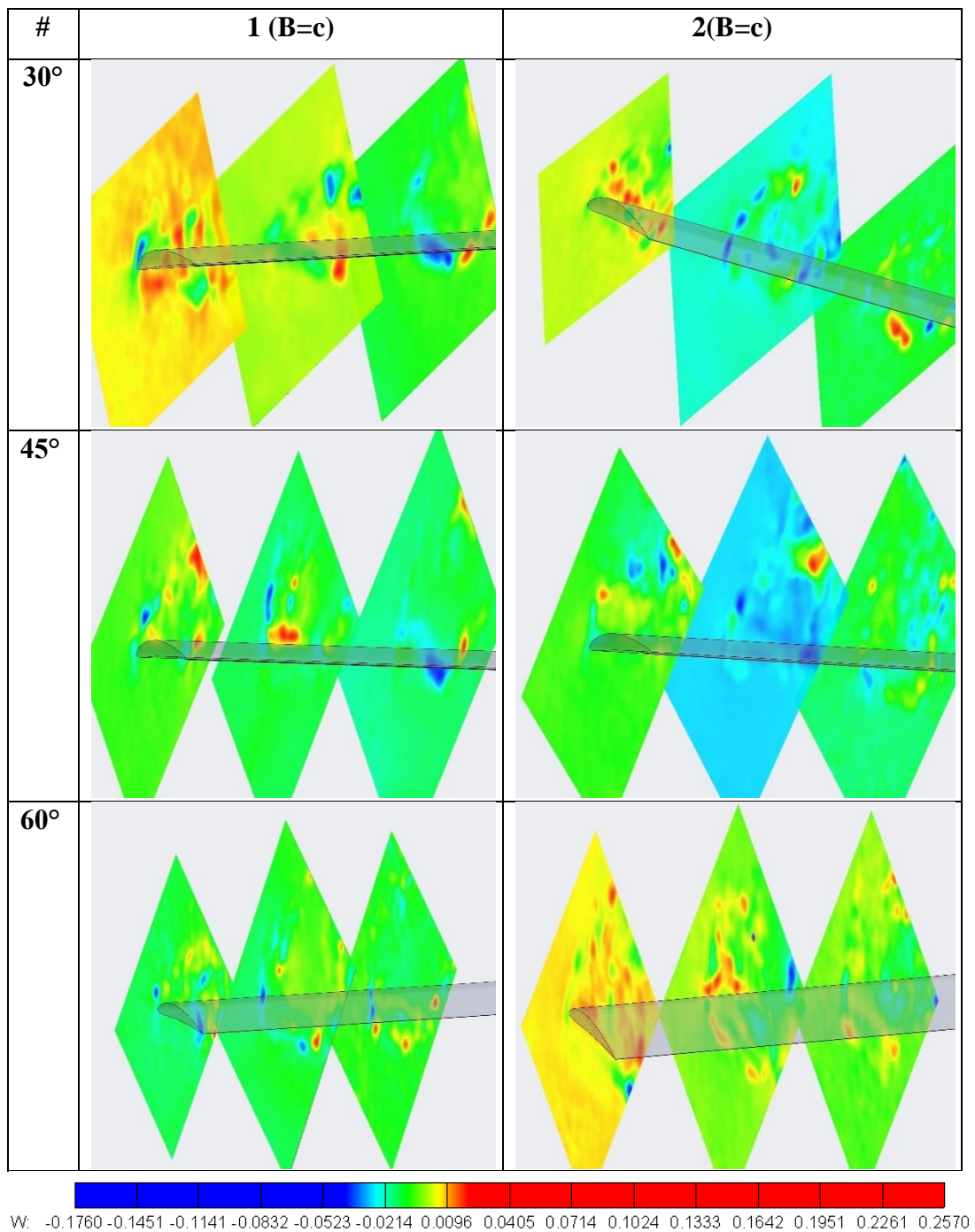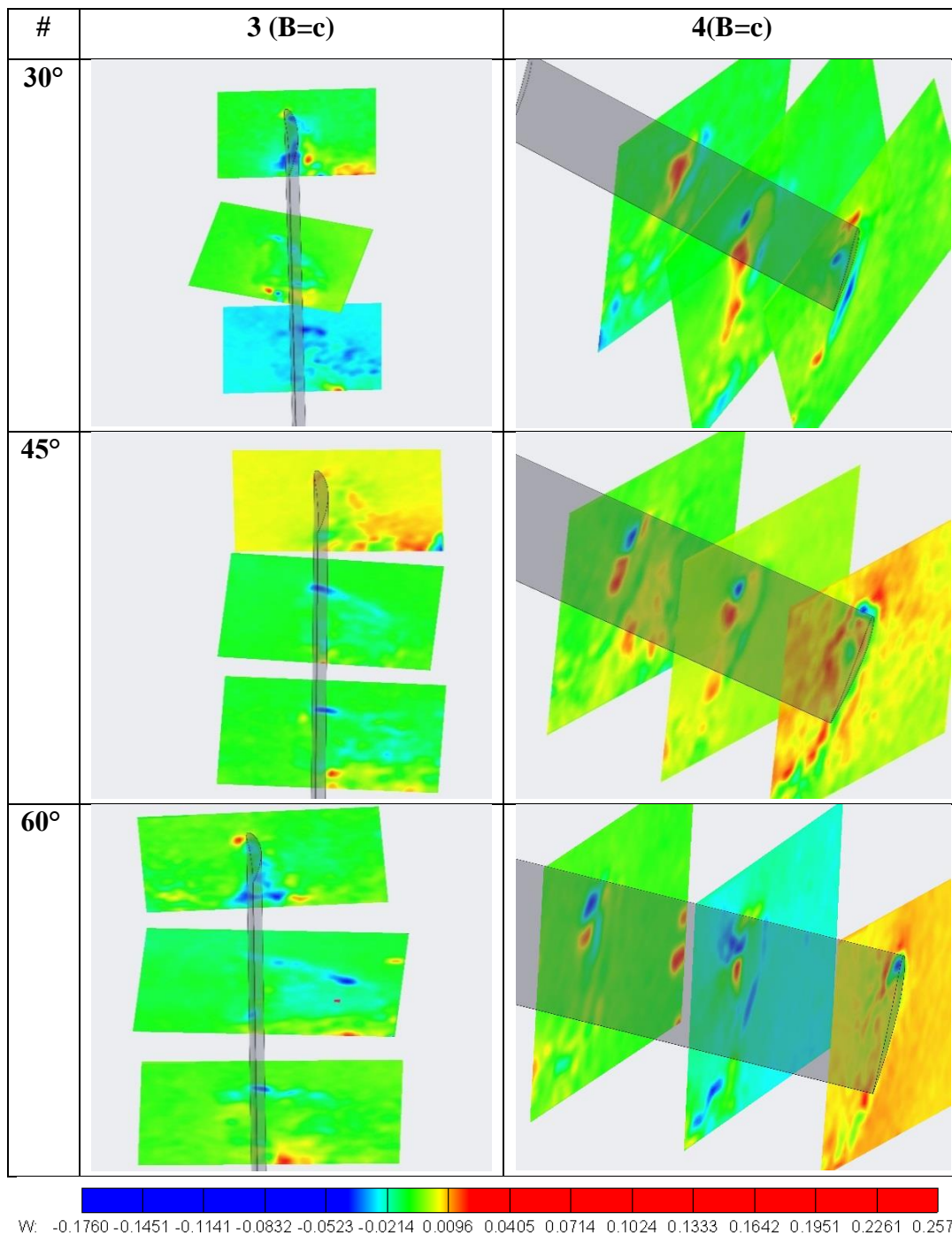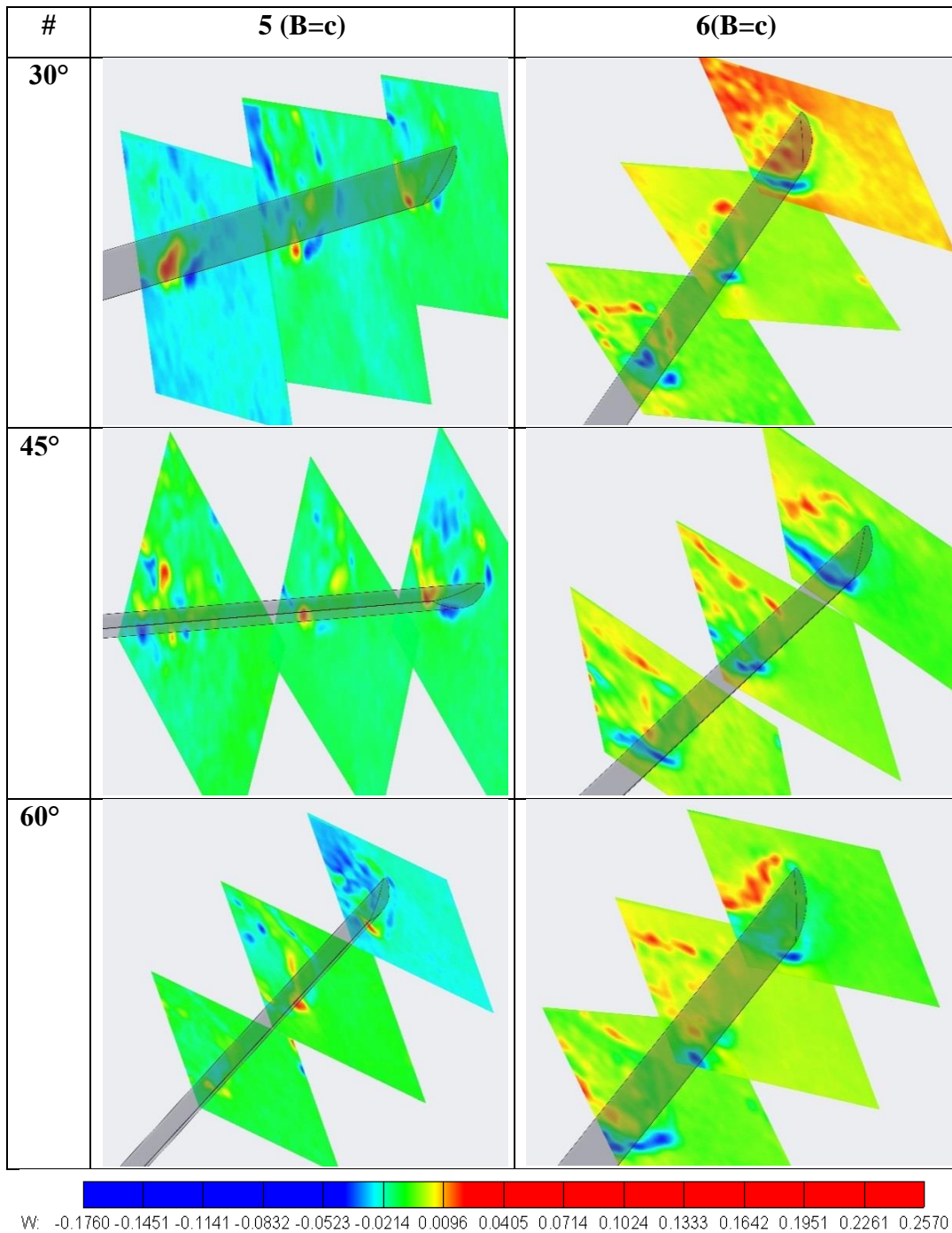
Figure 49. The distribution of instantaneous velocity along the spanwise direction (W) of the model wing at three different spanwise locations for point 1 and 2 during the 7th period for α=30°, α=45°, α=60°, B=c and Re=1000.

| # | 3 (B=c) | 4(B=c) |
|---|---------|--------|
| 30° | | |
| 45° | | |
| 60° | | |

W:  -0.1760 -0.1451 -0.1141 -0.0832 -0.0523 -0.0214 0.0096 0.0405 0.0714 0.1024 0.1333 0.1642 0.1951 0.2261 0.2570
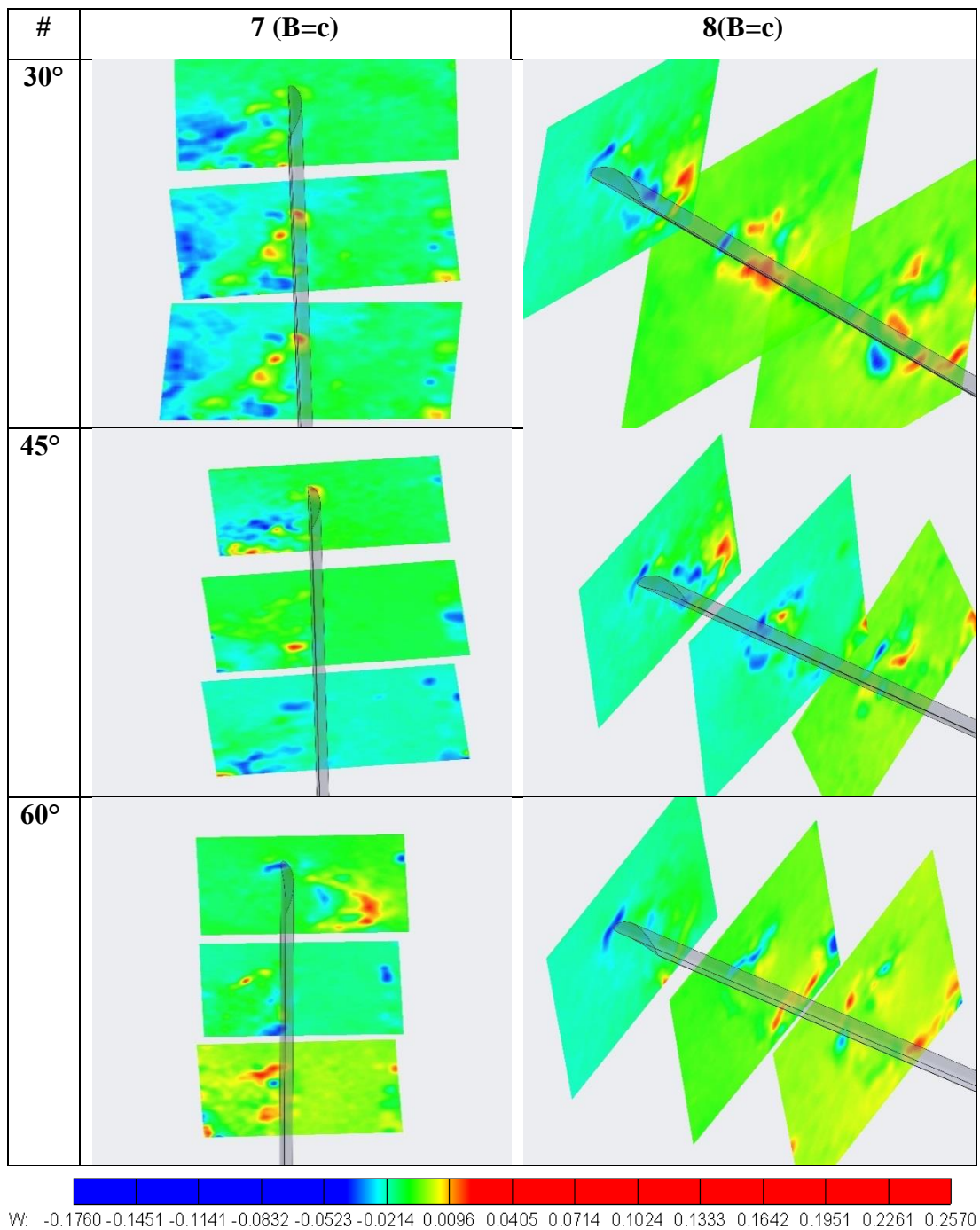
Figure 50. The distribution of instantaneous velocity along the spanwise direction (W) of the model wing at three different spanwise locations for point 3 and 4 during the 7th period for α=30°, α=45°, α=60°, B=c and Re=1000.

| # | 5 (B=c) | 6(B=c) |
|---|---------|--------|
| 30° | | |
| 45° | | |
| 60° | | |

W:  -0.1760 -0.1451 -0.1141 -0.0832 -0.0523 -0.0214 0.0096 0.0405 0.0714 0.1024 0.1333 0.1642 0.1951 0.2261 0.2570
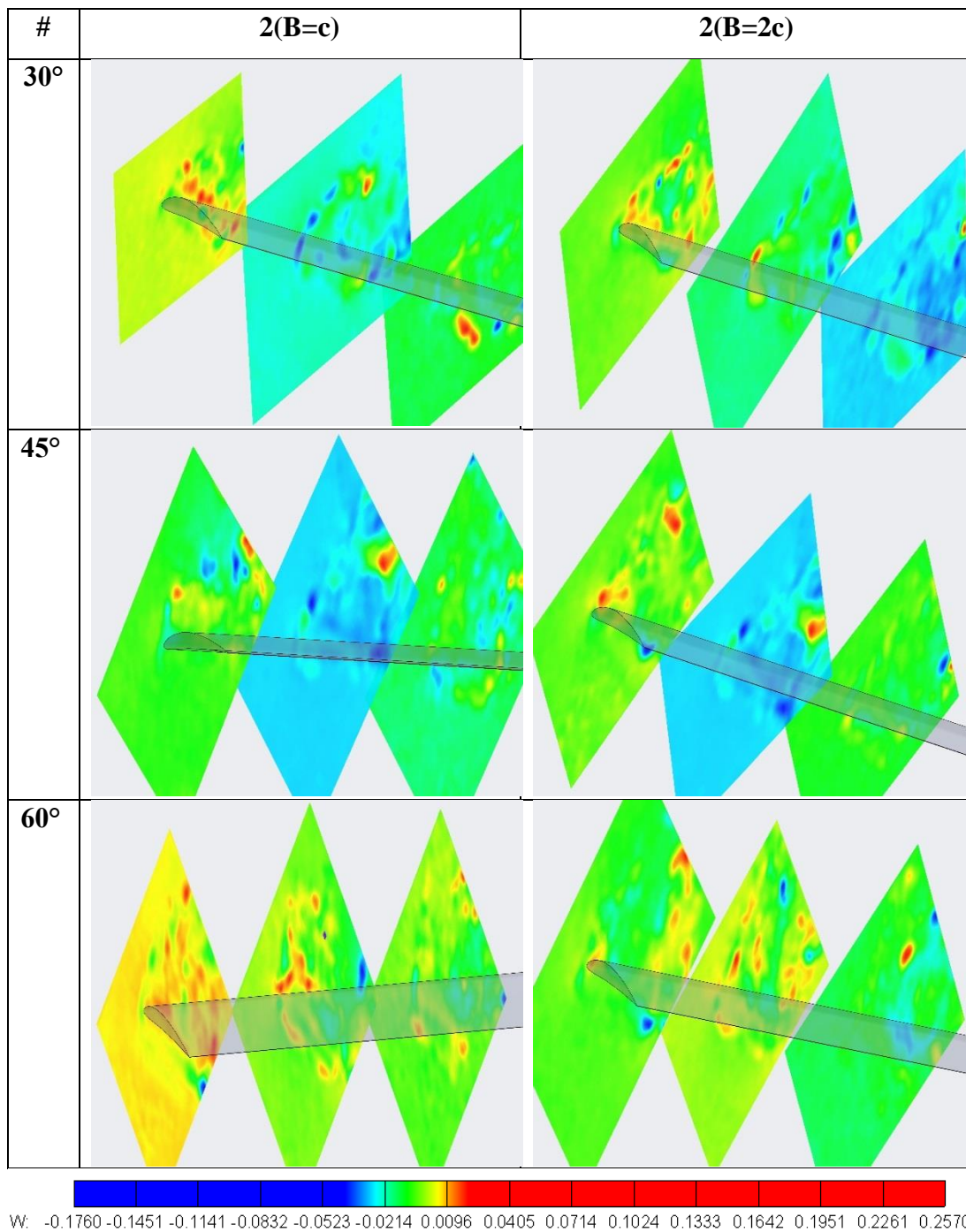
Figure 51. The distribution of instantaneous velocity along the spanwise direction (W) of the model wing at three different spanwise locations for point 5 and 6 during the 7th period for α=30°, α=45°, α=60°, B=c and Re=1000.

Figure 51 presents the distribution of instantaneous velocity component along the spanwise direction of the wing at three different spanwise locations for points 5 and 6 of the figure-of-eight motion during the 7th period for three initial angle of attacks of α=30°, α=45° and α=60° with amplitude of B=c. The corresponding Reynolds number is 1000. In point 6 we can see that spanwise motion around wing's leading edge is generally towards wing tip, while around trailing edge location it is generally towards wing root. The other interesting point is that during down stroke motion the spanwise motion is depicted to occur in suction side of the wing and respectively in up stroke motion the spanwise velocity components are generally seen in pressure side of the wing(obviously it is the same for LEVs and TEVs).

Figure 52 presents the distribution of instantaneous velocity component along the spanwise direction of the wing at three different spanwise locations for points 7 and 8 of the figure-of-eight motion during the 7th period for three initial angle of attacks of α=30°, α=45° and α=60° with amplitude of B=c. The corresponding Reynolds number is 1000. For point 7, similar to point 3 it seems that there are quite identical spanwise motion distributions for all three initial angle of attacks. As the wing reaches point 8, the spanwise velocity distribution is quite similar to what we have seen for point 1. The spanwise velocity is generally decreased by increasing the initial angle of attack.

| # | 7 (B=c) | 8(B=c) |
|---|---------|--------|
| 30° | | |
| 45° | | |
| 60° | | |

W:  -0.1760 -0.1451 -0.1141 -0.0832 -0.0523 -0.0214 0.0096 0.0405 0.0714 0.1024 0.1333 0.1642 0.1951 0.2261 0.2570

Figure 52. The distribution of instantaneous velocity along the spanwise direction (W) of the model wing at three different spanwise locations for point 7 and 8 during the 7th period for α=30°, α=45°, α=60°, B=c and Re=1000.

| # | 2(B=c) | 2(B=2c) |
|---|--------|---------|
| 30° | | |
| 45° | | |
| 60° | | |

W:  -0.1760 -0.1451 -0.1141 -0.0832 -0.0523 -0.0214 0.0096 0.0405 0.0714 0.1024 0.1333 0.1642 0.1951 0.2261 0.2570

Figure 53. The distribution of instantaneous velocity along the spanwise direction (W) of the model wing for B=c (left) and B=2c (right), at three different spanwise locations for point 2 during the 7th period for α=30°, α=45°, α=60° and Re=1000

The effects of vertical amplitude on the velocity component in the spanwise direction are investigated in this section. The spanwise velocity component distributions are shown for B=c and B=2c study cases for point 2 of the figure-of-eight motion in Figure 53. The corresponding Reynolds number is 1000.

As it is shown in Figure 53, for B=2c more motion in spanwise direction is depicted for B=2c case in a wider area above the suction surface of the wing. It can be due to existence of more detached vortices for case B=2c in the upper area of wing suction surface. So it can be generally concluded that by increasing vertical amplitude of motion more spanwise motion is seen around leading and trailing edges of the wing model.

## 4.4. Comparison with Previous Studies:

In this section, the results of present study which are taken at the mid-span location of wing are compared with previous 2-D studies.

Firstly, the experimental results of the instantaneous vorticity contours of wing having NACA 6412 airfoil profile during the 7th period for α=30°, α=45°, α=60° and B=c are compared with the experimental results of the study previously performed by Cekinmez (Ref. [15]) (Comparison tables are given in Figure 54 to Figure 57). After that, current studies exp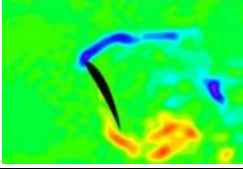erimental results and the numerical results obtained by Cekinmez (Ref. [15]) for the 7th period of flapping motion are compared for two different amplitudes of figure-of-eight motion at α=30° in Figure 58.

Comparing the present experimental results with previous experiments of Cekinmez (Ref. [15]), it can be seen that the formation of the LEVs and the TEVs are similar in both experiments. Even, the vortices remaining from previous stroke are observed for both studies especially at point 7 for α= 30°, α= 45°, α= 60° at B=c and B=2c. It is also seen that (from Figure 54 to Figure 57) these vortices are not interact with the vortices that are formed during the present stroke. On the other hand, since in current study the 3-D flow measurements are performed with single end plate mounted to the wing root, the fluid motion in spanwise direction is not restricted. However, the study of Cekinmez (Ref. [15]) has end plates in both sides of

the wing (tip and root). Thus, the effects of spanwise motions on the vortex structures can be seen well in current study compared to previous one (Cekinmez Ref. [15]).

The difference in the experimental results between the current study and previous study of Cekinmez Ref. [15] is that the vortex formations around both edges of wing are more detached from the wing and extended into the flow in the current study. Compared to the current results, the generated LEVs and TEVs in the previous results are distributed in larger area. As a result of this, the magnitudes of counter-rotating vortices in the present study are higher than the previous one. For instances, for initial angle of attack of 30°, the magnitude range of vorticities changes between the values of -5.548 (1/s) to 5.362 (1/s), whereas this range in the previous study is between – 4.76 (1/s)  to 4.25 (1/s). It can be concluded from above that the effects of three dimensionality leads to more powerful vortices around the wing. In the other words, if the spanwise motion s restricted, less powerful vortices will be formed.

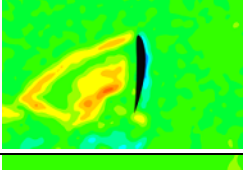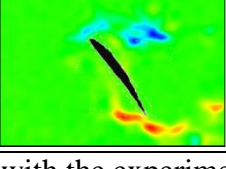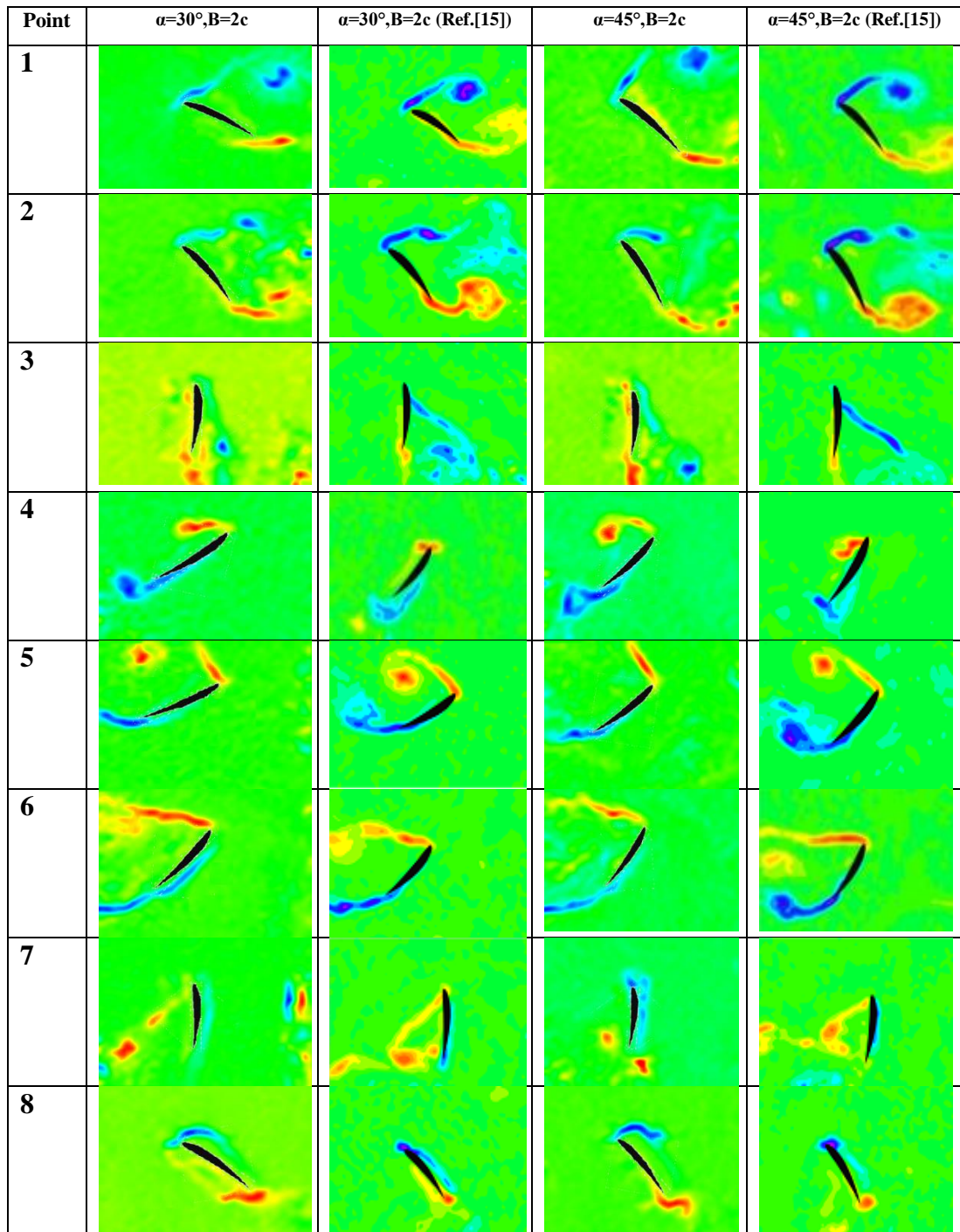| Point | α=30°,B=c | α=30°,B=c (Ref. [15]) | α=45°, B=c | α=45°, B=c (Ref. [15]) |
|-------|-----------|----------------------|------------|------------------------|
| 1 | | | | |
| 2 | | | | |
| 3 | | | | |
| 4 | | | | |
| 5 | | | | |
| 6 | | | | |
| 7 | | | | |
| 8 | | | | |
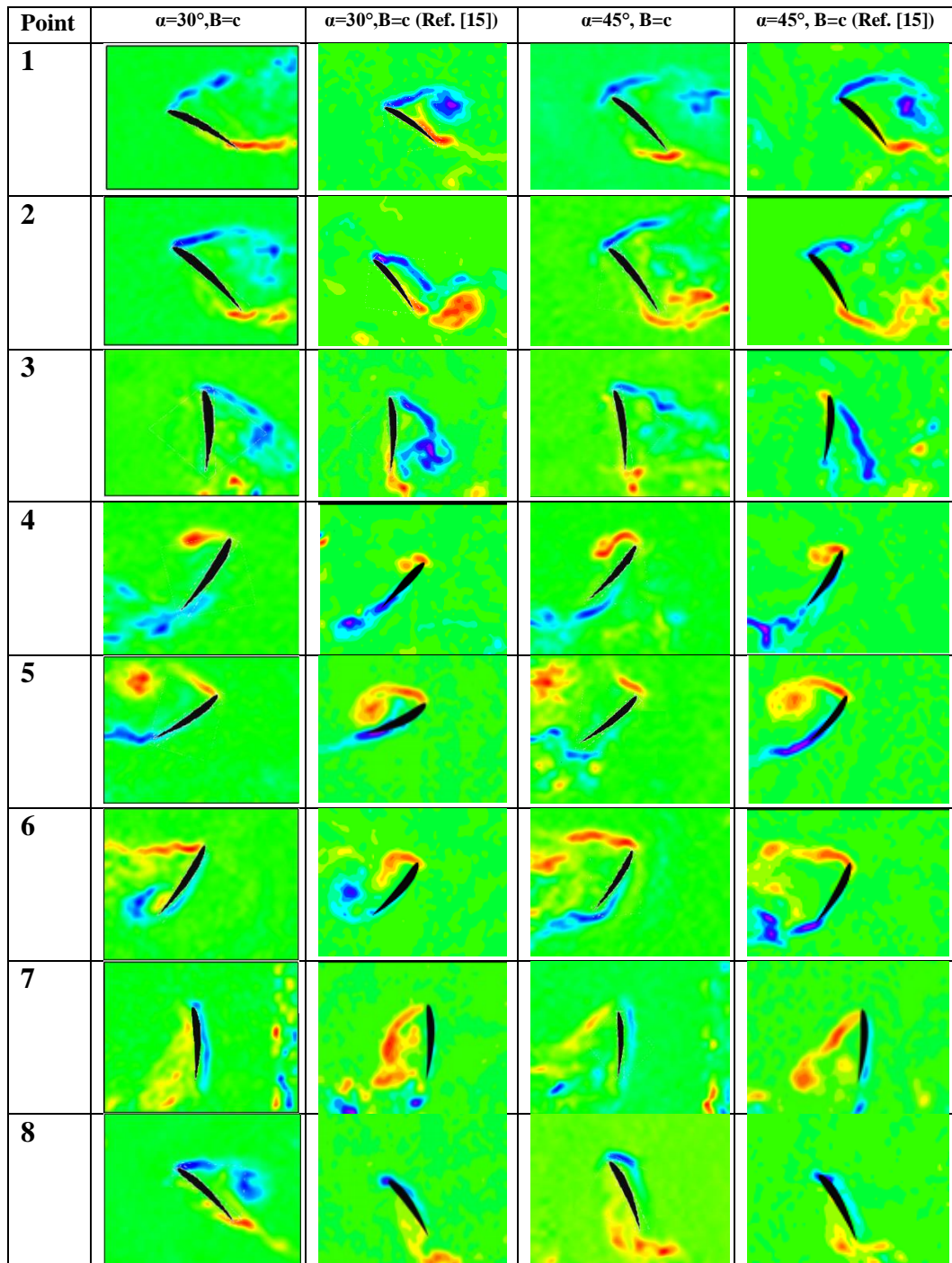
Figure 54. A comparison with the experimental study of Cekinmez (Ref. [15]) as instantaneous vorticity contours of wing during 7th period for α=30°, α=45°, B=c and Re=1000. The 1st and 3rd coloums have the 3-D experimental results of current study, which are captured at the mid-span location.
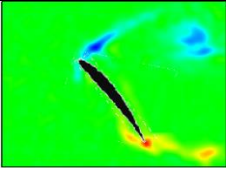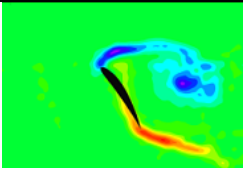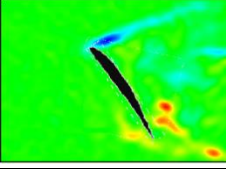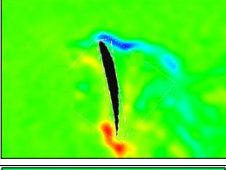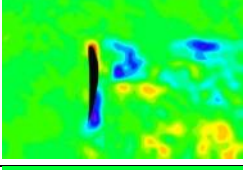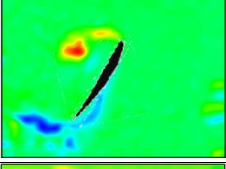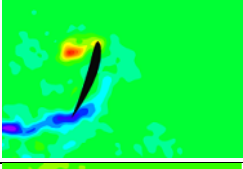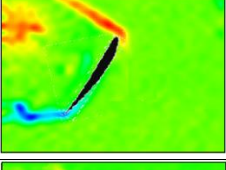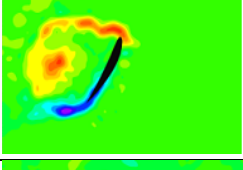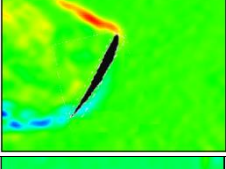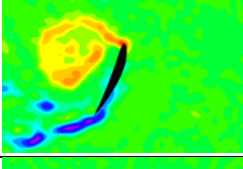
| Point | B=c | B=c (Ref.[15]) |
|-------|-----|----------------|
| 1 | | |
| 2 | | |
| 3 | | |
| 4 | | |
| 5 | | |
| 6 | | |
| 7 | | |
| 8 | | |

Figure 55. A comparison with the experimental study of Cekinmez (Ref. [15]) as instantaneous vorticity contours of wing during 7th period for α=60° and B=c, Re=1000. The 1$^{st}$ coloum has the 3- D experimental results of current study, which are captured at the mid-span location.

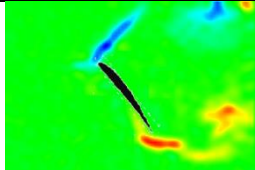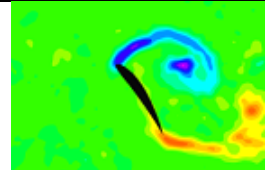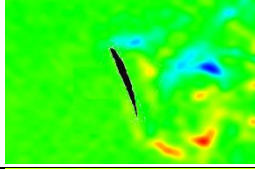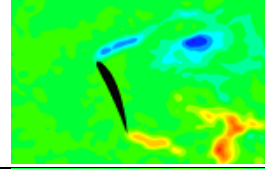| Point | α=30°,B=2c | α=30°,B=2c (Ref.[15]) | α=45°,B=2c | α=45°,B=2c (Ref.[15]) |
|---|---|---|---|---|
| 1 | | | | |
| 2 | | | | |
| 3 | | | | |
| 4 | | | | |
| 5 | | | | |
| 6 | | | | |
| 7 | | | | |
| 8 | | | | |

Figure56. A comparison with the experimental study of Cekinmez (Ref. [15]) as instantaneous vorticity contours of wing during 7th period for α=30°, α=45° and B=2c, Re=1000. The 1st and 3rd coloums have the 3- D experimental results of current study, which are captured at the mid-span location .
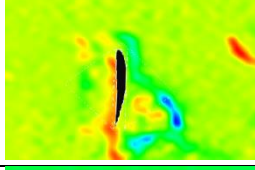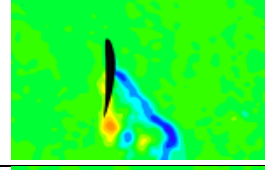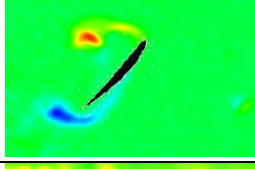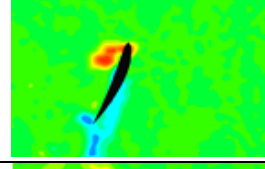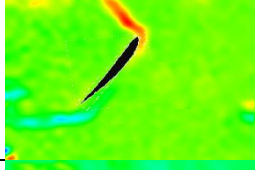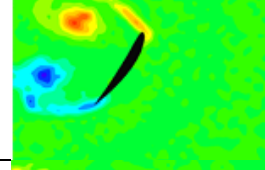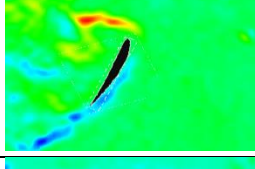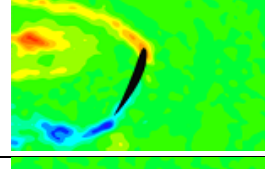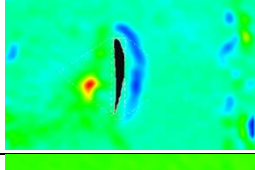
Figure 57. A comparison with the experimental study of Cekinmez (Ref. [15]) as instantaneous vorticity contours of wing during 7th period for α=60° and B=2c, Re=1000. The 1st coloum has the 3- D experimental results of current study, which are captured at the mid-span location.

As for comparison between the experimental results of present study and the numerical results performed by Cekinmez (Ref. [15]), the formation of the LEVs and TEVs is seemed to be similar (see in Figure 58). Main difference between the results is that an interaction between the LEVs and TEVs are significantly more in the numerical results. This difference results from the numerical computations solved by 2-D grid domain. Thus, three dimensionality effect of both LEVs and TEVs on vortex shedding mechanism indicate that the counter-rotating vortices obtained from the experiments are not interact mutually as much as those of the numerical solutions.
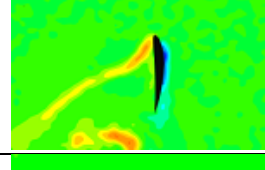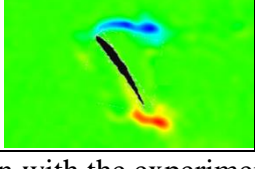
Comparing to the numerical results of the behavior of LEVs, the attachment of LEVs is apparently less due to three-dimensionality effect. Despite of the three-dimensionality effect on the vortex formations of LEVs, the formation of TEVs in experimental results is generally similar to those in numeric simulations. Particularly, at each end of the reversal stroke, the generated LEVs and TEVs in the experimental results are seemed to shed to the flow due to Kramer effect. Also, another difference between the experimental and numerical studies comes from that the fluid motion in spanwise direction is not limited, since the 3-D experiments are performed with single end plate mounted to the wing root in the current study. Hence, the velocity produced along the spanwise direction affects the formation of the LEVs and TEVs in the experimental study.

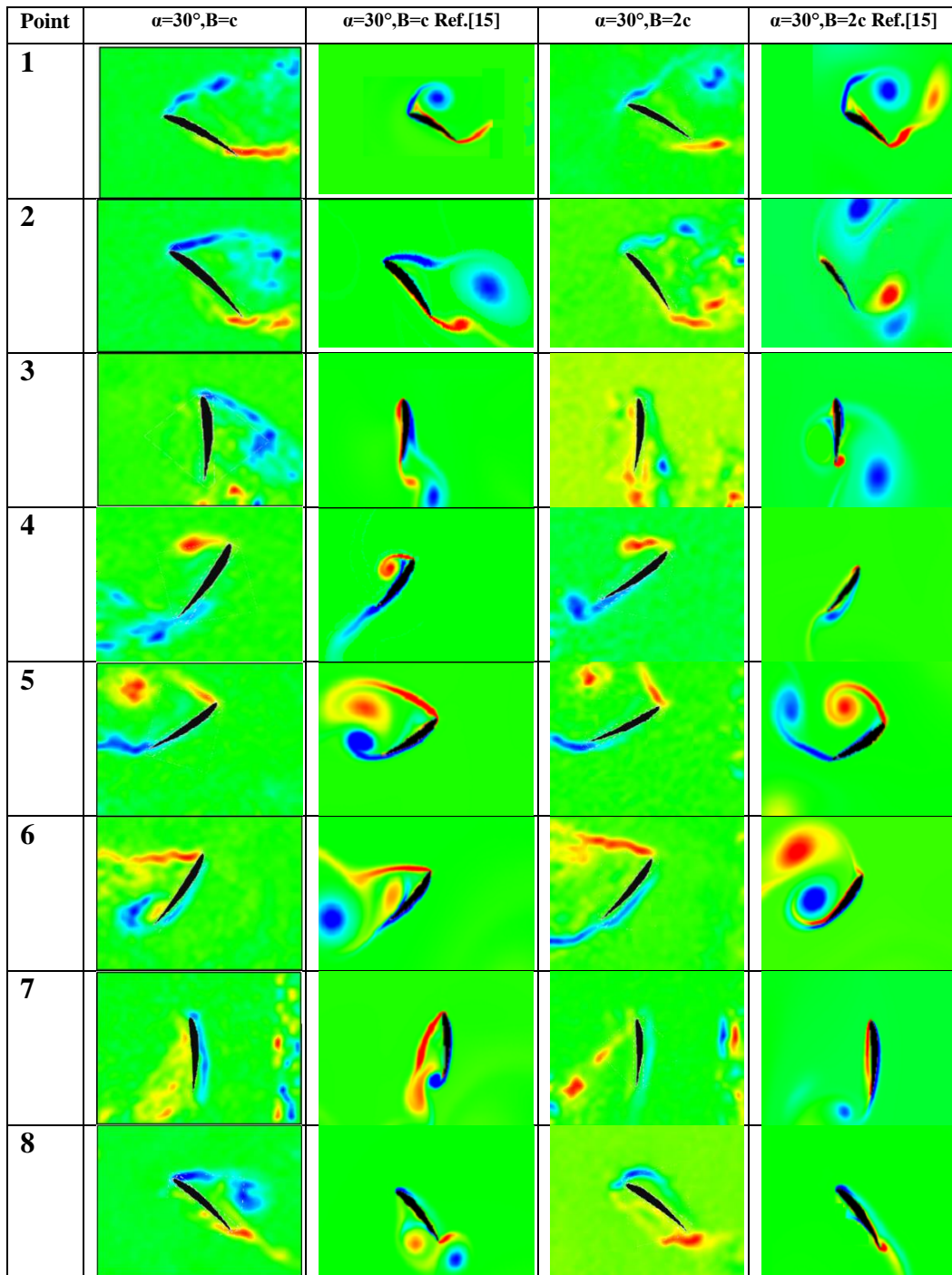| Point | α=30°,B=c | α=30°,B=c Ref.[15] | α=30°,B=2c | α=30°,B=2c Ref.[15] |
|-------|-----------|--------------------|------------|---------------------|
| 1 | | | | |
| 2 | | | | |
| 3 | | | | |
| 4 | | | | |
| 5 | | | | |
| 6 | | | | |
| 7 | | | | |
| 8 | | | | |

Figure 58. A comparison of with the numerical study of Cekinmez (Ref. [15]) as instantaneous vorticity contours of wing during 7th period for α=30°, B=2c and Re=1000. The 1st and 3rd coloums have the 3- D experimental results of current study, which are captured at the mid-span location .

# CHAPTER 5

## CONCLUSION

The main objective of the current study is to describe the vortex formations around wing and to understand the aerodynamic mechanism for the generation of lift and drag forces in the 3-D flow field during figure-of-eight motion. Thus, in this study, investigation of vortex formation around the wing making figure-of-eight motion in hovering flight at low Reynolds numbers are performed by the Stereoscopic Particle Image Velocimetry (SPIV) technique. The experiments are carried out with single wing having cross-section of NACA 6412 airfoil for three different initial angle of attacks ($\alpha=30°$, $\alpha=45°$, $\alpha=60°$) and for two vertical amplitudes (B=c, B=2c) with regarding to investigation of the velocity along the spanwise direction.

Given in the literature survey and the previous studies performed by Cekinmez (Ref. [15]), the physical parameters such as the effect of vertical amplitude and the effect of initial angle of attack are determined to compare the results of present study with the previous studies for the same flapping motion.

Different from previous studies Baskan (Ref. [14]) and Cekinmez (Ref. [15]), the experimental setup was improved in such way that the vortex structures during the figure-of-eight motion could be visualized and measured much better.

The effect of the vertical amplitude during figure-of-eight motion showed that substantially larger LEVs and TEVs are produced at higher vertical amplitudes of motion. It was also observed that the remaining vortices from previous stroke at point 7 are less seen at the higher vertical amplitude of motion.

The literature survey on the vortex mechanisms showed that the delayed stall and Kramer effect plays a significant role on the vortex formations and evolutions. In the current study, the Kramer effect was especially seen at each stroke reversal of

motion. Because of this effect, the higher magnitudes of LEVs and TEVs were detected for the case of B=2c, which are respectively 5.657 (1/s) and 4.359 (1/s). On the other hand, when the magnitude of counter-rotating vortices is investigated throughout the figure-of-eight motion, the magnitude of vortices is higher during the downstroke motion.

The second parameter in current study is the initial angle of attack. Among all initial angle of attacks, the higher magnitudes of LEVs and TEVs are generally observed at the initial angle of attack of 60°. Particularly, the maximum magnitudes of counter-rotating vortices at α=60° are respectively identified as 6.233 (1/s) and 5.356 (1/s) at point 8. For all angle of attacks, it was observed that the magnitude of counter-rotating vortices is higher during the downstroke motion.

The velocity along spanwise direction (W) in the figure-of-eight motion is also investigated. The results indicated that the spanwise motion is in suction side of the wing during down stroke motion. However, in up stroke motion the spanwise velocity components (W) are generally seen in pressure side of the wing (obviously it is the same for LEVs and TEVs). As for investigating the effect of initial angle of attack on the spanwise velocity, a drop in the spanwise velocity is observed by increasing the initial angle of attack. Another investigation is performed for the effects of vertical amplitude on the velocity component in the spanwise direction (W) throughout the motion. Obviously, the results show that for B=2c the motion in the spanwise direction is distributed in a wider area above the upper side of the wing. Therefore, it can be generally concluded that more spanwise motion (W) is observed around leading and trailing edges of the wing model by increasing vertical amplitude of motion

The vortex regions of current study at the mid-span location were compared to experimental results of previous study done by Cekinmez (Ref [15]). It was seen that the formation of the LEVs and the TEVs are similar in both experiments. However, since the present study conducted with single end plate, the three-dimensionality has larger effects on the vortex formations and evolutions. So, the vortex structures around the both edges of wing are more detached from the wing and extended into the flow. Also, the generated LEVs and TEVs in the previous

results are distributed in larger area by comparing to the present results. On the other hand, the magnitudes of counter-rotating vortices in the current study are higher than the previous one.

The experimental results in current study are also compared with the numerical results performed by Cekinmez (Ref. [15]) about to the behavior of LEVs. The experimental results showed that the attachment of LEVs is apparently less due to three-dimensionality effect. Despite of the three-dimensionality effect on the vortex formations of LEVs, the formation of TEVs in 3-D experiments is generally similar to those in numeric simulations. Hence, the velocity along the spanwise direction (W) affects the formation of the LEVs and TEVs in the experimental study.

## 5.1. Future Work:

In this study, the vortex mechanisms around the wing are investigated using Stereo PIV technique. As a future work, the measurement of lift and drag forces on the wing can be carried out by using load cells, which contributes the investigation of unsteady aerodynamic forces produced during figure-of-eight motion.

For a specified location on wing, the experimental results are obtained by the Stereo PIV technique. This leads to problems about interpreting flow visualizations. Taking these problems into consideration, an alternative measurement method such as Volumetric Three-Component Velocimetry (V3V) gets a necessity to visualize 3-D vorticity or velocity distribution in both near and far field.

Up to now, all experimental investigations in our laboratory are performed only for rigid wings by regarding an effect of elastic behavior on the vortex structures. On the other hand, it is no doubt that the elastic behavior is used by birds or insects in actual life either by changing the kinematics of motion or by changing the span length with regard to incoming free stream. Although this field of aerodynamics is evidently difficult to deal with, the vortex structure created by flexible wings can be investigated with the same parameters performed by previous studies and for the same flapping motion in hover.

# REFERENCES

[1] http://www.darpa.mil/tto/mav/mav_auvsi.html , 1997. Last Accessed: 22.07.2014

[2] McMichael, J. M., Francis, M. S., "Micro Air Vehicles - Toward a New Dimension in Flight", DARPA, USA. 1997

[3] Shyy W., Lian Y., Tang J., Viieru D., and Liu H., "Aerodynamics of Low Reynolds Number Flyers", Cambridge University Press, 2008

[4]*http://www.microbot.ru/modules/Static_Docs/data/1_MicroElectroMechanical_Systems_MEMS/Flyers/entomopter_mars_explorer/* Last Accessed : 22.07.2014

[5] http://en.wikipedia.org/wiki/Ornithopter Last Accessed : 22.07.2014.

[6] http://www.gizmag.com/techject-dragonfly-microuav/24900/ Last Accessed : 22.07.2014.

[7] Norberg, U. M., "Hovering flight of the dragonflyAeschna juncea" L.,in T.Y.-T.Wu, C.J.Brokaw, and C. Brennen (Eds.),Swimming and Flying in Nature,Vol. 2 (New York, Plenum), pp. 763–81,1975.

[8] Guerrero J., "Numerical Simulation of the Unsteady Aerodynamics of Flapping Flight", PhD. Thesis, University of Genoa, Department of Civil, Environmental and Architectural Engineering, 2009

[9] http://en.wikipedia.org/wiki/%C3%89tienne-Jules_Marey Last accessed: 22.06.2014

[10] Sane, S. P., "The aerodynamics of insect flight," Journal of Experimental Biology, Vol. 206, pp. 4191-4208, 2003

[11] Kurtulus D. F., "Numerical and Experimental Analysis of Flapping Motion in Hover: Application to Micro Air Vehicle", Joint Ph.D thesis Poitiers University/ENSMA (Poitiers France) and METU (Ankara-Turkey), Poitiers, France, 17 June 2005

[12] Maxworthy, T., "Experiments on the Weis-Fogh mechanism of lift generation by insects in hovering flight", Part 1. Dynamics of the 'fling', J. Fluid Mech., 1979, Vol. 93, Part 1, pp 47-63

[13] Sarıgöl, E., "Experimental And Numerical Analysis Of Flapping Wing Motion", Ph.D. Thesis, METU Aerospace Engineering Department, July 2007.

[14] Başkan Ö., "Experimental And Numerical Investigation Of Flow Field Around Flapping Airfoils Making Figure-Of-Eight In Hover", M.Sc. thesis, METU Aerospace Engineering Department, September 2009.

[15] Çekinmez A. ,"Measurement Of Leading And Trailing Edge Vortex Shedding Mechanism For Flapping Airfoil In Hover Using Particle Image Velocimetry Technique", M.Sc. thesis, METU Aerospace Engineering Department, September 2013.

[16] T. Theodorsen., "General Theory Of Aerodynamic Instability And The Mechanism If Flutter", Technical report, NACA, Technical Report No. 496, 1935.

[17] T. von Karman and J. Burgers., "General Aerodynamic Theory - Perfect Fluids" Aerodynamic Theory, 2, 1935.

[18] Weis-Fogh, Torkel, "Quick Estimates of Flight Fitness in Hovering Animals, Including Novel Mechanisms for Lift Production," Journal of Experimental Biology, vol. 59, pp. 169-230, 1973.

[19] Swanson T.A, "An Experimental And Numerical Investigation Of Flapping And Plunging Wings", PhD Thesis, Missouri University, Department of Aerospace Engineering, 2009

[20] http://www.sciencedirect.com/science/article/pii/S0094114X05001084 Last accessed: 19.06.2014.

[21] Maxworthy, T., "Experiments on the Weis-Fogh Mechanism of Lift Generation by Insects in Hovering Flight. Part 1. Dynamics of the „Fling,"" Journal of Fluid Mechanics, vol. 93, part 1, pp. 47-63, 1979.

[22] Maxworthy, T., "The Fluid Dynamics of Insect Flight.", Ann. Rev. Fluid. Mech., Vol. 13, pp. 329-350, 1981

[23] Ellington, C. P., "The aerodynamics of hovering insect flight: I. The quasi-steady analysis", Philosophical Transactions of the Royal Society of London, Series B 305, 1–15, 1984

[24] Wang Z.J.,"Dissecting Insect Flight" , Annu. Rev. Fluid Mech., Vol. 37, pp.183-210, 2005

[25] Ellington, C. P., Van den Berg, C., Willmott, A. P., and Thomas, A. L. R."Leading-edge vortices in insect flight", Nature (London) 384, 626–30, 1996.

[26] Van Den Berg, C. and Ellington, C.P., "The vortex wake of a hovering model hawkmoth", Phil. Trans. R. Soc. Lond. B 352, pp.317-328, 1997.

[27] Kim J. and Kim C., "Numerical Investigation of the Geometric Factors of an Insect's Wing Motion in an e-Science Environment", Journal of the Korean Physical Society, Vol. 55, No. 5, pp. 2172-2179 , 2009

[28] Liang Z, Dong H., "Computational Analysis of Hovering Hummingbird Flight", 48th AIAA Aerospace Sciences Meeting Including the New Horizons Forum and Aerospace Exposition, 2010

[29] Warrick, D. R., Tobalske, B. W., and Powers, D. R., "Aerodynamics of the hovering hummingbird, Nature (London) 435", 1094–7, 2005.

[30] Wolf M., Ortega-Jimenez V.M. and Dudley R. "Structure Of The Vortex Wake In Hovering Anna's Hummingbirds (Calypte anna)", Proceedings of the Royal Society Biological Sciences, 280: 20132391, 2013

[31] Cheng B., Roll J., Liu Y., Trollin D.R. and Deng X., "Three-Dimensional Vortex Wake Structure Of Flapping Wings In Hovering Flight", The Journal of Royal Society Interface, 11, 20130984, 2013

[32] "FlowManager software and Introduction to PIV Instrumentation, Software"s User Guide", Dantec Dynamics A/S, Pub. No: 9040U3625, September 2002

[33] Seeding materials, http://www.dantecdynamics.com/Default.aspx?ID=731 , Last accessed: 20.06.2014

[34] "IPL Software Installation & User's guide", Dantec Dynamics A/S, Pub. No: 9040U4151, December 2002

[35] Raffel, M., Willert, C., and Kompenhans, J., Particle Image Velocimetry A Practical Guide, Springer Verlag, Berlin, 1998.

[36] "Digital CCD Camera C8484-05C Instruction Manual", Dantec Dynamics A/S, Pub. No: 7450172-01, Ver.1.1, Oct. 2002,

[37] "FlowMap 3D-PIV System, Installation &User Guide", Dantec Dynamics A/S, Pub. No: 9040U4113, Feburary 2002

[38] NACA 6412 Airfoil Profile,

http://www.airfoildb.com/foils/draw/335.svg?axes=true&chord=5 , Last accessed: 22.06.2014

[39] http://en.wikipedia.org/wiki/Vorticity; Last accessed: 22.09.2014

[40] S.A. Ansari, R. Z. bikowski, K. Knowles, "Aerodynamic modelling of insect-like flapping flight for micro air vehicles", Progress in Aerospace Sciences 42 (2006) 129–172, 1 September 2006
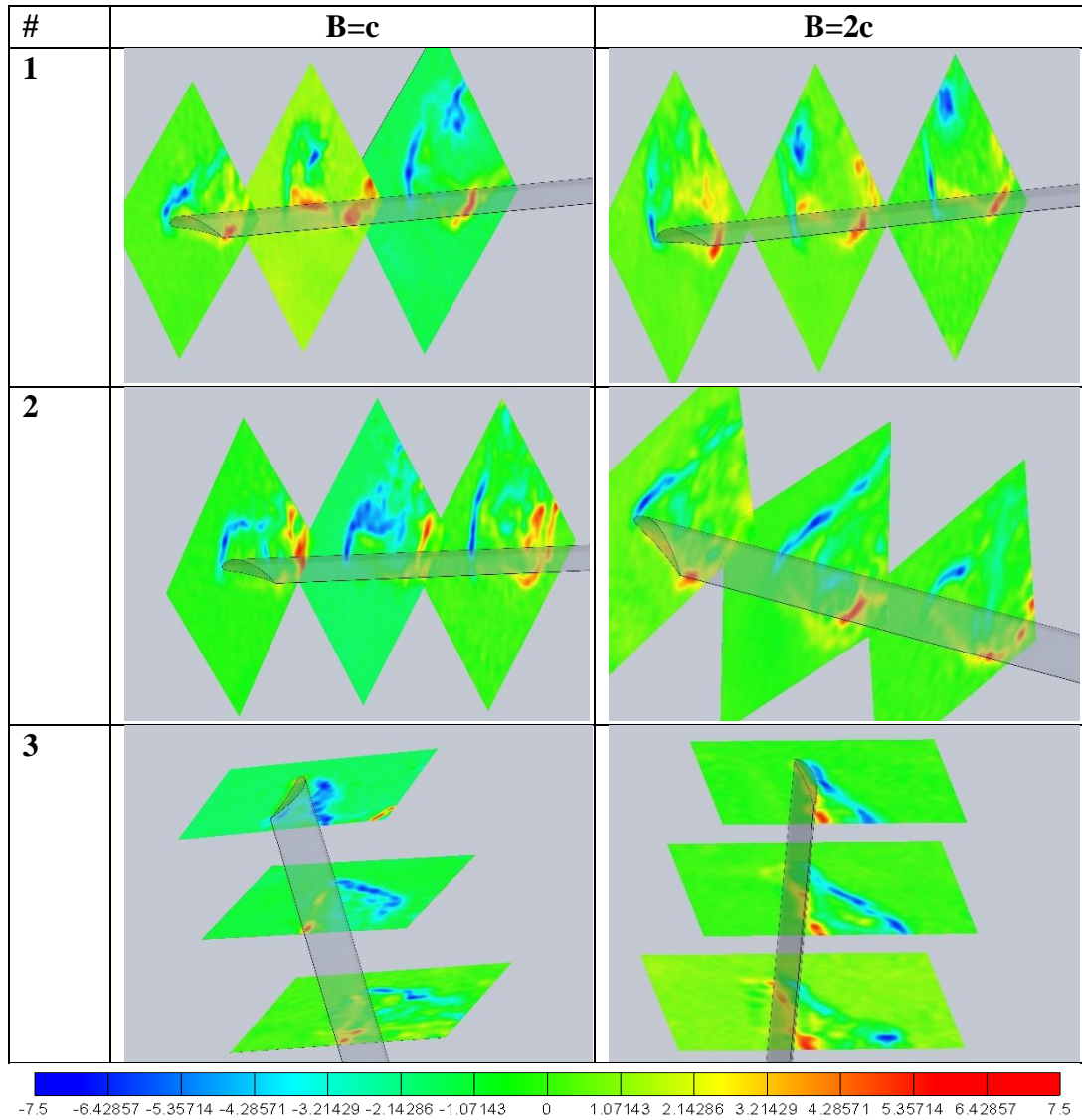
Figure A.1 Instantaneous vorticity contours (1/s) of wing during the 7th period at α=45°, B=c (left), B=2c (right) and Re=1000 for points 1, 2 and 3.
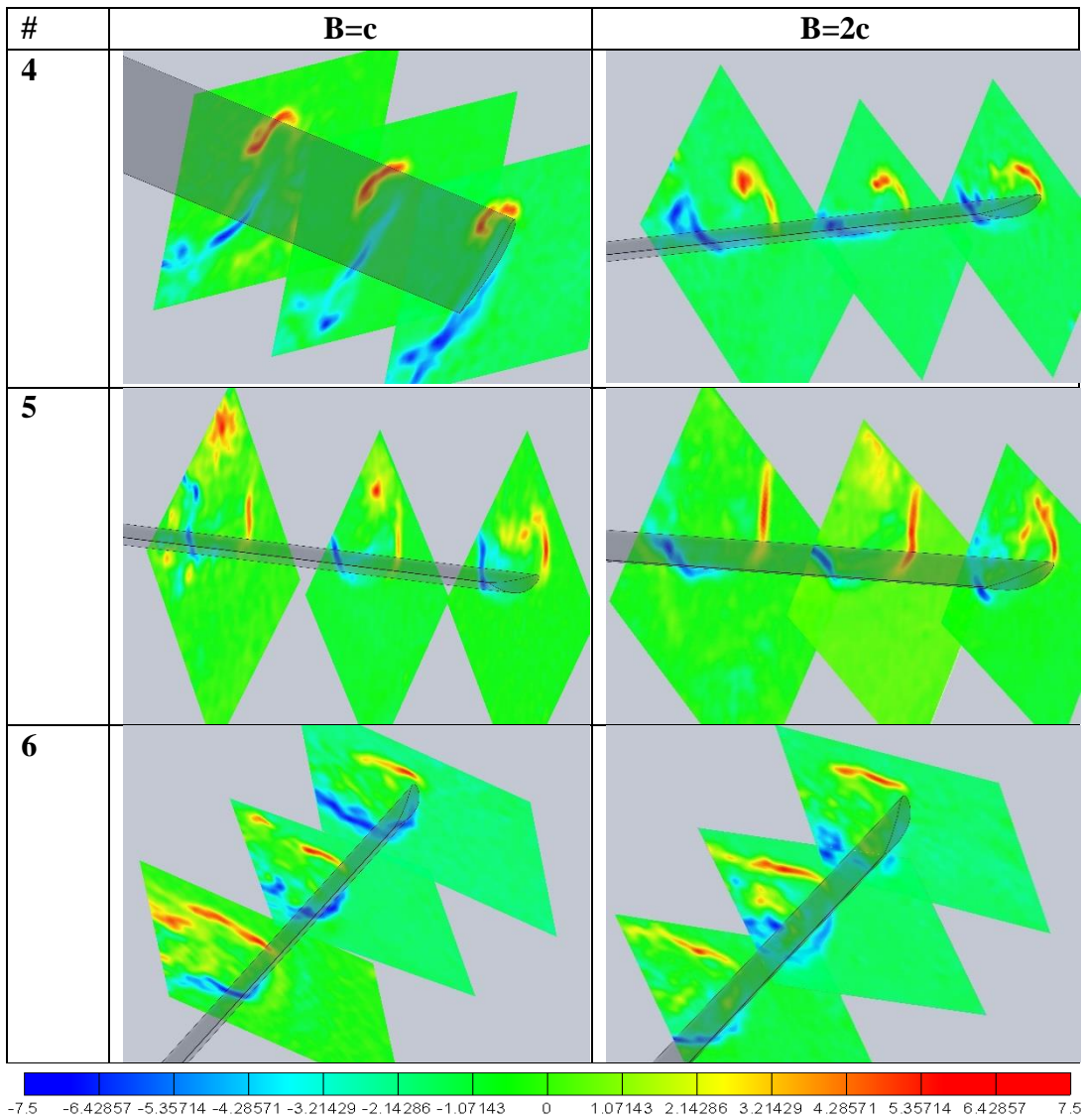
Figure A.2 Instantaneous vorticity contours (1/s) of wing during the 7th period at
α=45°, B=c (left), B=2c (right) and Re=1000 for points 4, 5 and 6.
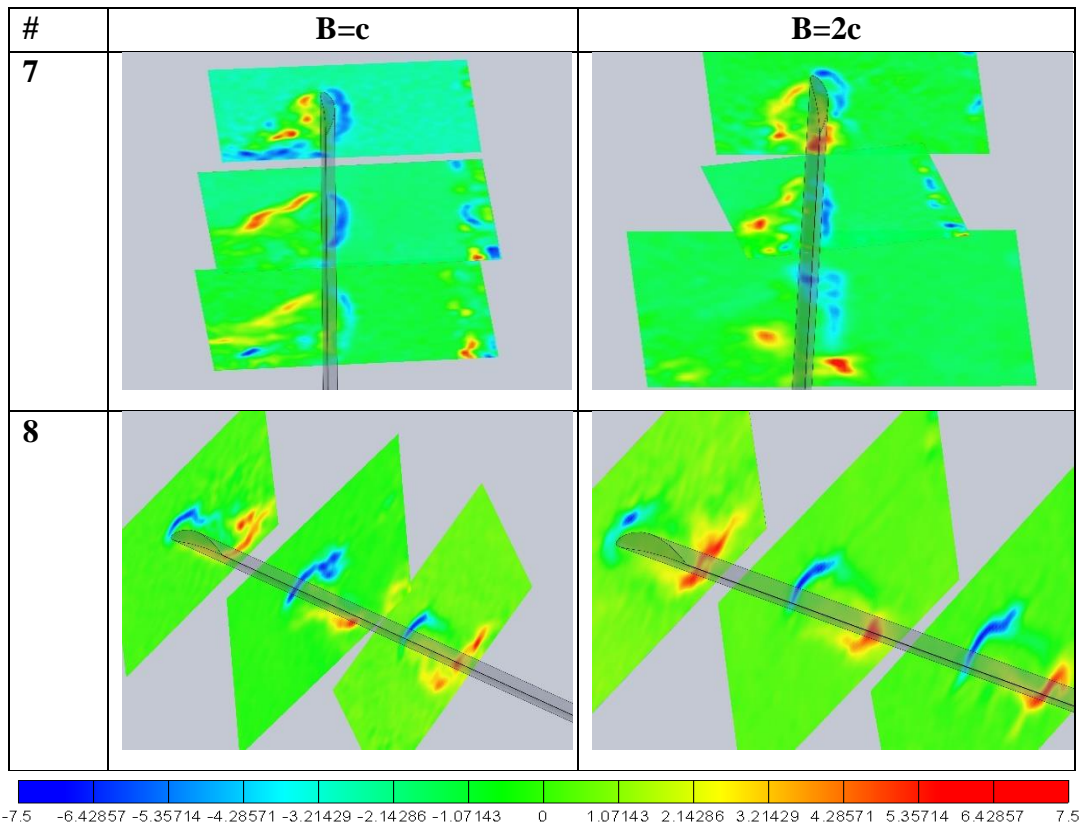
Figure A.3. Instantaneous vorticity contours of NACA 6412 airfoil wing during the 7th period for α=45°, B=c (left), B=2c (right) and Re=1000.
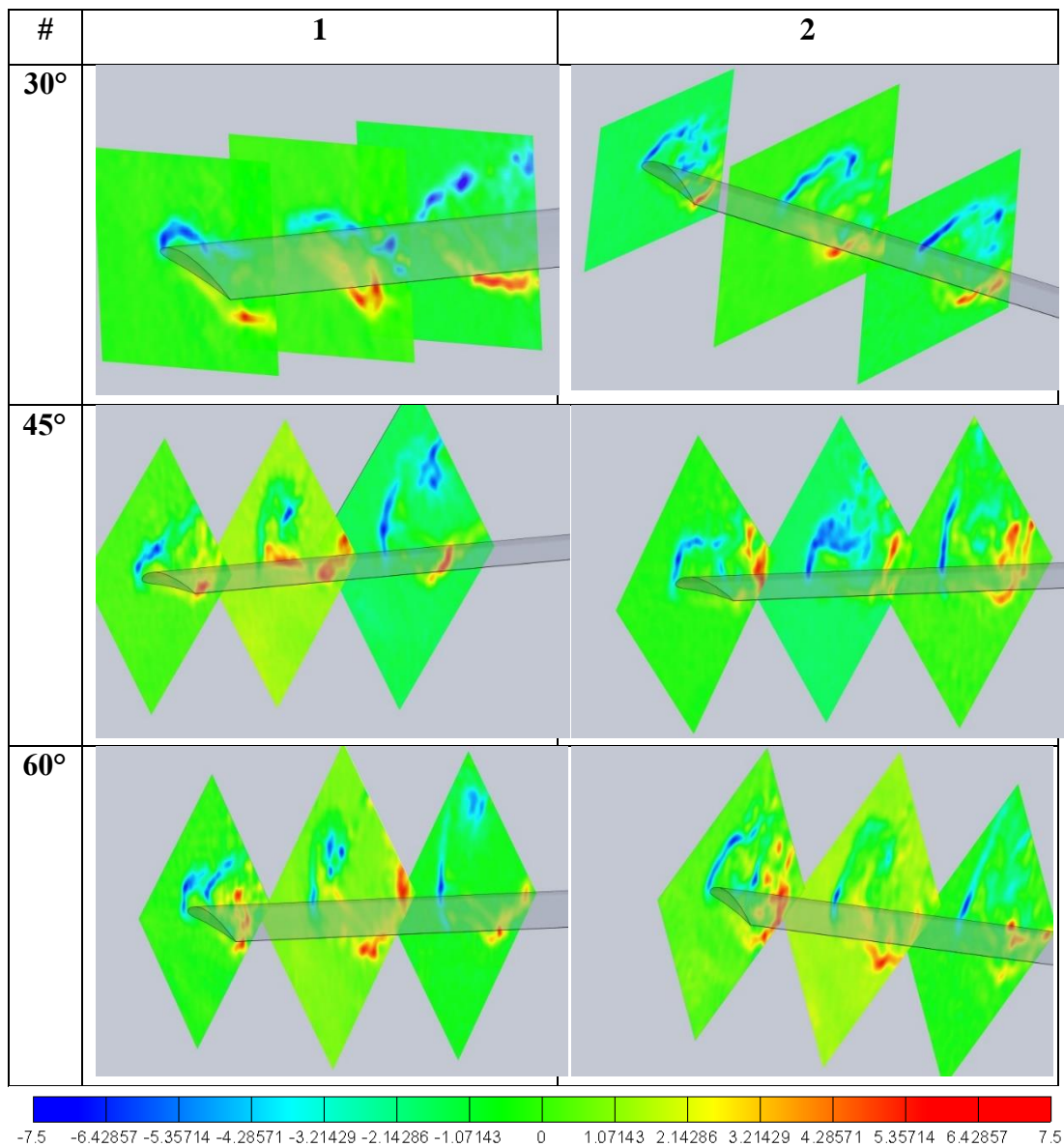
| # | 1 | 2 |
|---|---|---|
| **30°** | | |
| **45°** | | |
| **60°** | | |

Figure A.4. Instantaneous vorticity contours (1/s) of wing at points 1 and 2 during the 7th period for α=30°, α=45°, α=60°, B=c and Re=1000.
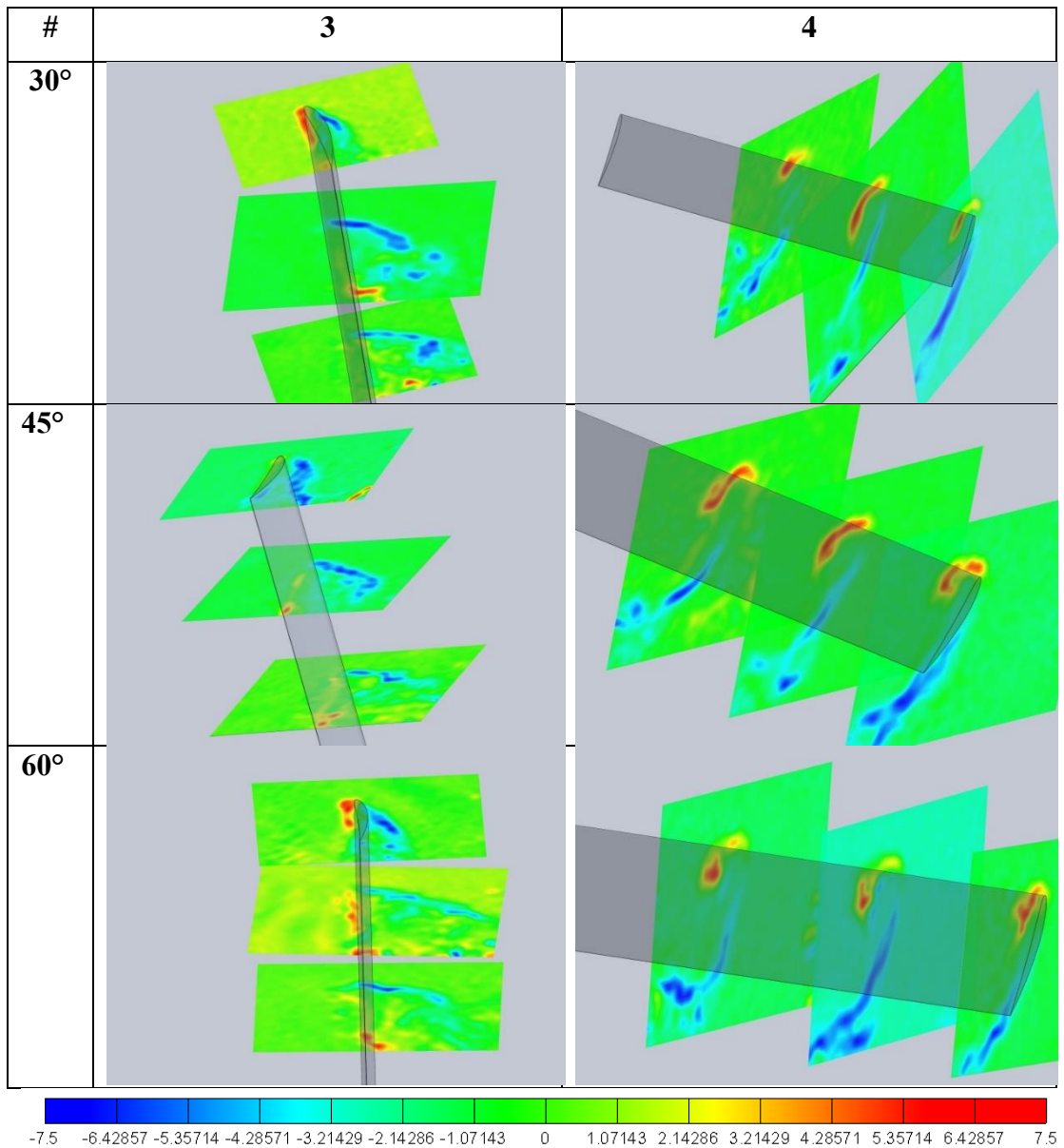
Figure A.5. Instantaneous vorticity contours (1/s) of wing at points 3 and 4 during the 7th period for α=30°, α=45°, α=60°, B=c and Re=1000.
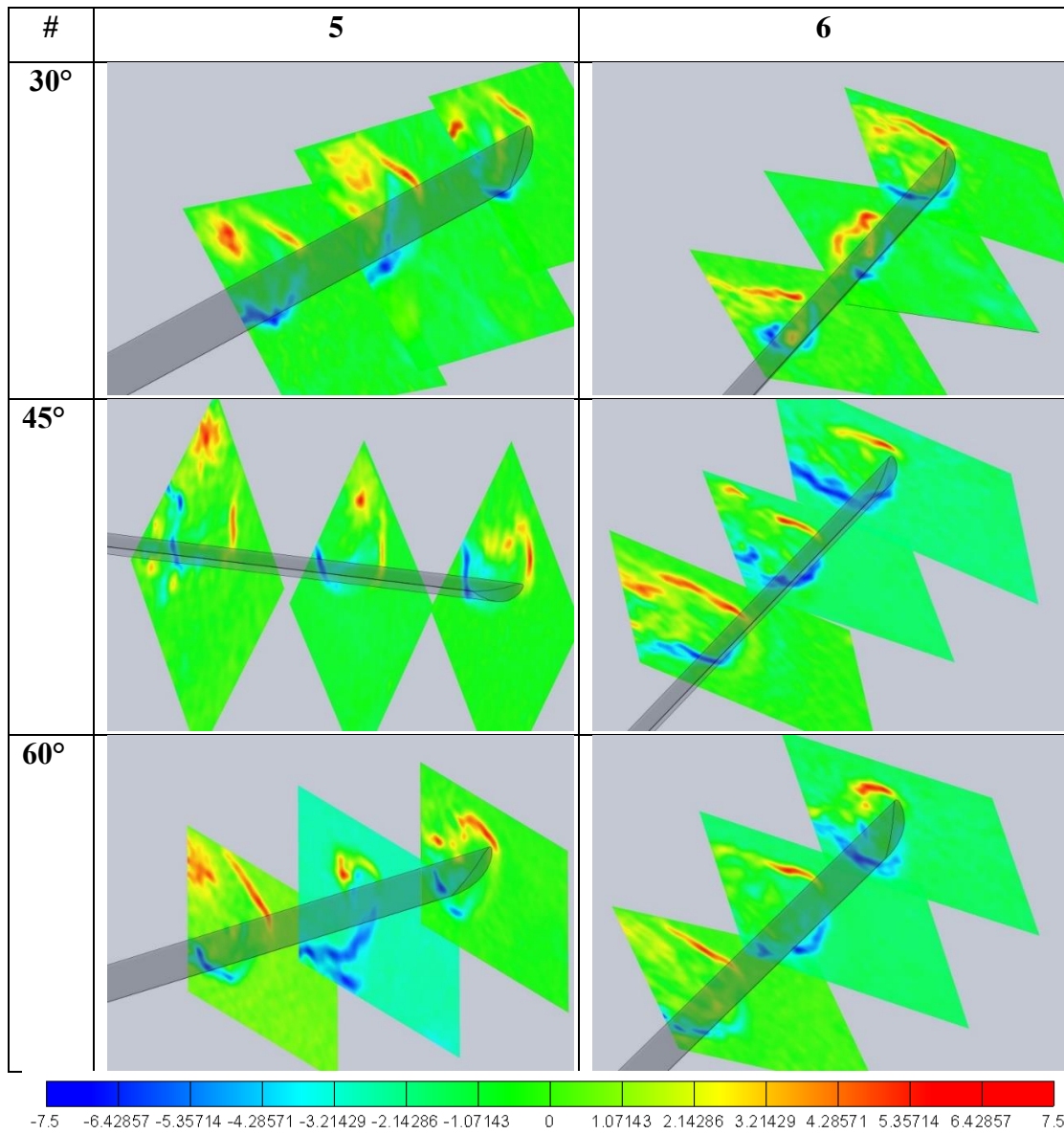
Figure A.6. Instantaneous vorticity contours (1/s) of wing at point 5 and 6 during the 7th period for α=30°, α=45°, α=60°, B=c and Re=1000.
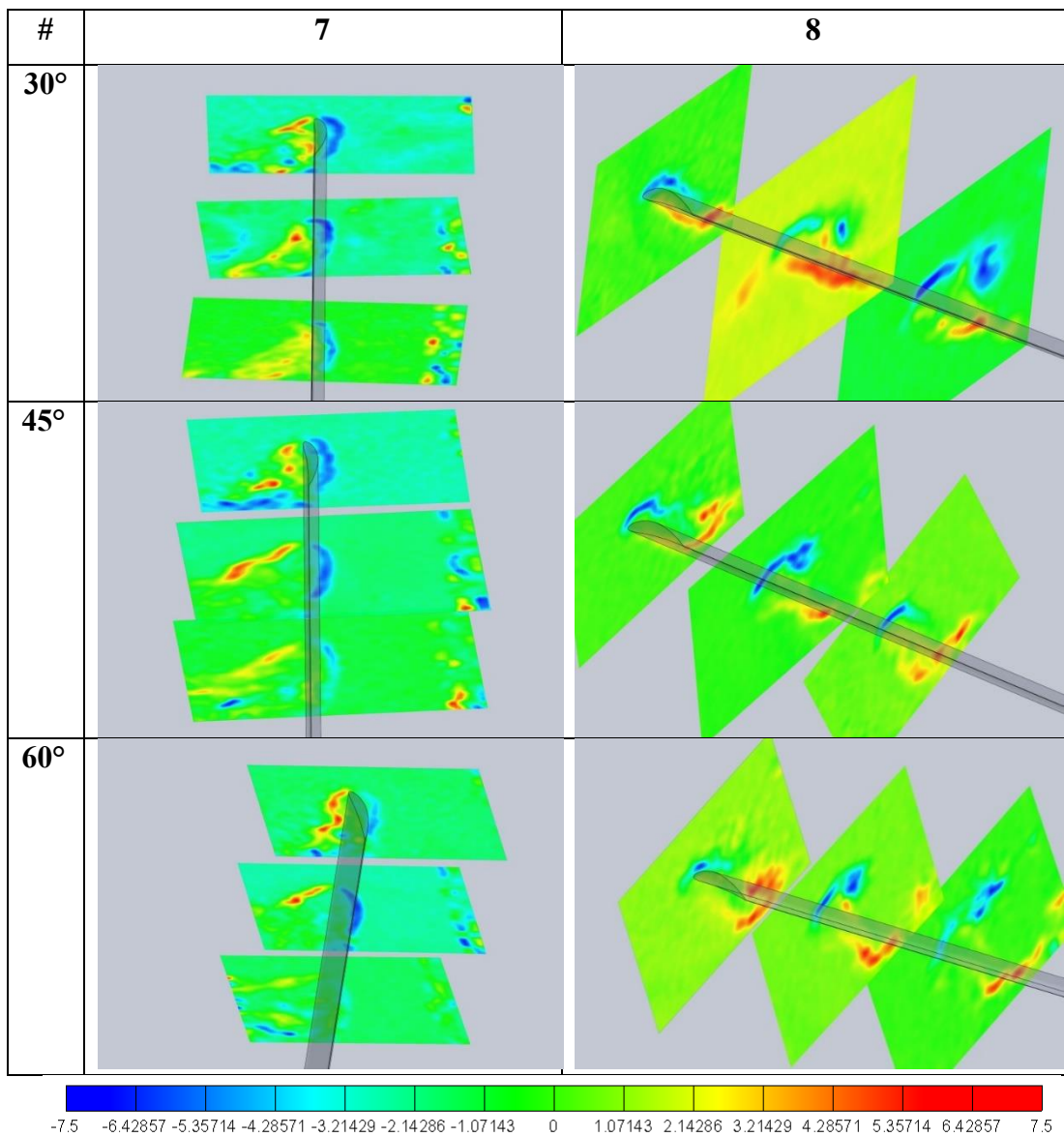
Figure A.7. Instantaneous vorticity contours (1/s) of wing at points 7 and 8 during the 7th period for α=30°, α=45°, α=60°, B=c and Re=1000.